

TECHNISCHE UNIVERSITÄT
CHEMNITZ

Nonequilibrium and semiclassical dynamics in topological phases of quantum matter

Von der Fakultät für Naturwissenschaften der
Technischen Universität Chemnitz

genehmigte

Dissertation

zur Erlangung des akademischen Grades

Doctor rerum naturalium
(Dr. rer. nat.)

vorgelegt

von **M.Sc. Sthitadhi Roy**

geboren am 28.01.1991 in Asansol, India

Tag der Einreichung: 30.10.2017

Gutachter: Prof. Dr. Michael Schreiber
Prof. Dr. Roderich Moessner

Tag der Verteidigung: 28.03.2018

*dedicated to
my mother Sumita Roy,
and
my father Souvik Roy*

Contents

Acknowledgments	9
List of publications	11
List of figures	13
List of tables	16
1 Introduction	19
2 Topological systems and semiclassical dynamics	25
2.1 Model Hamiltonians	26
2.1.1 1D: Su-Schrieffer-Heeger model	26
2.1.2 2D: Haldane’s honeycomb model and related model on square lattice	29
2.1.3 3D: A Weyl semimetal model	31
2.2 Semiclassical equations of motion	34
2.2.1 Berry curvature as a magnetic field in momentum space	35
2.2.2 Anomalous Hall velocity	37
3 Non-equilibrium signatures of topological criticality in local bulk observables	39
3.1 Non-equilibrium protocol	40
3.2 General structure in momentum space	41
3.3 Signatures in one dimension	42
3.3.1 Results for the SSH model	42
3.3.2 Results for Kitaev p-wave superconducting chain	46
3.3.3 Signatures at finite times	47
3.4 Signatures in two dimensions	47
3.5 Absence of signatures for non-topological gap closings	49

3.6	Summary	50
4	Wavepacket dynamics of Chern band lattices in a trap	53
4.1	Simulations of wavepacket dynamics on the Haldane model	55
4.1.1	Model Hamiltonian	55
4.1.2	Construction of wavepackets	56
4.1.3	Harmonic trap	58
4.1.4	Simulations of wavepacket dynamics	59
4.2	Semiclassical dynamics	60
4.3	Comparison of semiclassical predictions with exact dynamics	63
4.4	Semiclassics in a tight trap	67
4.5	Summary	68
5	Spatially local quenches as a probe for Chern insulators	71
5.1	Model Hamiltonian and quench protocols	73
5.2	Half-filled open-boundary system	74
5.2.1	Local density quench from equilibrium	74
5.2.2	Local density pulse	77
5.3	Chiral ‘edge’ dynamics in power-law traps	79
5.4	Summary	83
6	Chern numbers and chiral anomalies in Weyl butterflies	85
6.1	Weyl semimetal in magnetic fields	87
6.2	Chern numbers via wavepacket dynamics	89
6.2.1	Wavepackets localized in momentum	89
6.2.2	Wavepackets with finite momentum spread	91
6.3	Chiral anomalies in the Weyl butterfly	94
6.4	Summary	97
7	Disordered Floquet Chern insulators	99
7.1	Topological invariants for the Floquet system	101
7.2	Model and two-step Floquet drive	106
7.2.1	Static properties	106
7.2.2	Two-step Floquet drive	107
7.3	Phase diagram for translation-invariant system	108
7.3.1	Topological phase transitions	108
7.3.2	Non-topological gap closings	112

7.4	Phase diagram in presence of disorder	114
7.4.1	Topological invariants with disorder	115
7.4.2	Features of the phase diagram	115
7.4.3	Level-spacing statistics	118
7.5	Summary	121
8	Conclusions and Outlook	125

Acknowledgments

In the course of the work constituting this thesis, I have interacted with many individuals in different contexts, be it scientific or administrative, without whose help the work would not have been possible. It is my honour to express my sincere gratitude to all of them.

First of all I would like to thank Prof. Dr. Roderich Moessner for giving me the opportunity to pursue my doctoral research at an amazing place like MPIPKS, and constantly providing wonderful guidance at many different levels, be it the finer nuances of my projects, or the bigger picture of visualising the projects in their entirety, or at the even broader level of the general outlook of the scientific community towards a subject. My discussions with him were not only lessons in physics but also more generally lessons in how to think about research problems from a broader perspective and then break them down into smaller pieces which could then be solved. I hope whatever of this approach I have managed to imbibe will hold me in good stead in my future scientific career.

I extend my sincere gratitude to Prof. Dr. Michael Schreiber kindly agreeing to referee the thesis and allowing me to submit it at the University of Chemnitz.

I would especially like to thank Dr. Adolfo G. Grushin for being a such a great senior collaborator, it has been extremely enjoyable working with and learning from him, and I look forward to the ongoing and future collaborations with him. A lot of the what I understand about topological condensed matter systems have been courtesy Adolfo, and I also thank him for introducing me to the subject of Weyl semimetals.

I would like to thank everyone with whom I have collaborated over the past four years, Prof. Dr. Soumya Bera, Dr. Leda Bucciattini, Prof. Dr. Arnab Das, Prof. Dr. Sourin Das, Prof. Dr. Amit Dutta, Prof. Dr. Masud Haque, Dr. Markus Heyl, Dr. Ivan M. Khaymovich, Dr. Sota Kitamura, Dr. Michael Kolodrubetz, Dr. Achilleas Lazarides, Prof. Dr. Joel E. Moore, Dr. Tanay Nag, Dr. Takashi Oka, Dr. Krishanu Roychowdhury, Dr. Kush Saha, Prof. Dr. Diptiman Sen, Dr. Abhiram Soori, Prof.

Dr. G.J. Sreejith, and Guiseppe De Tomasi; working with them has been a privilege and pleasure for me.

I would like to thank the visitors programme of MPIPKS, the administrative staff of MPIPKS, and Frau Regine Schuppe, for helping me out with various administrative and logistical affairs and ensuring an as smooth as possible stay in Dresden. I am also immensely thankful to the IT department at MPIPKS for maintaining such a state of the art computational cluster here, the use of which was integral to my doctoral work.

I would like to express my heartfelt thanks to my parents, Sumita Roy and Souvik Roy for being a constant source of encouragement and support throughout my life. In addition, I would like to thank my dear friend Prakriti Palchoudhury for her companionship and for being the source of a positive distraction which was much needed on this journey.

List of publications (2014-)

Publications marked with † constitute various chapters of the thesis.

1. **Sthitadhi Roy**, Michael Kolodrubetz, Nathan Goldman, Adolfo G. Grushin, *Tunable axial gauge fields in engineered Weyl semimetals: Semiclassical analysis and optical lattice implementations*, arXiv:1708.08469
2. **Sthitadhi Roy**, Ivan M. Khaymovich, Arnab Das, Roderich Moessner, *Multifractality without fine-tuning in a Floquet quasiperiodic chain*, arXiv:1706.05012
3. Leda Bucciantini, **Sthitadhi Roy**, Sota Kitamura, Takashi Oka, *Emergent Weyl nodes and Fermi arcs in a Floquet Weyl semimetal*, **Phys. Rev. B** **96**, 041126(R) (2017) (**Rapid Communication**)
4. † **Sthitadhi Roy**, Roderich Moessner, Arnab Das, *Locating topological phase transitions using non-equilibrium signatures in local bulk observables*, **Phys. Rev. B** **95**, 041105(R) (2017) (**Rapid Communication**)
5. † **Sthitadhi Roy**, G. J. Sreejith, *Disordered Chern insulator with a two step Floquet drive*, **Phys. Rev. B** **94**, 214293 (2016)
6. † **Sthitadhi Roy**, Michael Kolodrubetz, Joel E. Moore, Adolfo G. Grushin, *Chern numbers and chiral anomalies in Weyl butterflies*, **Phys. Rev. B** **94**, 161107(R) (2016) (**Rapid Communication**)
7. Giuseppe De Tomasi, **Sthitadhi Roy**, Soumya Bera, *Generalized Dyson model: nature of zero mode and its implication in dynamics*, **Phys. Rev. B** **94**, 144202 (2016)
8. † Adolfo G. Grushin, **Sthitadhi Roy**, Masudul Haque, *Response of fermions in Chern bands to spatially local quenches*, **J. Stat. Mech.** **083103** (2016)
9. **Sthitadhi Roy**, Krishanu Roychowdhury, Sourin Das, *Pseudo-spin half metals on the surface of 3-D topological insulators*, **New J. Phys.** **18**, 073038 (2016)

10. **Sthitadhi Roy**, Sourin Das, *Transport signatures of surface potentials on three-dimensional topological insulators*, **Phys. Rev. B** **93**, 085422 (2016)
11. [†] **Sthitadhi Roy**, Adolfo G. Grushin, Roderich Moessner, Masudul Haque, *Wavepacket dynamics on Chern band lattices in a trap*, **Phys. Rev. A** **92**, 063626 (2015)
12. **Sthitadhi Roy**, Kush Saha, Sourin Das, *Probing surface states exposed by crystal terminations at arbitrary orientations of three-dimensional topological insulators*, **Phys. Rev. B** **91**, 195415 (2015)
13. **Sthitadhi Roy**, Abhiram Soori, Sourin Das, *Tunnel Magnetoresistance scan of a pristine 3D topological insulator*, **Phys. Rev. B** **91**, 041109(R) (2015) (**Rapid Communication**)
14. Tanay Nag, **Sthitadhi Roy**, Amit Dutta, Diptiman Sen, *Dynamical localization in a chain of hard core bosons under a periodic driving*, **Phys. Rev. B** **89**, 165425 (2014)

List of Figures

2.1	Schematic lattice of the SSH chain, the energy spectrum of the SSH chain, and demonstration of the topological nature of the energy bands.	28
2.2	Schematic representation of Haldane's honeycomb model and its phase diagram.	30
2.3	Schematic of a Chern insulator model realised on a square lattice, the energy spectrum of the model, and its phase diagram.	32
2.4	Energy spectrum of the Weyl semimetal model	33
3.1	Locating the topological phase transitions using non-equilibrium signatures in the SSH model.	44
3.2	The overlap $\chi_k(\lambda_i, \lambda_f)$ plotted as function of k for different values of λ_f for a fixed λ_i shows the mechanism of the non-analyticity.	44
3.3	Non-analytic behavior of local observables in non-equilibrium states as signatures of topological phase transitions in the Kitaev p-wave superconducting chain.	46
3.4	Results for the SSH chain at finite t .	47
3.5	Locating the topological phase boundary using a non-equilibrium signature in the bulk (Haldane model).	48
3.6	Absence of non-analytic signatures for non-topological gap closings	49
4.1	Honeycomb lattice defining the Haldane model along with its energy spectrum and Berry curvature distribution in the lower band.	55
4.2	The overlaps \mathcal{O}_α of the initial wavepacket at different initial momenta \mathbf{k}_0 with the eigenstates of \mathcal{H}_{HM} .	58
4.3	Geometry of the lattice and the trap, along with the trajectory of the wavepacket.	59
4.4	Trajectories of the wavepacket in momentum space.	60
4.5	Profiles of $\dot{\theta}_-(\mathbf{k})$ and $\dot{\theta}_+(\mathbf{k})$ in the Brillouin zone.	63
4.6	Comparison of the angular velocities $\langle \dot{\theta} \rangle_{\text{exact}}$, $\langle \dot{\theta} \rangle_{\text{pp-sc}}$, and $\langle \dot{\theta} \rangle_{\text{wp-sc}}$.	64

4.7	Overlaps as in Fig. 4.2(a), for a smaller wavepacket.	66
4.8	Dynamics in a tight trap.	67
5.1	Schematically show the two quench protocols.	72
5.2	Single particle-energy spectrum and edge states	73
5.3	The time evolution of the density in the Chern insulator, following a quench from equilibrium.	75
5.4	Density difference $\varrho_{nn}(t) - \varrho_{nn,0}$ at the site n marked in Fig. 5.3. . . .	75
5.5	The local density difference $\varrho_{ii}(t) - \varrho_{ii,0}$ is plotted for different times to show the dynamics of the edge excitation in the case of the pulse quench.	78
5.6	The density difference is plotted against time for the case of the pulse quench.	78
5.7	Single-particle energy spectrum and eigenstates in the presence of a trap. 80	
5.8	The density along the x direction for a fixed cut in real space in the presence of a trap.	81
5.9	Four snapshots of the density perturbation $\varrho_{ii}(t) - \varrho_{ii,0}$ after a quench in the presence of a trap.	82
6.1	Hofstadter butterfly spectra for a Weyl semimetal at rational fluxes showing multiplicity of Weyl nodes	87
6.2	Hall drift of the center of mass of a wavepacket for different values of the magnitude of the electric field E at two representative k_z values. .	90
6.3	\mathcal{C}_{eff} as a function of σ for the two cases corresponding to Figure 6.2. The dashed lines correspond to the \mathcal{C}_{sat} values calculated from Eq. (6.9). 93	
6.4	Chiral anomaly of the Weyl butterfly	95
6.5	Time of flight occupancy profiles in the (k_y, k_z) plane showing the chiral anomaly.	96
7.1	The levitation and annihilation mechanism for Floquet systems is shown schematically.	101
7.2	Evolution of eigenvalues of the modified unitary operator for a choice of a particular branch cut.	103
7.3	Winding of the edge states of the Floquet system depending on the choice of the branch cut.	103
7.4	The Floquet quasienergy spectrum $\omega_{\pm, \mathbf{k}}$ at different critical points. . .	109

7.5	Graphical representation of the phase diagram of the periodically driven Chern insulator.	111
7.6	Gap closings in the Floquet quasienergy spectra away from the high-symmetry points.	113
7.7	Phase diagram in terms of ν_0 and ν_π are shown in the presence of disorder.	116
7.8	Robustness of edge modes (winding invariants) to disorder.	117
7.9	Level-spacing statistics for different disorder strengths	119
7.10	Level-spacing statistics showing the reentrant topological behavior.	121

List of Tables

2.1	Periodic table of topological insulators and superconductors	26
7.1	Summary of the phase transitions of the periodically driven Chern insulator. The four columns show the critical points, the changes in \mathcal{C} , ν_0 , and ν_π	111

Chapter 1

Introduction

Classifying different of phases matter has always been one of the most fundamental and important questions of science, which also led to the birth of the immensely rich field of phase transitions and critical phenomena, and the field has been evolving ever since. A naturally accompanying field of research has been the development of methods and techniques, both theoretical and experimental, to characterize different phases and critical points. Much of the early development in classifying phases of matter was built around Landau's theory of broken symmetries, one of the cornerstones of condensed matter physics. In the more recent past, however, it has become increasingly evident that physical systems can exhibit much richer phase structures than indicated by Landau's theory. These new phases of matter, dubbed as possessing *topological order*, are characterized by exotic properties like long-ranged quantum entanglement and perfectly conducting edge states. In the presence of symmetries, even short-ranged entangled states are known to have symmetry-protected topological order.

Strongly interlaced with the research in topological condensed matter physics has been the development of the field of non-equilibrium quantum dynamics. While on one hand, non-equilibrium responses of topological systems have proved to be one of the most useful ways of extracting their topological properties, on the other hand, exotic topological phases have also been discovered which have no analog in equilibrium systems. A lot of the progress has been fuelled by the extraordinary advances in experiments with cold atoms in optical lattices. They have enabled not only the synthesis of topological phases of matter but also served as ideal platforms to study their non-equilibrium responses.

This thesis studies various aspects of the field of non-equilibrium dynamics of topological systems under the umbrella of two broad questions, first, how non-equilibrium dynamics can be used to characterize topological phases or locate topological critical

points, and second, what new topological phases can be realized out of equilibrium. Topological order is often characterized via expectation values of non-local operators which are traditionally difficult to measure or observe experimentally. Hence, characterization of topological phases via local observables, dynamical or otherwise, which are accessible in experiments, is not only of fundamental theoretical importance but could present promising opportunities to further advance their experimental studies.

Topology had already announced its presence in condensed matter physics more than thirty years ago in the form of a quantized Hall conductance of a two-dimensional electron gas subjected to strong magnetic fields. In their ground breaking experiment discovering the integer quantum Hall effect, [von Klitzing *et al.* \(1980\)](#) found that the Hall conductance showed robust plateaus at integer multiples of e^2/h where e and h are electronic charge and Planck's constant respectively, two of the fundamental constants of nature. At the heart of this robust quantization of the Hall conductance lay the topological interpretation of the integer quantum Hall effect, as was shown in their seminal paper by [Thouless *et al.* \(1982\)](#) only a couple of years later. They showed that the quantized Hall conductivity is equal to a topological invariant, namely the Chern number, which is a bulk property. This came to be known as the *bulk-boundary correspondence* and was put in a more formal setting for the quantum Hall effect by [Hatsugai \(1993a,b\)](#). The statement for a generic system is that the number of chiral modes propagating along the edges of a two-dimensional system with their energies in the gaps between the bands of the energy spectrum the bulk is equal to the sum of the Chern numbers of all the bulk bands below the energy.

The topological origins of the quantized Hall conductivity were put by Haldane into a much broader and general context embedding the integer quantum Hall effect in a class of topological systems, which have now come to be known by the name of *Chern insulators*. In his seminal work, [Haldane \(1988\)](#) showed that one could obtain a finite quantized Hall conductivity in a system of spinless fermions with linear dispersion just by breaking time-reversal symmetry, which he achieved by the means of complex hopping amplitudes between lattice sites encoding a synthetic gauge field. The resulting system has a gapped bulk spectrum with non-zero Chern numbers in the bands, which equal the number of perfectly conducting chiral edge modes on the edge, consistent with the bulk-boundary correspondence.

The discovery of time-reversal invariant topological insulators in two- [[Kane and Mele \(2005b,a\)](#); [Bernevig and Zhang \(2006\)](#); [Bernevig *et al.* \(2006\)](#)] and three- [[Fu *et al.* \(2007\)](#); [Roy \(2009\)](#); [Zhang *et al.* \(2009\)](#); [Hasan and Moore \(2011\)](#)] dimensions spurred a tremendous amount of research on topological insulators, both theoretical

and experimental. As these are symmetry-protected topological phases, efforts were made to classify all possible such topological phases with regard to their topological invariants given the dimensionality and symmetries. This finally culminated into the *periodic table for topological insulators and superconductors* [Kitaev *et al.* (2009); Ryu *et al.* (2010)]. The classification is done using homotopy groups, C lifford algebras, K -theory, and nonlinear sigma models describing Anderson (de)localization at the surface of a material; for a review see Chiu *et al.* (2016).

The research in gapped topological phases was well complemented by the discovery of a new class of three-dimensional topological systems with a gapless bulk, namely Weyl semimetals. The characteristic feature of such systems that the low energy theory of the system is described by the Weyl equations. The gapless momenta in the Brillouin zone, known as the Weyl points, turn out to be sources or sinks of Chern flux depending on their chirality. Weyl semimetals have emerged as an exciting area of research due to their exotic features like open Fermi arcs on the surface and chiral Landau levels in the presence of a magnetic field, which further lead to exotic electromagnetic responses like the chiral magnetic effect (generation of an electric current parallel to an external magnetic field due to an imbalance in the number of left- and right-chiral Weyl fermions), negative magnetoresistance (suppression of electrical resistivity upon increasing an applied external magnetic field), and condensed matter realizations of various quantum anomalies.

A short overview of the models of topological systems in one, two, and three dimensions considered in this thesis can be found in Chapter 2

Although solid state materials which are topological insulators and Weyl semimetals have been discovered, and have led to a significant advancement in their understanding via mesoscopic transport and standard electronic structure probe experiments like ARPES, they are not conducive towards studying non-equilibrium phenomena due to the rather short time scales within which such systems relax to a steady state once thrown out of equilibrium. On the other hand, the realization of these models with ultracold atoms in optical lattices provides ideal platforms to study their non-equilibrium behavior due to much larger time scales of coherent quantum evolution (which are often five to six orders of magnitude larger than their solid state counterparts). Moreover, they also allow for immense tunability across parameter regimes and often realize simple models which have yet not been realized in solid state materials. A case in point is Haldane's honeycomb model [Haldane (1988)] whose topological band structure was recently realized with ultracold fermions in a

periodically modulated honeycomb lattice [Jotzu *et al.* (2014)]. The experiment involves a circular modulation of the lattice position, such that the effective Floquet Hamiltonian contains complex next-nearest neighbour hoppings effectively breaking time-reversal symmetry. Another effective way of generating synthetic gauge fields in optical lattices has been via laser-assisted tunneling in a tilted optical lattice, originally proposed by Jaksch and Zoller (2003). The essential idea consists of tilting the optical lattice along a certain direction and using a pair of Raman lasers to induce hoppings using the internal states of the atoms which pick up a phase due to the difference in the wavevectors of the two lasers. This method has been successfully used to generate the Harper-Hofstadter model [Aidelsburger *et al.* (2013); Miyake *et al.* (2013)], which one can argue is also one of the simplest Chern insulator models. In fact, there has also been a proposal following the very same technique to realize a Weyl semimetal in a three-dimensional optical lattice [Dubček *et al.* (2015)].

In both the essential ideas discussed above, it is interesting to note that the central problem actually boils down to working with a system described by a Hamiltonian which is periodic in time. This falls into a broad class of systems, often dubbed Floquet systems, which has been one of the most intense fields of research in the past few years. Floquet systems being inherently out of equilibrium have called for re-interpreting their statistical mechanics and thermodynamics [Lazarides *et al.* (2014a,b)], and have shown exotic phases hitherto not known in equilibrium, for instance, discrete time crystals [Khemani *et al.* (2016); Else *et al.* (2016); Yao *et al.* (2017)] and anomalous topological edge states [Rudner *et al.* (2013)]. However, the genesis of Floquet topological phases was the work of Oka and Aoki (2009) where it was shown that a graphene sheet subjected to circularly polarized light hosts chiral edge modes and a quantized Hall conductivity. Tremendous progress in the field from then on has culminated into a classification of Floquet topological phases [Kitagawa *et al.* (2010); von Keyserlingk and Sondhi (2016a,b); Potter *et al.* (2016); Roy and Harper (2016)].

Parallel to the advancement in the field of Floquet topological phases, the effect of disorder on topological systems has also received much attention. Given that disorder plays such a crucial role in localising the bulk cyclotron orbits in an integer quantum Hall system, it is all but natural and inevitable that it should throw up new interesting physics in the context of topological insulators, especially when the picture of a topological band structure in the Brillouin zone breaks down in the presence of disorder. One of the most interesting aspects of the interplay of disorder-induced Anderson localization and topological order is the presence of disorder-induced topological phase

transitions and a disorder-induced topological phase which has been dubbed as the *topological Anderson insulator* [Li *et al.* (2009); Groth *et al.* (2009)]. The interplay of disorder and time-periodic modulation allows for further exotic topological phases, for instance, the anomalous Floquet-Anderson insulator as a non-adiabatic quantized charge pump [Titum *et al.* (2016)].

Motivated by these exciting developments of non-equilibrium dynamics of topological systems, this thesis attempts to explore some specific questions pertinent to the field.

In Chapter 3 it is shown that within a non-equilibrium setup obtained via a quantum quench, local bulk observables can show sharp signatures of topological quantum criticality via a non-analyticity in parameter space at the critical point. As described in a foundational work on the topic by Wegner (1971), via non-local unitary transformations one can go to a basis where a topological quantum phase transition can be described in the language of a conventional phase transitions using a local order parameter. However, the interesting aspect of the approach described in Chapter 3 is that within the non-equilibrium setup, the local bulk observables can locate the critical point in the natural basis where the phase transition is topological and not described by a local order parameter.

The next aspect that the thesis explores is how non-equilibrium dynamics, more precisely wavepacket dynamics, can be used to probe topological phases with an emphasis on cold atom experiments. The theoretical tool used extensively in this regard are the semiclassical equations of motion. The Chern number of a band is the net flux of Berry curvature through the entire two-dimensional Brillouin zone. The Berry curvature, hence, can be interpreted as a magnetic field but in reciprocal space and it appropriately adds a correction term to the real-space group velocity. Hence, the motion of the wavepacket can be used to map out the Berry curvature and thence the topology of the band. Some details of the semiclassical equations can be found in Chapter 2. Such an approach is applied to Haldane's honeycomb model in Chapter 4. Complementary to these bulk responses, spatially local quenches in Chern insulators can be used to probe the presence or absence of chiral edge modes as explored in Chapter 5. Local density perturbations at the edges between topological and trivial regions show a dynamical chiral response along the edge.

The idea of semiclassical equations of motion can be extended to the case of a three-dimensional Weyl semimetal. Since in cold atom experiments, magnetic fields are realized synthetically via phases in complex hoppings, exploring the Hofstadter limit is a natural scenario. When the magnetic field penetrating a two-dimensional

system becomes so large that the associated magnetic length, $l_B = \sqrt{\hbar c/eB}$ (B being the magnetic field), becomes comparable to the lattice spacing, the energy spectrum of the system is described by fractal known as the *Hofstadter butterfly* [Hofstadter (1976)], first studied by Hofstadter and hence the name. Chapter 6 introduces the Weyl butterfly, a set of fractals which describes the spectrum of a Weyl semimetal subjected to a magnetic field, and we characterize the fractal set of Weyl nodes in the spectrum using wavepacket dynamics to reveal their chirality and location. Moreover, we show that the chiral anomaly – a hallmark of the topological Weyl semimetal – does not remain proportional to the magnetic field at large fields, but rather inherits a fractal structure of linear regimes as a function of external field.

In Chapter 7, the phase diagram of the disordered Chern insulator with a Floquet drive is explored. In the model considered there are indeed topological Floquet edge modes which are exclusive to Floquet systems, for instance, the edge modes in gaps of the quasienergy spectrum around $\pm\pi$. There are also disorder-induced topological transitions between different Floquet topological phases, due to a mechanism shown to be of *levitation-annihilation* type.

The thesis is structured as follows. Chapter 2 discusses some typical models hosting topological phases which are used in the rest of the thesis. The chapter also outlines the derivation of the semiclassical equations to include the corrections from the topological terms and discusses how they can be used to reconstruct the topology of the band structure. Chapter 3 describes how topological quantum critical points can be located via local bulk observables in a non-equilibrium scenario and the chapter is based on Roy *et al.* (2017). Wavepacket dynamics in Chern band systems via semiclassics based on Roy *et al.* (2015) forms the content of Chapter 4 whereas results on spatially local quenches as probes of Chern insulators based on Grushin *et al.* (2016a) are contained in Chapter 5. The results on Chern numbers and chiral anomalies in Weyl butterflies and how to probe them can be found in Chapter 6 which is based on Roy *et al.* (2016). Chapter 7 consists of the discussion on disordered Floquet Chern insulators and relies heavily on Roy and Sreejith (2016). Finally, the thesis concludes with the summary of the results presented in it and a discussion of future directions and outlook in Chapter 8.

Chapter 2

Topological systems and semiclassical dynamics

The aim of this chapter is to introduce and describe the models showing topological phases, and some of the related concepts including their semiclassical dynamics which will be used in the rest of the thesis. Topological phases in non-interacting fermionic systems have been the subject of extensive research to the extent that they have been fully classified on the basis of the symmetries of their Hamiltonian and their spatial dimensions [Ryu *et al.* (2010); Chiu *et al.* (2016)]. A periodic table of the topological invariants summarising the classification taken from Chiu *et al.* (2016) is shown in Table 2.1.

The models used in this thesis correspond to the classes BDI and D in one dimension and class A in two dimensions, the corresponding entries of which are highlighted in Table 2.1. In one dimension, we work with the Su-Schrieffer-Heeger chain [Su *et al.* (1979)] (class BDI), the topological phases of which are described by an integer valued bulk winding invariant which corresponds to the number of zero-energy fermionic edge modes in a system with open boundary conditions. In two dimensions, the relevant model is Haldane's honeycomb model [Haldane (1988)] (class A), which is characterized by the integer valued bulk invariant (Chern number) which corresponds to the number of chiral edge modes. Finally, in three dimensions, we work with a simple two-band Weyl semimetal model which can be viewed as a momentum-space stack of Chern insulators.

In Section 2.1 we describe these models followed by a sketch of the derivation of the semiclassical equations of motion for such topological systems in Section 2.2.

class\δ	T	C	S	0	1	2	3	4	5	6	7
A	0	0	0	\mathbb{Z}	0	\mathbb{Z}	0	\mathbb{Z}	0	\mathbb{Z}	0
AIII	0	0	1	0	\mathbb{Z}	0	\mathbb{Z}	0	\mathbb{Z}	0	\mathbb{Z}
AI	+	0	0	\mathbb{Z}	0	0	0	$2\mathbb{Z}$	0	\mathbb{Z}_2	\mathbb{Z}_2
BDI	+	+	1	\mathbb{Z}_2	\mathbb{Z}	0	0	0	$2\mathbb{Z}$	0	\mathbb{Z}_2
D	0	+	0	\mathbb{Z}_2	\mathbb{Z}_2	\mathbb{Z}	0	0	0	$2\mathbb{Z}$	0
DIII	-	+	1	0	\mathbb{Z}_2	\mathbb{Z}_2	\mathbb{Z}	0	0	0	$2\mathbb{Z}$
AII	-	0	0	$2\mathbb{Z}$	0	\mathbb{Z}_2	\mathbb{Z}_2	\mathbb{Z}	0	0	0
CII	-	-	1	0	$2\mathbb{Z}$	0	\mathbb{Z}_2	\mathbb{Z}_2	\mathbb{Z}	0	0
C	0	-	0	0	0	$2\mathbb{Z}$	0	\mathbb{Z}_2	\mathbb{Z}_2	\mathbb{Z}	0
CI	+	-	1	0	0	0	$2\mathbb{Z}$	0	\mathbb{Z}_2	\mathbb{Z}_2	\mathbb{Z}

Table 2.1: Periodic table of topological insulators and superconductors; $\delta \equiv d - D$ where d is the spatial dimension and $D + 1$ is the codimension of the defect. Often the defect is the boundary of the system in which case $\delta = d$. The classification into different classes mentioned in the first column are on the basis of presence or absence of the symmetries time-reversal (T), particle-hole (C), and chiral (S). The \pm in the corresponding columns denote that the anti-unitary symmetries, T and C, upon squaring give \pm , i.e. $T^2 = \pm 1$, and $C^2 = \pm 1$, whereas a 0 denotes the absence of the symmetry. The entries \mathbb{Z} , \mathbb{Z}_2 , $2\mathbb{Z}$, and 0 denote the topological invariants for the corresponding symmetry classes. (Taken from [Chiu *et al.* \(2016\)](#))

2.1 Model Hamiltonians

2.1.1 1D: Su-Schrieffer-Heeger model

The Su-Schrieffer-Heeger (SSH) model is a one-dimensional model of non-interacting fermions described on a bipartite lattice with dimerized hoppings (see Figure 2.1(a)). The model is described by the Hamiltonian

$$\mathcal{H}_{\text{SSH}} = - \sum_l [\lambda_1 \hat{c}_{l,A}^\dagger \hat{c}_{l,B} + \lambda_2 \hat{c}_{l,B}^\dagger \hat{c}_{l+1,A}] + \text{h.c.}, \quad (2.1)$$

where $\hat{c}_{l,A(B)}^\dagger$ is a fermionic creation operator on the site l on sublattice $A(B)$. λ_1 denotes the hopping amplitude between the sublattices A and B on any site l , and λ_2 denotes the hopping amplitude between the sublattice B at site l and sublattice A at site $l + 1$. By means of a lattice Fourier transform, the Hamiltonian in reciprocal space can be represented as

$$\mathcal{H}_{\text{SSH}} = - \sum_k \Psi_k^\dagger H_k \Psi_k = - \sum_k \Psi_k^\dagger (\mathbf{d}_k \cdot \boldsymbol{\sigma}) \Psi_k, \quad (2.2)$$

where $\Psi_k = (\hat{c}_{k,A}, \hat{c}_{k,B})^T$, σ s are the usual Pauli matrices and the vector \mathbf{d}_k is given by

$$\mathbf{d}_k = \{\lambda_1 + \lambda_2 \cos k, \lambda_2 \sin k, 0\}. \quad (2.3)$$

The two level Hamiltonian has an energy spectrum given by

$$\epsilon_{\pm}(k) = \pm \sqrt{(\lambda_1 + \lambda_2 \cos k)^2 + (\lambda_2 \sin k)^2}, \quad (2.4)$$

from which one can immediately see that the spectrum has gap-closing points at $\lambda_1/\lambda_2 = \pm 1$ which are the topological critical points as shown in Figure 2.1(b). Owing to the two-level structure of the model, complete information about the topology of the bands is encoded in the pseudospinor corresponding to the unit vector $\hat{\mathbf{d}}_k = \mathbf{d}_k/|\mathbf{d}_k|$. First, we note that the topological phase of this model is protected by chiral symmetry which can also be interpreted as a sublattice symmetry. Since the two basis states correspond to the two sublattices, the sublattice symmetry operator $\hat{S} = \sigma^z$ and for the symmetry to be present, we need $\hat{S}H_k\hat{S}^\dagger = -H_k$ which automatically implies $d_{k,z} = 0$. Hence, the presence of the sublattice symmetry restricts the vector \mathbf{d}_k to a two-dimensional plane, in our convention, the (x, y) plane. The topology of the band is encoded in the closed curve that the planar vector \mathbf{d}_k traces out as k is varied through the Brillouin zone. A curve that encloses the origin is topologically distinct from one that does not, because one cannot be deformed into the other without making the curve go through the origin which happens to be the topological critical point as at that point $\mathbf{d}_k = 0$ (Figure 2.1(c)). The bulk winding invariant is precisely equal to the number of times the origin is enclosed by the closed curve traced by the vector \mathbf{d}_k . However, one could indeed go from one topological phase to the other without closing the gap or going through a critical point the sublattice symmetry is allowed to be broken. It would amount to having $d_{k,z} \neq 0$ and the curve traced out by \mathbf{d}_k would not be planar any more. As a result, the curve could be lifted out of its plane and put back in such a way that the origin is not enclosed in its initial configuration but enclosed in the final configuration of the curve (Figure 2.1(e)).

The different windings of the vector \mathbf{d}_k can be expressed mathematically via the winding number

$$\nu = \frac{1}{2\pi} \int_0^{2\pi} dk \left(\hat{\mathbf{d}}_k \times \frac{d\hat{\mathbf{d}}_k}{dk} \right)_z = \begin{cases} 1 & \text{for } |\lambda_1/\lambda_2| < 1; \\ 0 & \text{for } |\lambda_1/\lambda_2| > 1. \end{cases} \quad (2.5)$$

For a system with open boundary conditions, the topological nature of the band results in zero energy modes localised at the edges of the chain as shown in Figure 2.1(d). It is possible to build a simple physical picture of these edge modes in the fully dimerised limit. In the limit of $\lambda_1 = 0$, corresponding to the topological phase, the A sublattice on the first site and the B sublattice on the last site are decoupled from the entire chain and hence host a pair of zero energy modes, each localised on

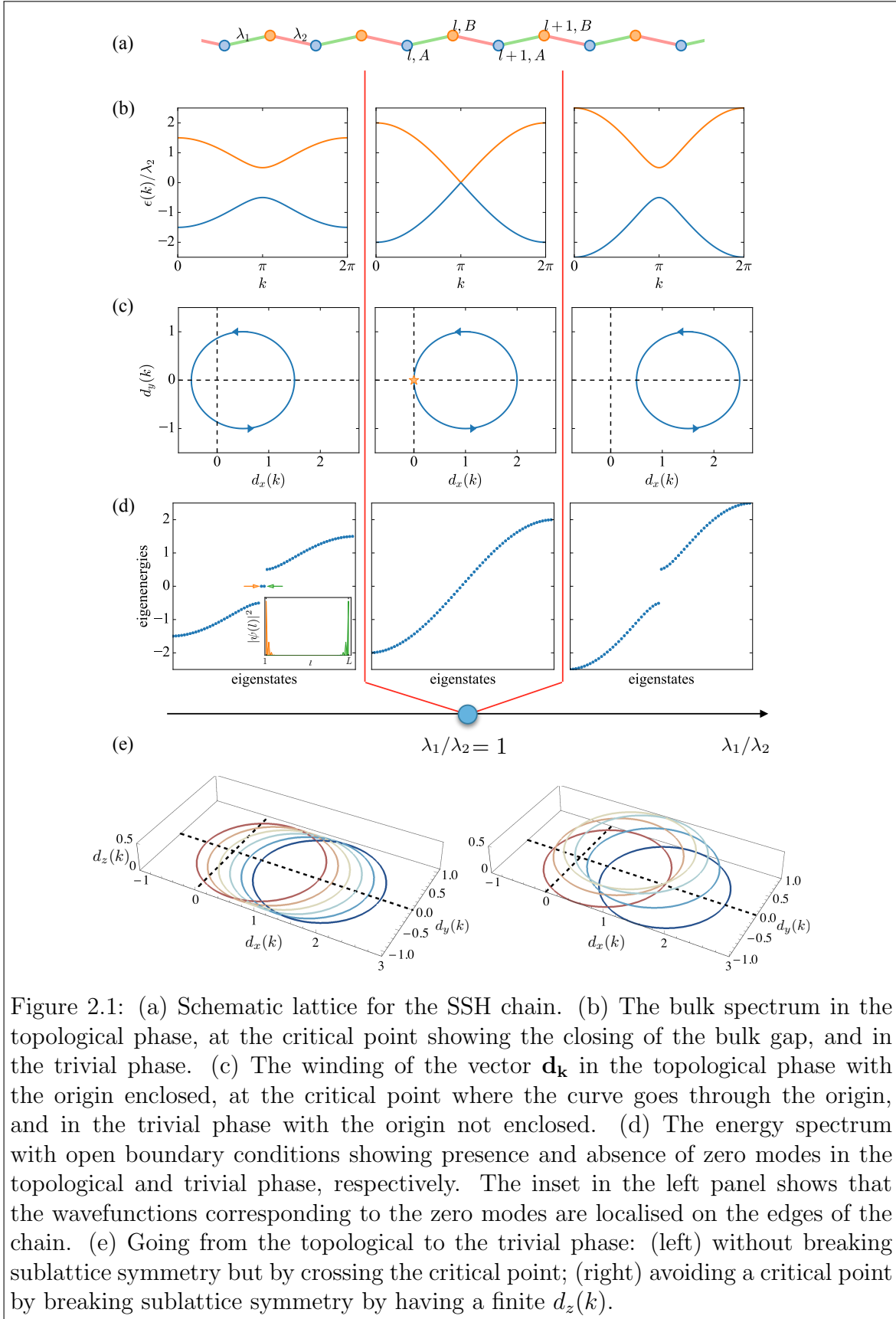


Figure 2.1: (a) Schematic lattice for the SSH chain. (b) The bulk spectrum in the topological phase, at the critical point showing the closing of the bulk gap, and in the trivial phase. (c) The winding of the vector \mathbf{d}_k in the topological phase with the origin enclosed, at the critical point where the curve goes through the origin, and in the trivial phase with the origin not enclosed. (d) The energy spectrum with open boundary conditions showing presence and absence of zero modes in the topological and trivial phase, respectively. The inset in the left panel shows that the wavefunctions corresponding to the zero modes are localised on the edges of the chain. (e) Going from the topological to the trivial phase: (left) without breaking sublattice symmetry but by crossing the critical point; (right) avoiding a critical point by breaking sublattice symmetry by having a finite $d_z(k)$.

one of them. On moving away from this limit, these edge modes stay robust although their localisation length increases.

2.1.2 2D: Haldane's honeycomb model and related model on square lattice

Haldane's honeycomb model, as the name suggests, is defined on a honeycomb lattice and is described by the Hamiltonian

$$\mathcal{H}_{\text{Haldane}} = -J_1 \sum_{\langle i,j \rangle} [\hat{c}_i^\dagger \hat{c}_j + \text{h.c.}] - J_2 \sum_{\langle\langle i,j \rangle\rangle} [e^{i\phi} \hat{c}_i^\dagger \hat{c}_j + \text{h.c.}] + \sum_i M_i \hat{c}_i^\dagger \hat{c}_i, \quad (2.6)$$

where the first term describes real hoppings between nearest neighbours $\langle i, j \rangle$, the second term describes complex hoppings between next-nearest neighbours $\langle\langle i, j \rangle\rangle$ with the fermion picking up a phase ϕ when hopping along the direction shown by the arrows in Figure 2.2(a), and the third term describes a staggered sublattice mass with $M_i = \pm M$ for a site i on sublattice $A(B)$. The complex next-nearest hopping breaks time-reversal symmetry and induces a topological gap in the spectrum, also known as the Haldane mass. On the other hand, the staggered sublattice mass breaks inversion symmetry and induces a trivial gap in the spectrum, which is often dubbed as the Semenoff mass. The competition between the two kinds of masses allows for a phase diagram with both topological and trivial phases separated by topological phase transitions as shown in Figure 2.2(b). The corresponding set of critical points can be located by analysing the gap closings of the spectrum obtained from the Hamiltonian (2.6) in reciprocal space which owing the bipartite nature of the honeycomb lattice can be expressed as $\mathcal{H}_{\text{Haldane}}(\mathbf{k}) = d_{0,\mathbf{k}} \mathbb{I}_2 + \mathbf{d}_{\mathbf{k}} \cdot \boldsymbol{\sigma}$ with

$$\begin{aligned} d_{0,\mathbf{k}} &= -2J_2 \cos \phi [\cos(\mathbf{k} \cdot \mathbf{n}_1) + \cos(\mathbf{k} \cdot \mathbf{n}_2) + \cos(\mathbf{k} \cdot \mathbf{n}_3)]; \\ d_{\mathbf{k},x} &= -J_1 [\cos(\mathbf{k} \cdot \mathbf{e}_1)] + [\cos(\mathbf{k} \cdot \mathbf{e}_2)] + [\cos(\mathbf{k} \cdot \mathbf{e}_3)]; \\ d_{\mathbf{k},y} &= -J_1 [\sin(\mathbf{k} \cdot \mathbf{e}_1)] + [\sin(\mathbf{k} \cdot \mathbf{e}_2)] + [\sin(\mathbf{k} \cdot \mathbf{e}_3)]; \\ d_{\mathbf{k},z} &= -2J_2 \sin \phi [\sin(\mathbf{k} \cdot \mathbf{n}_1) + \sin(\mathbf{k} \cdot \mathbf{n}_2) + \sin(\mathbf{k} \cdot \mathbf{n}_3)] + M, \end{aligned} \quad (2.7)$$

where \mathbf{e}_i s and \mathbf{n}_i s are vectors connecting nearest neighbours and next-nearest neighbours, respectively, and are given by

$$\begin{aligned} \mathbf{e}_1 &= (0, 1); \quad \mathbf{e}_2 = (-\sqrt{3}/2, -1/2); \quad \mathbf{e}_3 = (\sqrt{3}/2, -1/2); \\ \mathbf{n}_1 &= (\sqrt{3}, 0); \quad \mathbf{n}_2 = (-\sqrt{3}/2, -3/2); \quad \mathbf{n}_3 = (\sqrt{3}/2, 3/2). \end{aligned} \quad (2.8)$$

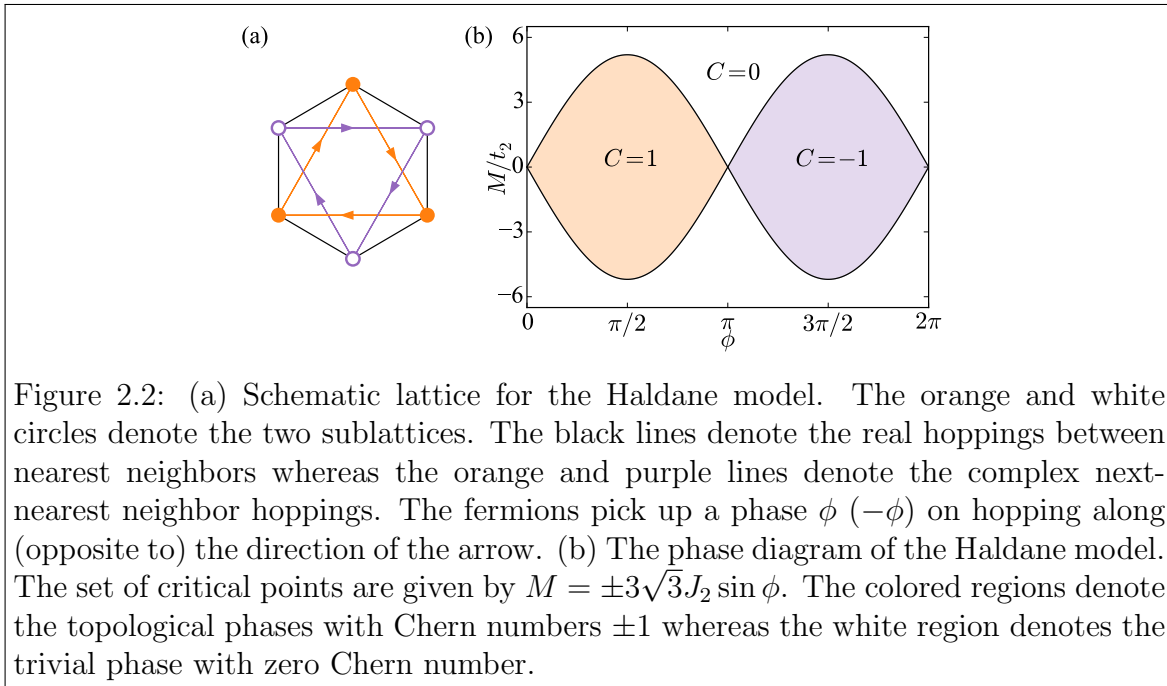


Figure 2.2: (a) Schematic lattice for the Haldane model. The orange and white circles denote the two sublattices. The black lines denote the real hoppings between nearest neighbors whereas the orange and purple lines denote the complex next-nearest neighbor hoppings. The fermions pick up a phase ϕ ($-\phi$) on hopping along (opposite to) the direction of the arrow. (b) The phase diagram of the Haldane model. The set of critical points are given by $M = \pm 3\sqrt{3}J_2 \sin \phi$. The colored regions denote the topological phases with Chern numbers ± 1 whereas the white region denotes the trivial phase with zero Chern number.

The eigenvalues of the two-level reciprocal space Hamiltonian, $\epsilon_{\pm}(\mathbf{k}) = d_{0,\mathbf{k}} \pm |\mathbf{d}_{\mathbf{k}}|$ describe the energy dispersion of the bands and the eigenspinors $|u_{\pm}(\mathbf{k})\rangle$ encode the topology of the bands.

Locating the gap closings in the spectrum by setting $|\mathbf{d}_{\mathbf{k}}| = 0$ yields the set of critical points as $M = \pm 3\sqrt{3}J_2 \sin \phi$. The topology of the bands is reflected in the Chern number which can be calculated from the eigenspinors $|u(\mathbf{k})\rangle$ as follows. The Chern number is given by the net flux of the Berry curvature, $\Omega_{\mathbf{k}}$ through the entire Brillouin zone as

$$\mathcal{C} = \frac{1}{2\pi} \int_{BZ} dk_x dk_y \Omega_{\mathbf{k}}^z, \quad (2.9)$$

where the Berry curvature can be interpreted as an effective magnetic field but in momentum space which is explained in more details in Section 2.2.1. The Berry curvature can be obtained by taking a curl (in momentum space) of the Berry connection, $\Omega_{\mathbf{k}} = \nabla_{\mathbf{k}} \times \mathcal{A}_{\mathbf{k}}$, which is effectively the corresponding vector potential and can be obtained from the eigenspinors as

$$\mathcal{A}_{\mathbf{k}} = i\langle u_{\mathbf{k}} | \nabla_{\mathbf{k}} | u_{\mathbf{k}} \rangle. \quad (2.10)$$

Although Haldane's honeycomb model has emerged as the archetypal example of a Chern insulator model and also has been experimentally realized in a cold atom experiment [Jotzu *et al.* (2014)], an intimately related model of a Chern insulator on

a square lattice with a two-site unit cell, owing to its simplicity, is also extensively used in the thesis. The model is described by the Hamiltonian

$$\mathcal{H}_{\text{CI}} = \left[- \sum_{\mathbf{r}} \left(\Psi_{\mathbf{r}}^{\dagger} \frac{J_1 \sigma^z + i J_2 \sigma^x}{2} \Psi_{\mathbf{r}+\hat{x}} + \Psi_{\mathbf{r}}^{\dagger} \frac{J_1 \sigma^z + i J_2 \sigma^y}{2} \Psi_{\mathbf{r}+\hat{y}} - \frac{M_0}{2} \Psi_{\mathbf{r}}^{\dagger} \sigma^z \Psi_{\mathbf{r}} \right) \right] + \text{h.c.} \quad (2.11)$$

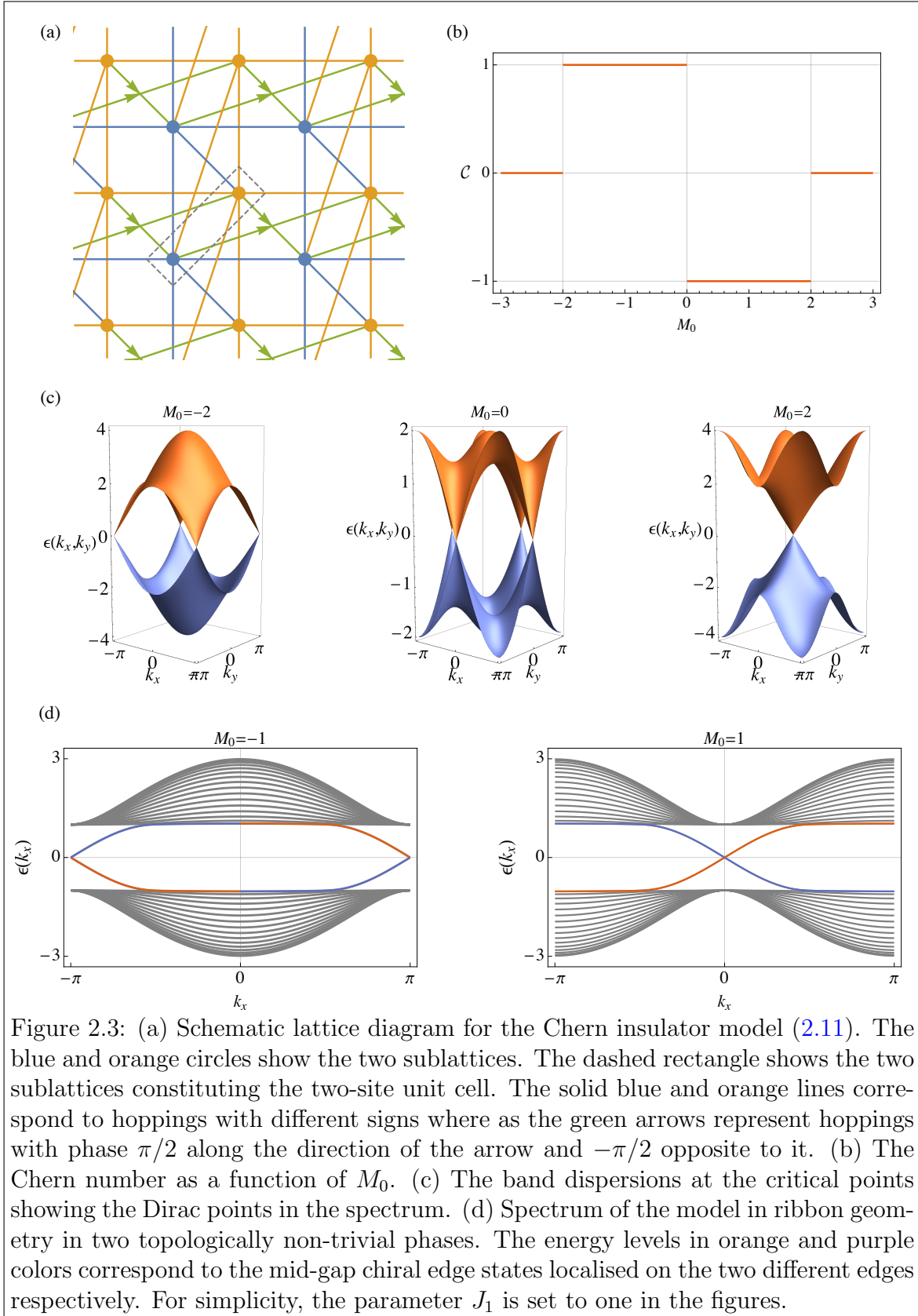
For simplicity we set $J_2 = J_1$. The configuration of hoppings realising the model is schematically shown in Figure 2.3(a). As in Haldane's honeycomb model, time-reversal symmetry is broken by complex hoppings. The one-parameter phase diagram of the model characterised in terms of the Chern number as a function of the parameter M_0 is shown in Figure 2.3(b). As was done for Haldane's honeycomb model, the topological critical points of the model can be found by analysing the gap closings of the bulk spectrum which could be obtained from the two-level reciprocal space Hamiltonian $\mathcal{H}_{\text{CI}}(\mathbf{k}) = \mathbf{d}_{\mathbf{k}} \cdot \boldsymbol{\sigma}$ with

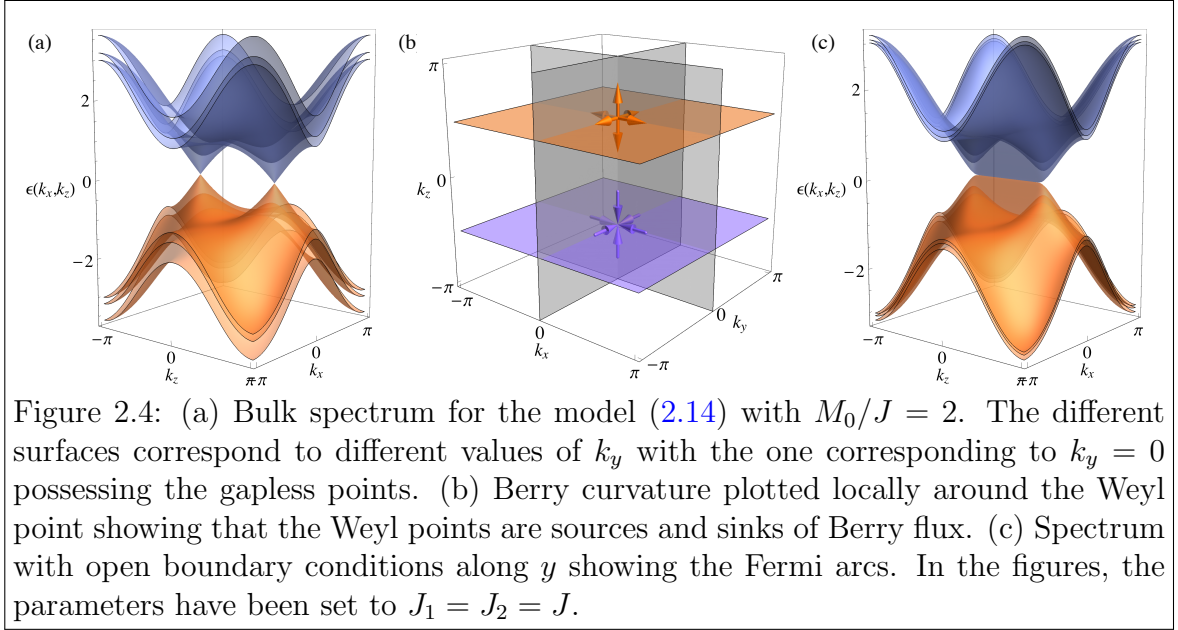
$$\mathbf{d}_{\mathbf{k}} = \{-J_1 \sin k_x, -J_1 \sin k_y, M_0 - J_1 \cos k_x - J_1 \cos k_y\}. \quad (2.12)$$

The model has critical points at $M_0/J_1 = -2$ and $M_0/J_1 = 2$ with one Dirac point in the spectrum at $\mathbf{k} = (\pi, \pi)$ and $\mathbf{k} = (0, 0)$, respectively, where the Chern number changes by one from zero to ± 1 . The model also has a critical point at $M_0/J_1 = 0$ with two Dirac points in the spectrum at $\mathbf{k} = (\pi, 0)$ and $\mathbf{k} = (0, \pi)$, where the Chern number changes by two from -1 to 1 . The bulk spectra at these critical points are shown in Figure 2.3(c). In the topological phase, the model hosts mid-gap chiral edge states which can be seen in the energy spectrum of the model by putting it on a ribbon geometry, *i.e.* with open boundary conditions along y but periodic boundary conditions along x . The resulting spectrum as a function of k_x (which remains a good quantum number) is shown in Figure 2.3(d) which also shows that the edge states localised on one of the edges (say the left edge shown by the orange lines) have opposite chiralities in the regimes corresponding to the Chern number being 1 or -1 . The edge state localised on the right edge has a chirality which is opposite to that of the edge state in the left edge.

2.1.3 3D: A Weyl semimetal model

A Weyl semimetal is a three-dimensional system featuring a gapless bulk spectrum with linear band crossings at the so-called *Weyl points*. Consequently, the low energy excitations in the linear regime are Weyl fermions, with a vanishing density of states at the gapless point, hence the name Weyl semimetal. Owing to the no-go theorem





by Nielsen and Ninomiya (1981), the Weyl points always appear in pairs in a lattice system with different chiralities, and the separation between two Weyl points of a pair in momentum space is related to breaking of time-reversal symmetry. Hence, intuitively one can guess that a Weyl semimetal can be constructed by stacking two-dimensional time-reversal symmetry-broken systems, for instance, Chern insulators. The Weyl semimetal model considered in this thesis is indeed constructed by stacking many layers of the two-dimensional Chern insulator (2.11) along the third direction such that the Hamiltonian describing the system is

$$\mathcal{H}_{\text{WSM}} = \left[- \sum_{\mathbf{r}} \left(\Psi_{\mathbf{r}}^{\dagger} \frac{J_1 \sigma^z + i J_2 \sigma^x}{2} \Psi_{\mathbf{r}+\hat{x}} + \Psi_{\mathbf{r}}^{\dagger} \frac{J_1 \sigma^z + i J_2 \sigma^y}{2} \Psi_{\mathbf{r}+\hat{y}} + J_1 \Psi_{\mathbf{r}}^{\dagger} \frac{\sigma^z}{2} \Psi_{\mathbf{r}+\hat{z}} - \frac{M_0}{2} \Psi_{\mathbf{r}}^{\dagger} \sigma^z \Psi_{\mathbf{r}} \right) \right] + \text{h.c.} \quad (2.13)$$

In momentum space, the Hamiltonian again has a simple two-level $\mathbf{d}_{\mathbf{k}} \cdot \boldsymbol{\sigma}$ form with

$$\mathbf{d}_{\mathbf{k}} = \{-J_2 \sin k_x, -J_2 \sin k_y, M_0 - J_1 \cos k_x - J_1 \cos k_y - J_1 \cos k_z\}. \quad (2.14)$$

For simplicity, we set $J_1 = J_2 = J$. From Eq. (2.14), one can understand the Weyl semimetal Hamiltonian as a family of Chern insulator Hamiltonians depending parametrically on k_z . The Weyl points in the three-dimensional Brillouin zone can be interpreted as points of topological phase transitions in the family of Chern insulator Hamiltonians. Hence, if one considers the Weyl semimetal Hamiltonian as a momentum space stack (along k_z) of Chern insulators with a k_z -dependent Chern number

$\mathcal{C}(k_z)$, then the Chern number must change across a Weyl point. This interpretation gives a simple understanding of why the Weyl points must appear in pairs in a lattice system. If there exists just one Weyl point in the spectrum, then $\mathcal{C}(k_z)$ would change only once across the Brillouin zone, which however is forbidden by the periodicity of the Brillouin zone. Hence, it naturally implies that there must exist another Weyl point in the spectrum, and more importantly, of different chirality. Interpreting the Weyl semimetal as a Chern insulator stack also provides a simple picture of one of the most exotic properties of a Weyl semimetal, namely surface Fermi arcs. The momentum slices corresponding to a finite value of $\mathcal{C}(k_z)$ possess chiral edge states in a system with open boundary conditions. However these states only extend between the Weyl points in momentum space, and the Fermi surface on the surface of the sample is just a line between the two Weyl points, and hence it is a Fermi arc.

The above features are summarized in Figure 2.4 for the model (2.13). The Hamiltonian has a gapped bulk spectrum for $|M_0/J| > 3$. However, for $1 < M_0/J < 3$ and $-3 < M_0/J < -1$, it has a pair of Weyl points at $\mathbf{k} = \{0, 0, \pm \cos^{-1}(M_0/J - 2)\}$ and $\mathbf{k} = \{\pi, \pi, \pm \cos^{-1}(M_0/J + 2)\}$, respectively, whereas for $|M_0/J| < 1$, the model has two pairs of Weyl points at $\mathbf{k} = \{\pi, 0, \pm \cos^{-1}(M_0/J)\}$ and $\mathbf{k} = \{0, \pi, \pm \cos^{-1}(M_0/J)\}$. The spectrum for $M_0/J = 2$ with the Weyl points is shown in Figure 2.4(a). That these Weyl points are sources and sinks of Berry curvature flux can be shown in Figure 2.4(b) by plotting the Berry curvature $\Omega_{\mathbf{k}}$ locally around the Weyl points. Finally the spectrum with open boundary conditions along y is shown in Figure 2.4(c) which shows the surface Fermi arcs between the two Weyl points.

2.2 Semiclassical equations of motion

In the context of cold atomic systems, since the probes for the topological nature of the realised band structures often involve dynamics of wavepackets, the framework of semiclassical equations of motion is quite natural for analysing them theoretically. Before going into the derivation of the semiclassical equations of motion, it is useful to state them,

$$\begin{aligned}\dot{\mathbf{r}} &= \nabla_{\mathbf{k}} \epsilon_{n,\mathbf{k}} + \dot{\mathbf{k}} \times \Omega_{n,\mathbf{k}}, \\ \dot{\mathbf{k}} &= \mathbf{F} = \mathbf{E} + \dot{\mathbf{r}} \times \mathbf{B},\end{aligned}\tag{2.15}$$

where $\epsilon_{n,\mathbf{k}}$ and $\Omega_{n,\mathbf{k}}$ are, respectively, the energy dispersion and the Berry curvature of the n^{th} band, and \mathbf{F} is the force which could be due to electromagnetic fields \mathbf{E} and \mathbf{B} , or due to gravity in tilted lattices.

2.2.1 Berry curvature as a magnetic field in momentum space

Note that in Eq. (2.15), the Berry curvature appears in the form of the magnetic field but in momentum space. This follows from the invariance of the Bloch wavefunctions under phase shifts local in momentum, in analogy to the relation between local $U(1)$ phase symmetry in real space and gauge fields. The analogy can be made more explicit as follows. In the rest of the derivations in this chapter, we set $\hbar = 1 = c = e$ for simplicity.

Consider $\psi(\mathbf{r}, t)$ to be the solution of the Schrödinger equation in the presence of a scalar potential $\Phi(\mathbf{r}, t)$ and a vector potential $\mathbf{A}(\mathbf{r}, t)$ such that the operators $-i\nabla$ and $i\partial_t$ are transformed via minimal coupling respectively to $-i\nabla - \mathbf{A}$ and $i\partial_t - \Phi$,

$$(i\partial_t - \Phi)\psi(\mathbf{r}, t) = [(-i\nabla - \mathbf{A})^2] \psi(\mathbf{r}, t) + V(\mathbf{r})\psi(\mathbf{r}, t). \quad (2.16)$$

A transformation under a local phase shift $\phi(\mathbf{r}, t)$ is defined as $\psi'(\mathbf{r}, t) = e^{i\phi(\mathbf{r}, t)}\psi(\mathbf{r}, t)$. Under this transformation, the Schrödinger equation (2.16) stays invariant provided the scalar and vector potentials are also transformed as

$$\begin{aligned} \Phi'(\mathbf{r}, t) &= \Phi(\mathbf{r}, t) - \partial_t\phi(\mathbf{r}, t), \\ \mathbf{A}'(\mathbf{r}, t) &= \mathbf{A}(\mathbf{r}, t) + \nabla\phi(\mathbf{r}, t). \end{aligned} \quad (2.17)$$

The transformation of Φ and \mathbf{A} in Eq. (2.17) is simply a gauge transformation and does not change any physics as it keeps the physical electric and magnetic fields the same. However, the important point is that the local $U(1)$ phase symmetry of the wavefunction is directly related to a gauge field.

In case of a lattice system, the potential $V(\mathbf{r})$ is periodic in space and the eigenfunctions of the Schrödinger equation are described by Bloch wavefunctions $\psi_{n,\mathbf{k}}(\mathbf{r}) = u_{n,\mathbf{k}}(\mathbf{r})e^{i\mathbf{k}\cdot\mathbf{r}}$. It turns out that in such a scenario, the Schrödinger equation stays invariant under a local-in-momentum phase shift of the form

$$\psi'_{n,\mathbf{k}}(\mathbf{r}) = e^{i\phi(\mathbf{k})}\psi_{n,\mathbf{k}}(\mathbf{r}) = e^{i\phi(\mathbf{k})}u_{n,\mathbf{k}}(\mathbf{r})e^{i\mathbf{k}\cdot\mathbf{r}}, \quad (2.18)$$

provided there is no scattering between Bloch waves with different momentum. This requirement is indeed satisfied in non-interacting lattice systems with translation symmetry, *i.e.* in the absence of disorder or impurities.

Hence, in direct analogy to the local-in-space phase symmetry of the solutions of the Schrödinger equation as described in Eq (2.17), the local-in-momentum phase symmetry of the Bloch wavefunctions would imply the presence of intrinsic gauge fields but in momentum space. The vector potential corresponding to the magnetic field

in momentum space can be identified with the Berry connection (2.10) by analyzing the position operator in momentum space for Bloch wavefunctions, the derivation of which is as follows.

Consider a general wavefunction which is a superposition of Bloch waves as

$$\Psi(\mathbf{r}) = \sum_n \int_{BZ} d\mathbf{k} \alpha_n(\mathbf{k}) \psi_{n,\mathbf{k}}(\mathbf{r}) = \sum_n \int_{BZ} d\mathbf{k} \alpha_n(\mathbf{k}) u_{n,\mathbf{k}}(\mathbf{r}) e^{i\mathbf{k}\cdot\mathbf{r}}. \quad (2.19)$$

The operator in question, denoted by $\hat{\mathbf{r}}$ is defined via the relation

$$\begin{aligned} \mathbf{r}\Psi(\mathbf{r}) &= \sum_n \int_{BZ} d\mathbf{k} \hat{\mathbf{r}} \alpha_n(\mathbf{k}) u_{n,\mathbf{k}}(\mathbf{r}) e^{i\mathbf{k}\cdot\mathbf{r}} \\ &= \sum_n \int_{BZ} d\mathbf{k} \alpha_n(\mathbf{k}) u_{n,\mathbf{k}}(\mathbf{r}) (-i\nabla_{\mathbf{k}} e^{i\mathbf{k}\cdot\mathbf{r}}) \\ &= \sum_n \int_{BZ} d\mathbf{k} i\nabla_{\mathbf{k}} [\alpha_n(\mathbf{k}) u_{n,\mathbf{k}}(\mathbf{r})] e^{i\mathbf{k}\cdot\mathbf{r}} \end{aligned} \quad (2.20)$$

where in the last step, the periodicity of the Bloch wavefunctions in the Brillouin zone has been exploited. The completeness of the Bloch wavefunctions, $\sum_m u_{m,\mathbf{k}}^*(\mathbf{r}') u_{m,\mathbf{k}}(\mathbf{r}') = \delta(\mathbf{r} - \mathbf{r}')$ is now invoked to obtain from Eq. (2.20)

$$\begin{aligned} \mathbf{r}\Psi(\mathbf{r}) &= \sum_n \int_{BZ} d\mathbf{k} \left[(i\nabla_{\mathbf{k}} \alpha_n(\mathbf{k})) \psi_{n,\mathbf{k}}(\mathbf{r}) \right. \\ &\quad \left. + \alpha_n(\mathbf{k}) \sum_m u_{m,\mathbf{k}}(\mathbf{r}) \left(\int d\mathbf{r}' u_{m,\mathbf{k}}^*(\mathbf{r}') i\nabla_{\mathbf{k}} u_{n,\mathbf{k}}(\mathbf{r}') \right) e^{i\mathbf{k}\cdot\mathbf{r}} \right]. \end{aligned} \quad (2.21)$$

Often in semiclassical analyses, fully filled bands are considered and the dynamics are considered to be slow enough such that non-adiabatic effects resulting from inter-band transitions are suppressed and hence are neglected. With these assumptions, and using the definition of the Berry connection from Eq. (2.10), Eq. (2.21) can be recast as

$$\mathbf{r}\Psi(\mathbf{r}) = \sum_n \int_{BZ} d\mathbf{k} [(i\nabla_{\mathbf{k}} \alpha_n(\mathbf{k})) \psi_{n,\mathbf{k}}(\mathbf{r}) - \mathcal{A}_{n,\mathbf{k}} \alpha_n(\mathbf{k}) \psi_{n,\mathbf{k}}], \quad (2.22)$$

from which the position operator can be read off as

$$\hat{\mathbf{r}} = i\nabla_{\mathbf{k}} - \mathcal{A}_{n,\mathbf{k}}. \quad (2.23)$$

The stark resemblance to the momentum operator in the presence of a vector potential in real space $\hat{\mathbf{k}} = -i\nabla_{\mathbf{k}} - \mathbf{A}$ immediately leads to the identification of the Berry connection as an effective vector potential in momentum space. Further since the gauge invariant Berry curvature is the curl of the Berry connection, it can indeed be interpreted as an effective magnetic field in momentum space.

2.2.2 Anomalous Hall velocity

While the semiclassical equations of motion (2.15) seem rather obvious once the identification of the Berry curvature as a momentum space magnetic field is made, a more systematic derivation starting from a quantum mechanical treatment is in order, which is sketched in the following.

The equation of motion for the momentum is analyzed first. Consider the Hamiltonian in the presence of an electromagnetic field,

$$\mathcal{H}(\hat{\mathbf{k}}, \hat{\mathbf{r}}) = \mathcal{H}_{\text{kin}}(-i\nabla_{\mathbf{r}} - \mathbf{A}(\mathbf{r})) + \Phi(\mathbf{r}), \quad (2.24)$$

where \mathcal{H}_{kin} is the kinetic energy part of the Hamiltonian which depends only on momentum. Using Ehrenfest's theorem the equation of motion for the expectation value of the momentum can be written as

$$\begin{aligned} \frac{dk_{\mu}}{dt} &= \langle i[\mathcal{H}, -i\partial_{r_{\mu}} - A_{\mu}(\mathbf{r})] \rangle = \langle -\partial_{r_{\mu}}\mathcal{H} - dA_{\mu}/dt \rangle \\ &= \langle -\partial_{r_{\mu}}\mathcal{H}_{\text{kin}} - \partial_{r_{\mu}}\Phi - dA_{\mu}/dt \rangle \\ &= \left\langle -\frac{\partial\mathcal{H}}{\partial\hat{k}_{\nu}}\frac{\partial\hat{k}_{\nu}}{\partial r_{\mu}} - \frac{\partial\Phi}{\partial r_{\mu}} - \frac{dA_{\mu}}{dt} \right\rangle \\ &= \left\langle \frac{\partial\mathcal{H}}{\partial\hat{k}_{\nu}}\frac{\partial A_{\nu}}{\partial r_{\mu}} - \frac{\partial\Phi}{\partial r_{\mu}} - \frac{\partial A_{\mu}}{\partial r_{\nu}}\frac{dr_{\nu}}{dt} \right\rangle. \end{aligned} \quad (2.25)$$

In Eq. (2.25), one can then use Hamilton's equations to identify $\partial_{k_{\nu}}\mathcal{H} = dr_{\nu}/dt$ to finally obtain

$$\frac{dk_{\mu}}{dt} = -\partial_{r_{\mu}}\Phi + (\dot{\mathbf{r}} \times (\nabla \times \mathbf{A}))_{\mu} = E_{\mu} + (\dot{\mathbf{r}} \times \mathbf{B})_{\mu}, \quad (2.26)$$

which is nothing but the Lorentz force.

In order to analyse the equation of motion for the position, we go to the momentum space, where we consider the Hamiltonian $\mathcal{H}(\mathbf{k}, i\nabla_{\mathbf{k}} - \mathcal{A}_{\mathbf{k}})$. Also for Bloch wavefunctions we consider $\langle \mathcal{H} \rangle = \epsilon_{\mathbf{k}}$ where $\epsilon_{\mathbf{k}}$ is the dispersion for the band.

Similar to Eq. (2.25) we start with

$$\begin{aligned} \frac{dr_{\mu}}{dt} &= \langle i[\mathcal{H}, i\partial_{k_{\mu}} - \mathcal{A}_{\mathbf{k},\mu}] \rangle \\ &= \left\langle \frac{\partial\mathcal{H}}{\partial k_{\mu}} - \frac{d\mathcal{A}_{\mathbf{k},\mu}}{dt} \right\rangle \\ &= \partial_{k_{\mu}}\epsilon_{\mathbf{k}} + \left\langle \frac{\partial\mathcal{H}}{\partial\hat{r}_{\nu}}\frac{\partial\hat{r}_{\nu}}{\partial k_{\mu}} - \frac{\partial\mathcal{A}_{\mathbf{k},\mu}}{\partial k_{\nu}}\frac{dk_{\nu}}{dt} \right\rangle. \end{aligned} \quad (2.27)$$

As before, we use Hamilton's equations ($\partial_{r_\mu} \mathcal{H} = -\dot{k}_\mu$) and the expression for $\hat{\mathbf{r}}$ (2.23) in Eq. (2.27) to obtain

$$\frac{dr_\mu}{dt} = \partial_{k_\mu} \epsilon_{\mathbf{k}} + (\dot{\mathbf{k}} \times (\nabla_{\mathbf{k}} \times \mathcal{A}))_\mu = \partial_{k_\mu} \epsilon_{\mathbf{k}} + (\dot{\mathbf{k}} \times \boldsymbol{\Omega}_{\mathbf{k}})_\mu. \quad (2.28)$$

Hence, Eqs. (2.26) and (2.28) complete the derivation of the semiclassical equations of motion stated in Eq. (2.15). It is important to note that the equation for $\dot{\mathbf{r}}$ has an additional term coming purely from the Berry curvature whose contribution to the velocity is perpendicular to the direction of the force. This is often dubbed as the *anomalous Hall velocity* [Xiao *et al.* (2010); Nagaosa *et al.* (2010)]. The connection between the Hall velocity and the quantised Hall conductivity becomes immediately clear once the semiclassical response is integrated over the entire Brillouin zone and is summed over all fully occupied bands. Consider the case of a uniform electric field $E\hat{\mathbf{x}}$ such that the velocity of an electron in the n^{th} band at momentum \mathbf{k} is given by

$$v_{n,\mathbf{k}} = \frac{dr_{n,\mathbf{k}}}{dt} = \nabla_{\mathbf{k}} \epsilon_{n,\mathbf{k}} + E\hat{\mathbf{x}} \times \boldsymbol{\Omega}_{n,\mathbf{k}}, \quad (2.29)$$

such that the net current is given by

$$\mathbf{j} = \sum_{n \in \text{filled bands}} \frac{1}{2\pi} \int_{BZ} d\mathbf{k} [\nabla_{\mathbf{k}} \epsilon_{n,\mathbf{k}} + E\hat{\mathbf{x}} \times \boldsymbol{\Omega}_{n,\mathbf{k}}] = E \sum_n \mathcal{C}_n \hat{\mathbf{y}}, \quad (2.30)$$

where the first term drops off due to the periodicity of the dispersion over the Brillouin zone and \mathcal{C}_n is the Chern number of the n^{th} band. Hence the Hall conductivity is the sum of the Chern numbers of all the filled bands, which is concomitant with the bulk-boundary correspondence that the number of chiral edge modes in a bulk gap is the sum of the Chern numbers of all the bulk bands below the gap.

Chapter 3

Non-equilibrium signatures of topological criticality in local bulk observables

A quantum phase transition is typically associated with a non-analytic change of the physical properties of the system characterized by a local order parameter measured over the ground state of its Hamiltonian as a function of a tuning parameter [Sachdev (2011); Suzuki *et al.* (2013)]. The signatures of the criticality are also generically not expected to be present in excited eigenstates with finite energy density. As mentioned in Chapter 1, that there can exist order in nature beyond the traditional framework of local order was already realized by Wegner's groundbreaking work on gauge theories [Wegner (1971)] and the discovery of quantum Hall effect [von Klitzing *et al.* (1980)]. Such phases of matter have recently gained a lot of importance under the umbrella of *topological order*. A topological quantum phase transitions does not have a *local* order parameter in the bulk which can distinguish the two adjacent phases. Different topological phases are characterized by different values of certain topological invariants [Hasan and Kane (2010); Qi and Zhang (2011); Kitaev *et al.* (2009); Ryu *et al.* (2010); Zak (1989); Thouless *et al.* (1982)] and non-local string order parameters [Affleck *et al.* (1987, 1988)].

However, as discussed in this chapter, there exists an interesting connection between topological quantum criticality and its signatures in out-of-equilibrium states which are manifestly outside the ground state manifold of the family of Hamiltonians considered. *Local observables in the bulk* can show *non-analytic* signatures marking the ground-state topological quantum criticality, where the non-analyticities are observed over a family of highly excited states with *finite energy densities*. Specifically, this chapter discusses the results using non-interacting fermionic models where topo-

logical quantum phase transitions can entail conventional quantum phase transitions (described by bulk order parameters) via transformations (such as Jordan-Wigner) which are crucially *non-local*. Identifying the (transformed) bulk order parameter, and hence the transition, turns out to be difficult. The protocol described in this chapter provides a robust prescription for locating the critical point using local observables in the *natural* basis, where the phase transition is topological and not described by local order. Interestingly, the signature is found to be absent in a case of non-topological gap closing, constructed in this work, which corresponds to no real phase transitions, indicating its ability to distinguish between a true phase transition point and an “accidental” gap closing.

The results are put on a concrete footing using models described in Chapter 2, namely, the Su-Schrieffer-Heeger model [Su *et al.* (1979)] (SSH) in one dimension which belong to the symmetry class BDI, and Haldane’s honeycomb model [Haldane (1988)] in two dimension, which belongs to class A. Additionally, some results are also discussed for the Kitaev p-wave superconducting chain [Kitaev (2001)], belonging to symmetry class D, in order to show the validity of the results for other symmetry classes.

3.1 Non-equilibrium protocol

The non-equilibrium protocol consists of the following steps [Bhattacharyya *et al.* (2015)]:

- Consider a family of Hamiltonians parametrised by a coupling λ , such that there is a topological quantum phase transition as a function of λ at the critical point, $\lambda = \lambda_c$.
- Start with a state characterised by some initial Hamiltonian $\mathcal{H}(\lambda_i)$ (for example, one of its eigenstates or a finite temperature state), and quench it by instantaneously changing the parameter from λ_i to λ_f .
- Following the quench, the system relaxes to a steady state, which can be effectively described by a density matrix, $\rho(\lambda_f)$, diagonal in the eigenbasis of $\mathcal{H}(\lambda_f)$ for the purpose of computing expectation values of local observables on it (*corresponding to the diagonal ensemble*) [Rigol *et al.* (2008)].
- Track the expectation values of local bulk observables $\langle \hat{\mathcal{O}} \rangle = \text{Tr}[\hat{\mathcal{O}}\rho(\lambda_f)]$ as a function of λ_f .

It is found that $\langle \hat{\mathcal{O}} \rangle$ reflects the equilibrium topological quantum critical points via a non-analyticity in its behavior at $\lambda_f = \lambda_c$. A large class of initial states can be used for the quench, since the sufficient condition for obtaining the signature turns out to be an occupation gradient across the energy at the gapless modes, which can be achieved by controlling the filling fraction or by any finite temperature thermal state. This also makes the proposal pertinent for realizations in experiments similar to a recent quench experiment [Fläschner *et al.* (2016)].

3.2 General structure in momentum space

Hamiltonians of the aforementioned one- and two-dimensional systems are translation invariant and bipartite in nature, and can hence be represented in Fourier space by independent two-level systems - each corresponding to a particular momentum mode. In terms of the basis vectors $(|\mathbf{k}, A\rangle, |\mathbf{k}, B\rangle)^T$ spanning the Hilbert space of a k -mode, the two-level Hamiltonian is

$$\mathcal{H}_{\mathbf{k}}(\{\lambda\}) = d_{0,\mathbf{k}}\mathbb{I}_2 + \mathbf{d}_{\mathbf{k}}(\{\lambda\}) \cdot \boldsymbol{\sigma}, \quad (3.1)$$

where A and B denote the two pseudospins (which could be sublattices for bipartite systems or particle-hole pairs for superconducting systems) and the σ s are the usual Pauli matrices. The Hamiltonian in Eq. (3.1) has two eigenvalues given by $\varepsilon_{\pm,\mathbf{k}} = d_{0,\mathbf{k}} \pm |\mathbf{d}_{\mathbf{k}}|$ and the corresponding eigenvectors are denoted by $|e_{\mathbf{k}}\rangle$ and $|g_{\mathbf{k}}\rangle$ respectively. We start with a finite temperature mixed density matrix corresponding to the initial Hamiltonian $\mathcal{H}_i = \mathcal{H}(\{\lambda_i\})$ given by

$$\rho(t=0) = \otimes \prod_{\mathbf{k}} \rho_{i,\mathbf{k}} = \otimes \prod_{\mathbf{k}} [W_{-,\mathbf{k}}|g_{i,\mathbf{k}}\rangle\langle g_{i,\mathbf{k}}| + W_{+,\mathbf{k}}|e_{i,\mathbf{k}}\rangle\langle e_{i,\mathbf{k}}|], \quad (3.2)$$

where

$$\begin{aligned} \rho_{i,\mathbf{k}} &= W_{-,\mathbf{k}}|g_{i,\mathbf{k}}\rangle\langle g_{i,\mathbf{k}}| + W_{+,\mathbf{k}}|e_{i,\mathbf{k}}\rangle\langle e_{i,\mathbf{k}}| \\ &= \frac{1}{2} \left[\mathbb{I}_2 + (W_{+,\mathbf{k}} - W_{-,\mathbf{k}}) \frac{\mathbf{d}_{i,\mathbf{k}} \cdot \boldsymbol{\sigma}}{d_{i,\mathbf{k}}} \right], \end{aligned} \quad (3.3)$$

with $W_{\pm,\mathbf{k}}$ being the Boltzmann weights given by

$$W_{\pm,\mathbf{k}} = e^{-\beta\varepsilon_{\pm,i,\mathbf{k}}} / (e^{-\beta\varepsilon_{-i,\mathbf{k}}} + e^{-\beta\varepsilon_{+i,\mathbf{k}}}). \quad (3.4)$$

Note, that $\text{Tr}[\rho_{i,\mathbf{k}}] = 1$ for every \mathbf{k} so that the system is half-filled.

Evolution of ρ_i with \mathcal{H}_f , $\rho(t) = e^{-i\mathcal{H}_f t} \rho_i e^{i\mathcal{H}_f t}$ after the quench eventually leads to the diagonal ensemble represented by a density matrix of the form $\rho_\infty = \otimes \prod_{\mathbf{k}} \rho_{\mathbf{k},\infty}$, where

$$\rho_{\infty,\mathbf{k}} = \frac{1}{2} \left[\mathbb{I}_2 + (W_{+,\mathbf{k}} - W_{-,\mathbf{k}}) \frac{\mathbf{d}_{i,\mathbf{k}} \cdot \mathbf{d}_{f,\mathbf{k}}}{d_{i,\mathbf{k}} d_{f,\mathbf{k}}^2} \mathbf{d}_{f,\mathbf{k}} \cdot \boldsymbol{\sigma} \right]. \quad (3.5)$$

The expectation value of any local operator \mathcal{O} in the limit of $t \rightarrow \infty$ can be calculated as

$$\langle \mathcal{O} \rangle = \frac{1}{2\pi} \int d\mathbf{k} \text{Tr}[\rho_{\infty,\mathbf{k}} \hat{\mathcal{O}}_{\mathbf{k}}], \quad (3.6)$$

where the decomposition into the \mathbf{k} -modes is possible because we consider translation-invariant operators.

$\langle \mathcal{O} \rangle$ is then studied as a function of λ_f , the final parameter to which the system is quenched, a non-analyticity is observed when $\lambda_f = \lambda_c$. A natural choice of local observable is the energy difference between the initial and final states, measured with respect to a Hamiltonian corresponding to *any* point λ_m in parameter space. Formally, this energy difference is defined as $\Delta E = \text{Tr}[\mathcal{H}_m \rho_\infty] - \text{Tr}[\mathcal{H}_m \rho_0]$. Note that we keep λ_m fixed as we vary λ_f . In fact, any local observable which does not commute with \mathcal{H}_f can capture the non-analyticity. The non-analytic signatures persist for any finite temperature initial state (though attenuated as the temperature is increased). Note that for conventional quantum phase transitions, the energy of the ground state of $\mathcal{H}(\lambda)$ measured with respect to $\mathcal{H}(\lambda)$ itself shows a non-analytic behavior at $\lambda = \lambda_c$.

3.3 Signatures in one dimension

The non-analytic signatures for topological criticality are first discussed for the case of one-dimensional models, namely, the SSH model and the Kitaev p-wave superconducting chain.

3.3.1 Results for the SSH model

As discussed in Chapter 2, the SSH model is described by the tight-binding Hamiltonian $\mathcal{H}_{\text{SSH}} = -\sum_l [\lambda_1 \hat{c}_{l,A}^\dagger \hat{c}_{l,B} + \lambda_2 \hat{c}_{l,B}^\dagger \hat{c}_{l+1,A} + \text{h.c.}]$. For simplicity of notation, we consider $\lambda_1 = 1$ and $\lambda_2 = \lambda$. With this notation, the reciprocal space Hamiltonian (3.1) can be expressed with the components of the $\mathbf{d}_{\mathbf{k}}$ $d_{\mathbf{k}}^x = 1 + \lambda \cos k$; $d_{\mathbf{k}}^y = \lambda \sin k$; $d_{\mathbf{k}}^z = 0 = d_{\mathbf{k},0}$. As discussed in Chapter 2, the model has two critical points, at $\lambda = \pm 1$, with gapless modes at $k = \pi$ and $k = 0$, respectively.

To demonstrate the results explicitly, we choose the observable to be the expectation value of the Hamiltonian corresponding to the parameter λ_m . Using the

expressions for the initial and final density matrices from Eqs. (3.3) and (3.5). The expectation value $\mathcal{H}(\lambda_m)$ can be expressed as

$$\begin{aligned} E_0 &= \frac{1}{2\pi} \int d\mathbf{k} \operatorname{Tr}[\rho_{0,\mathbf{k}} \mathcal{H}_{m,\mathbf{k}}] \\ &= \frac{1}{2\pi} \int d\mathbf{k} \left[d_{0,m,\mathbf{k}} + (W_{+,\mathbf{k}} - W_{-,\mathbf{k}}) \frac{\mathbf{d}_{i,\mathbf{k}} \cdot \mathbf{d}_{m,\mathbf{k}}}{d_{i,\mathbf{k}}} \right], \end{aligned} \quad (3.7)$$

$$\begin{aligned} E_\infty &= \frac{1}{2\pi} \int d\mathbf{k} \operatorname{Tr}[\rho_{\infty,\mathbf{k}} \mathcal{H}_{m,\mathbf{k}}] \\ &= \frac{1}{2\pi} \int d\mathbf{k} \left[d_{0,m,\mathbf{k}} + (W_{+,\mathbf{k}} - W_{-,\mathbf{k}}) \frac{\mathbf{d}_{i,\mathbf{k}} \cdot \mathbf{d}_{f,\mathbf{k}}}{d_{i,\mathbf{k}}} \frac{\mathbf{d}_{f,\mathbf{k}} \cdot \mathbf{d}_{m,\mathbf{k}}}{d_{f,\mathbf{k}}} \right]. \end{aligned} \quad (3.8)$$

For the SSH model, ΔE turns out to be

$$\Delta E = \frac{1}{2\pi} \int_0^{2\pi} dk \frac{(W_{+,\mathbf{k}} - W_{-,\mathbf{k}})(\lambda_f - \lambda_i)(\lambda_f - \lambda_m) \sin^2 k}{(\lambda_f^2 + 2\lambda_f \cos k + 1) \sqrt{\lambda_i^2 + 2\lambda_i \cos k + 1}}. \quad (3.9)$$

For simplicity of presentation, we take $\lambda_i = 0 = \lambda_m$ (corresponding to the orange curve in Figure 3.1). With these parameters, Eq. (3.9) turns out to be of the form

$$\Delta E = \frac{1}{4} \left[(\lambda_f^2 + 1) - (\lambda_f + 1)^2 \left| \frac{\lambda_f - 1}{\lambda_f + 1} \right| \right] = \begin{cases} \lambda_f^2/2; & |\lambda_f| < 1 \\ 1/2; & |\lambda_f| > 1 \end{cases}, \quad (3.10)$$

which clearly shows that the first derivative of ΔE with respect to λ_f is discontinuous at the critical points $\lambda_c = \pm 1$, and hence the non-analyticity.

For other values of λ_i and λ_m , a closed form expression is difficult to write. However a numerical evaluation of the integral in Eq. (3.9) reveals the non-analyticities in ΔE at the critical point(s) as shown in Figure 3.1(a)-(b) for different values of the parameters and temperatures.

The non-analyticity in ΔE as function of λ_f appears as a kink at the critical point: the second derivative of ΔE with respect to λ_f diverges at the critical point, as can be seen by expanding the second derivative of ΔE with respect to λ_f around the gapless mode at the critical point. By taking the critical point at $\lambda_f = 1$, and expanding in powers of $\kappa = k - \pi$ one finds that

$$\left. \frac{\partial^2(\Delta E(\kappa))}{\partial \lambda_f^2} \right|_{\lambda_f=1} = \frac{C_{-2}}{\kappa^2} + C_0 + C_2 \kappa^2 + \dots \quad (3.11)$$

Hence, while the quench protocol populates higher-excited eigenmodes of $\mathcal{H}_{\text{SSH}}(\lambda_f)$, the dominant contribution to the non-analyticity of ΔE comes from the gapless mode k_c .

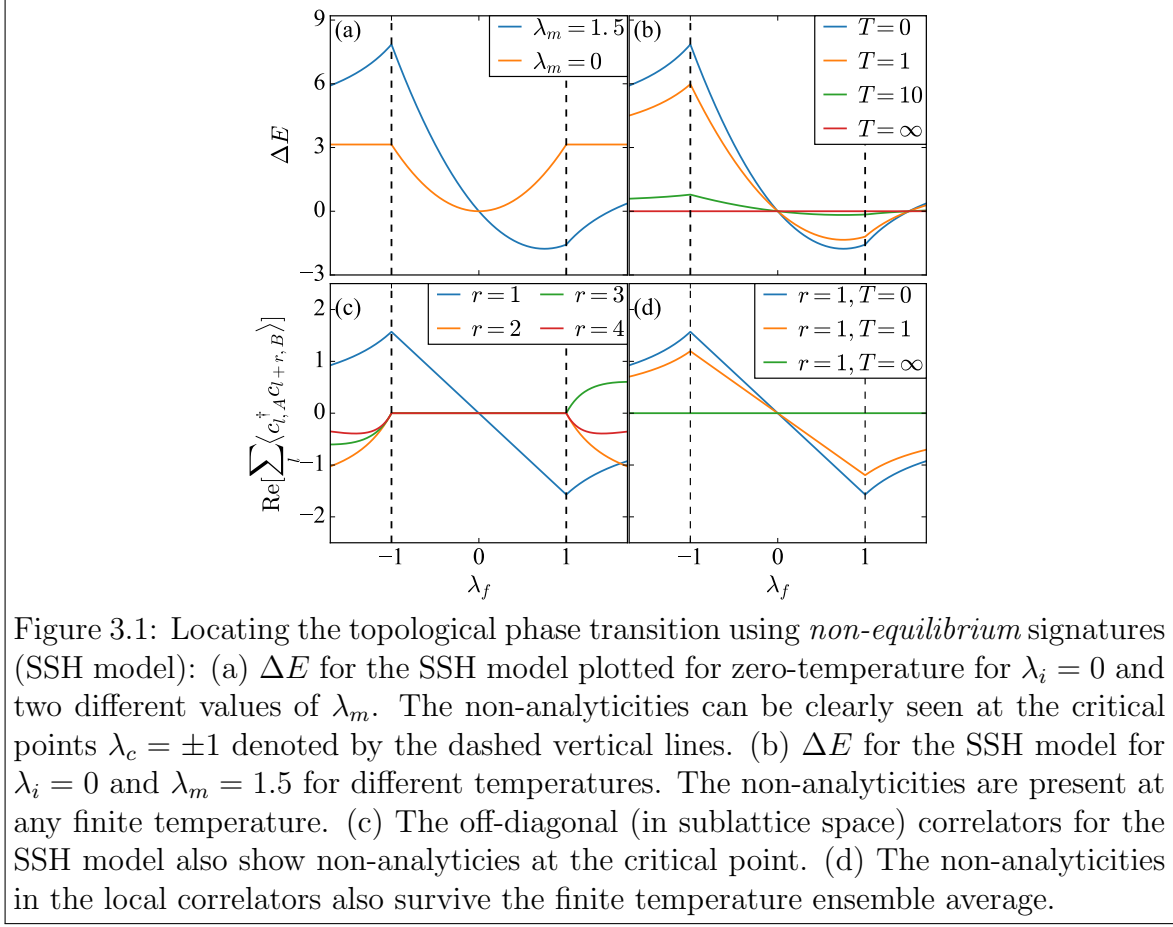


Figure 3.1: Locating the topological phase transition using *non-equilibrium* signatures (SSH model): (a) ΔE for the SSH model plotted for zero-temperature for $\lambda_i = 0$ and two different values of λ_m . The non-analyticities can be clearly seen at the critical points $\lambda_c = \pm 1$ denoted by the dashed vertical lines. (b) ΔE for the SSH model for $\lambda_i = 0$ and $\lambda_m = 1.5$ for different temperatures. The non-analyticities are present at any finite temperature. (c) The off-diagonal (in sublattice space) correlators for the SSH model also show non-analyticities at the critical point. (d) The non-analyticities in the local correlators also survive the finite temperature ensemble average.

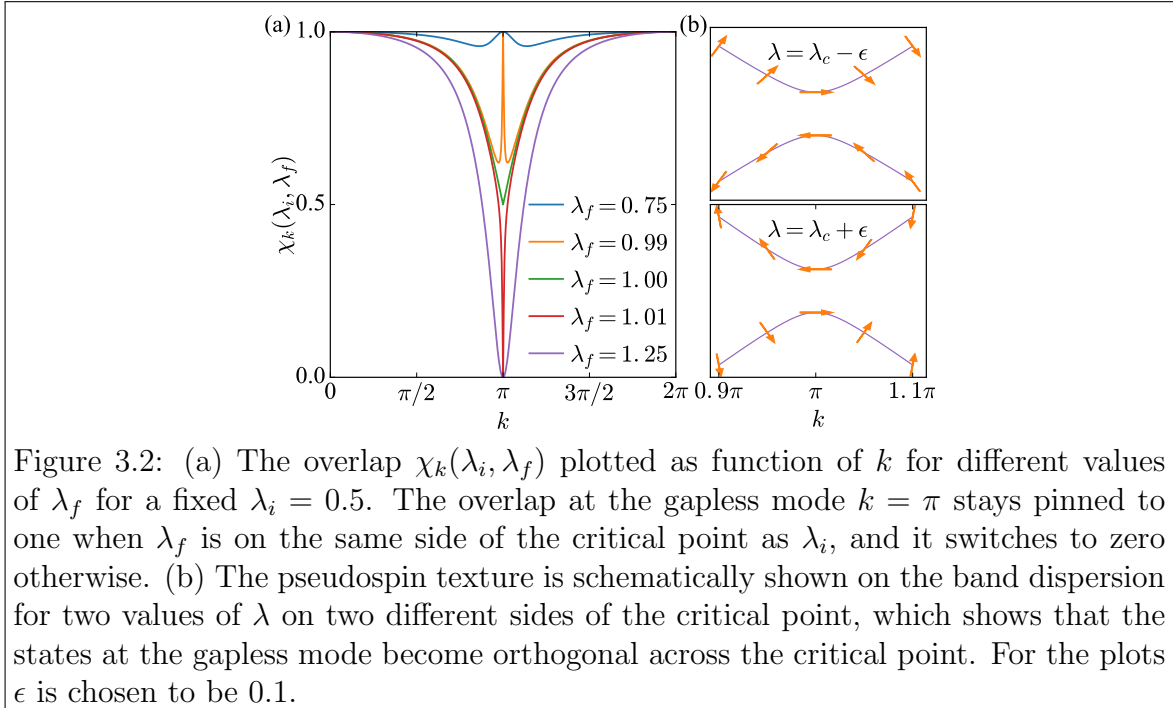


Figure 3.2: (a) The overlap $\chi_k(\lambda_i, \lambda_f)$ plotted as function of k for different values of λ_f for a fixed $\lambda_i = 0.5$. The overlap at the gapless mode $k = \pi$ stays pinned to one when λ_f is on the same side of the critical point as λ_i , and it switches to zero otherwise. (b) The pseudospin texture is schematically shown on the band dispersion for two values of λ on two different sides of the critical point, which shows that the states at the gapless mode become orthogonal across the critical point. For the plots ϵ is chosen to be 0.1.

The mechanism of the non-analyticity can be understood by looking at the mode-by-mode overlap of the initial state with the eigenstates of $\mathcal{H}_{\text{SSH}}(\lambda_f)$ across the critical point. For simplicity of illustration, start with the ground state of $\mathcal{H}_{\text{SSH}}(\lambda_i)$ ($|\psi(t=0)\rangle = \otimes \prod_k |g_k(\lambda_i)\rangle$). The overlap is defined as $\chi_k(\lambda_i, \lambda_f) = |\langle g_k(\lambda_i) | g_k(\lambda_f) \rangle|^2$ and plotted as a function of k for different values of λ_f in Figure 3.2(a). As long as λ_f stays on one side of the critical point, the overlap at the gapless mode ($k_c = \pi$) stays pinned to one, even when it is arbitrarily close to the critical point. However as soon as the critical point is crossed, the overlap jumps to zero discontinuously, where it stays pinned.

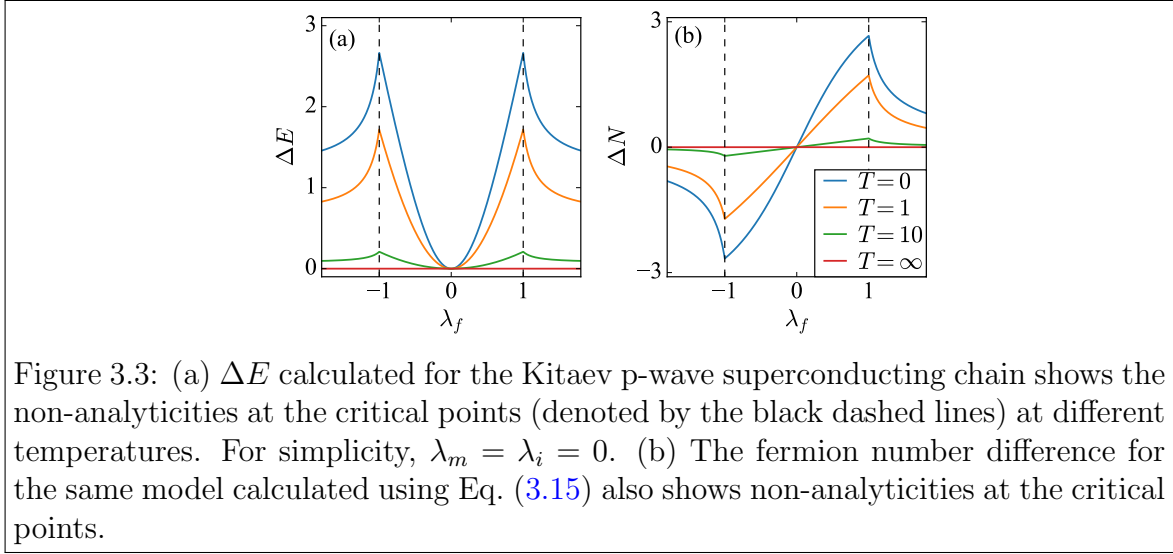
This discontinuous jump can be understood via the pseudospin textures (in sublattice space) at the gapless mode across the critical point. Since the SSH model is a bipartite system, one can simply compute the pseudospin textures by taking the expectation values of the Pauli matrices with respect to the eigenstates of the Hamiltonian. These textures shown in Figure 3.2(b) at the gapless mode ($k = \pi$) for the parameter value $\lambda = 1 + \epsilon$ take the form

$$\langle g_\pi(1 + \epsilon) | \boldsymbol{\sigma} | g_\pi(1 + \epsilon) \rangle = \{\text{sgn}(\epsilon), 0, 0\}. \quad (3.12)$$

The sign function ensures that across the critical point, the states at the gapless mode are orthogonal to each other, which manifests itself in the overlap switching from one to zero suddenly as the parameter is varied across the critical point.

The above arguments show that the non-analyticity in the observables at the critical point comes from the fact that the gapless mode is occupied and the nature of the state at the mode changes in a discontinuous way across the transition. This corroborates the earlier claim that it is not necessary to start from the ground state of \mathcal{H}_i , which also explains why the non-analyticities survive the finite temperature ensemble average.

In order to show that the non-analyticity hiding in the final density matrix can be captured by almost any local observable local correlation functions following the quench are also calculated. Note that the reciprocal space Hamiltonian of the SSH model is always restricted to the x - y plane in sublattice space and hence any correlator which is diagonal in sublattice space ($\propto \sigma^z$) has zero expectation value. Hence off-diagonal correlations defined as $\hat{G}_r = \sum_l \langle c_{l,A}^\dagger c_{l+r,B} \rangle$ are calculated. As expected these correlations also show non-analyticities of the same form as ΔE and they also survive the finite temperature ensemble averaging as can be seen in Figure 3.1(c)-(d).



3.3.2 Results for Kitaev p-wave superconducting chain

For completeness, the non-analytic signatures of topological quantum criticality are also studied in the Kitaev p-wave superconducting chain. The Hamiltonian of the model is given by

$$\mathcal{H}_{\text{p-SC}} = - \sum_i [c_i^\dagger c_{i+1} + \text{h.c.}] + \lambda \sum_i c_i^\dagger c_i + \sum_i [\Delta_{\text{SC}} c_i^\dagger c_{i+1}^\dagger + \text{h.c.}], \quad (3.13)$$

where λ , the chemical potential is our quench parameter and Δ_{SC} is the superconducting order parameter. The coefficients of the Pauli matrices in reciprocal space Hamiltonian are

$$d_{\mathbf{k}}^x = 0 = d_{\mathbf{k},0}; \quad d_{\mathbf{k}}^y = \Delta_{\text{SC}} \sin k; \quad d_{\mathbf{k}}^z = -\cos k - \lambda, \quad (3.14)$$

where the basis now is $(|k\rangle, |-k\rangle)^T$. This model has a phase transition between a topological superconducting phase with Majorana edge modes and a normal superconducting phase at $\lambda_c = \pm$. The model being a superconducting one does not conserve fermion number which naturally suggests a local observable which is experimentally relevant, namely the difference in the number of fermions before and after the quench, $\Delta N = \text{Tr}[\hat{N}\rho_\infty] - \text{Tr}[\hat{N}\rho_0]$, where \hat{N} is the total fermion number operator. ΔN turns out to be

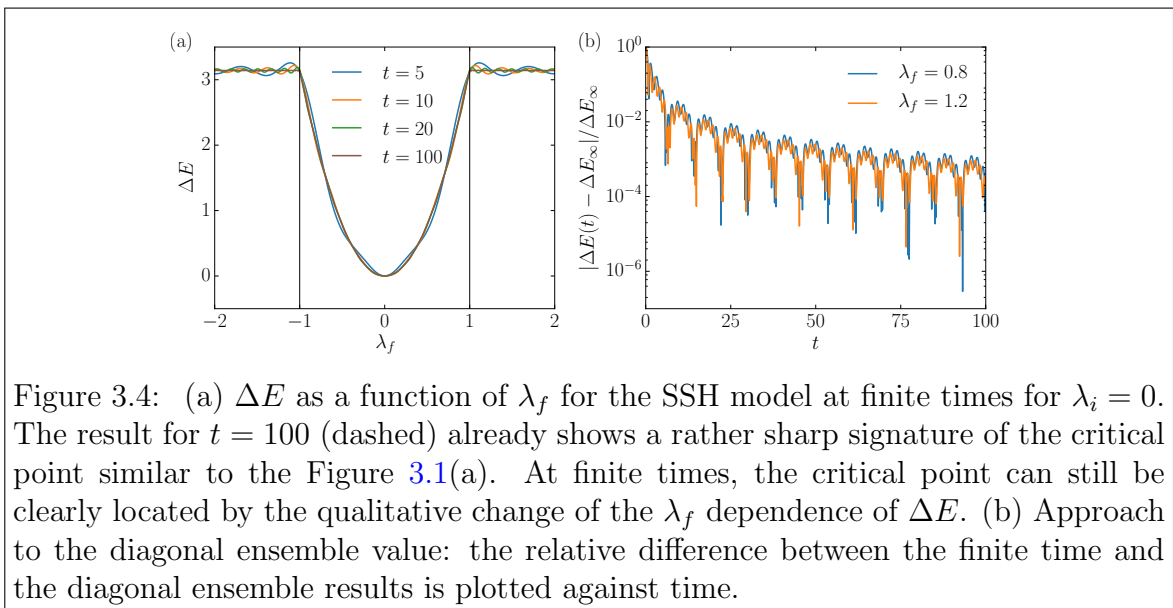
$$\Delta N = \frac{1}{2\pi} \int_0^{2\pi} dk (W_{+, \mathbf{k}} - W_{-, \mathbf{k}}) \frac{\mathbf{d}_{i, \mathbf{k}} \cdot \mathbf{d}_{f, \mathbf{k}}}{d_{i, \mathbf{k}} d_{f, \mathbf{k}}^2} d_{f, \mathbf{k}}^z, \quad (3.15)$$

where the vectors $\mathbf{d}_{\mathbf{k}}(\lambda)$ are given by Eq. (3.14). The difference in fermion number also shows a sharp kink at the critical points like the energy difference. As before these

non-analyticities are robust towards a finite temperature ensemble average. These non-analyticities can be seen in Figure 3.3.

3.3.3 Signatures at finite times

The results can be experimentally verified via quantum quench experiments similar to the one in Fläschner *et al.* (2016). The results show that the non-analyticities at the critical points appear in the limit of infinite time following the quench as the density matrix describing the state approaches the one corresponding to the diagonal ensemble. At finite times, the non-analyticities are dressed by the off-diagonal contributions. However, explicit calculations show that even at finite times accessible in experiments, the critical points can be identified even though the cusp present at infinite times is rounded off. For instance, in Figure 3.4, ΔE for the SSH model at different times t (measured in units of inverse hopping) is shown. At time scales achievable in the experiment [Fläschner *et al.* (2016)], namely $t = 10$ and $t = 20$, one can identify the critical points from the change in nature of the functions around $\lambda_f = \pm 1$. The emerging cusp is already clearly discernible at $t = 100$.



3.4 Signatures in two dimensions

The non-analytic signatures are now discussed for the case of two spatial dimensions. It is interesting to note that quench protocol succeeds in detecting topological quantum phase transitions via local bulk observables, whereas it is known that the

topological properties of a state quantified via the Chern number do not change following a quantum quench although indications of the topological quantum criticality can be found by studying the topological edge responses [D'Alessio and Rigol (2015); Caio *et al.* (2015)]. The model of choice is Haldane's honeycomb model introduced in Chapter 2, the Hamiltonian for which in real and momentum space is, respectively, mentioned in Eqs. (2.6) and (2.7). The model has critical lines in parameter space given by the relations $M = \pm 3\sqrt{3}t_2 \sin \phi$ as shown in Figure 2.2.

Apart from the energy difference as before, the other local observable calculated is the difference between the number of fermions on one sublattice before and after the quench, $\Delta N_A = \text{Tr}[\rho_\infty \hat{N}_A] - \text{Tr}[\rho_0 \hat{N}_A]$, where $\hat{N}_A = \sum_l c_{l,A}^\dagger c_{l,A}$. Note that it differs from the staggered occupation number operator $\hat{N}_A - \hat{N}_B$ by a constant as the total number of fermions is a constant of motion. In the parameter space of the model, for simplicity, ϕ is kept fixed and M is quenched. However, the non-analyticities, if present, would show up across any quench path across the critical line.

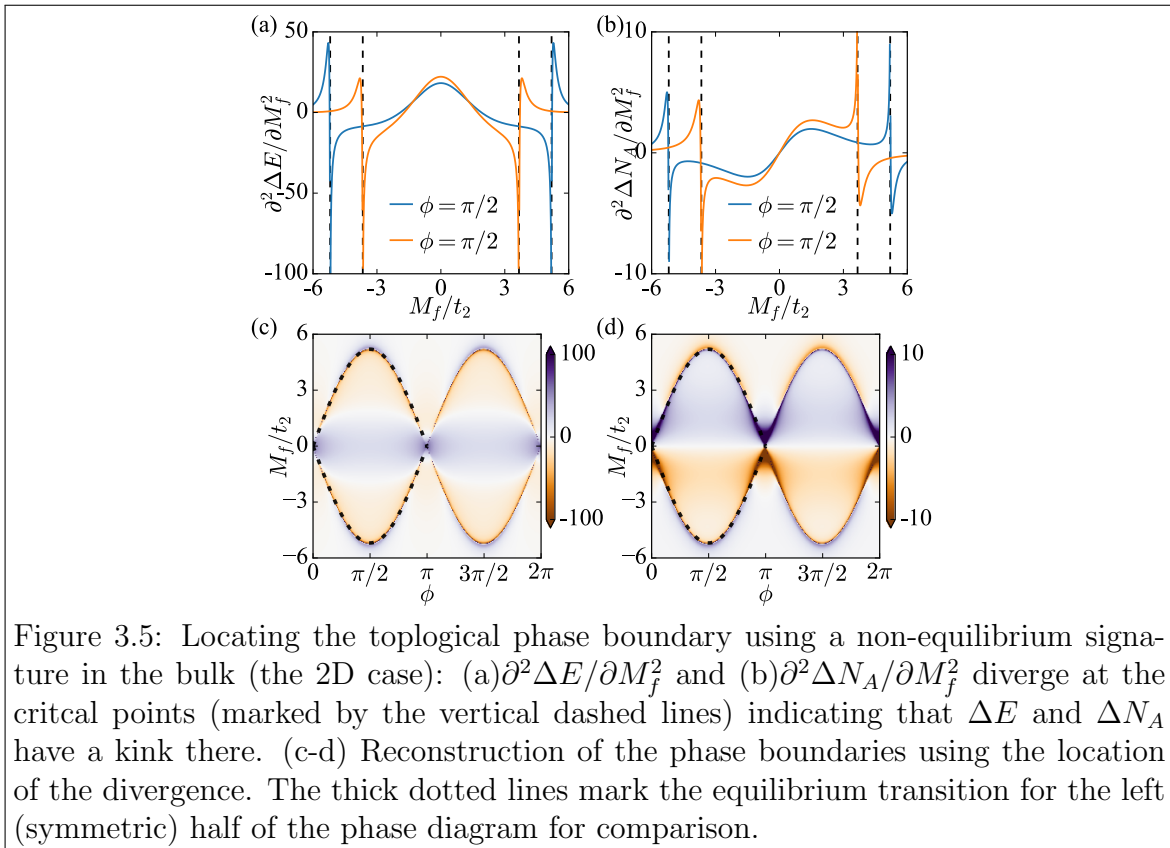


Figure 3.5: Locating the topological phase boundary using a non-equilibrium signature in the bulk (the 2D case): (a) $\partial^2 \Delta E / \partial M_f^2$ and (b) $\partial^2 \Delta N_A / \partial M_f^2$ diverge at the critical points (marked by the vertical dashed lines) indicating that ΔE and ΔN_A have a kink there. (c-d) Reconstruction of the phase boundaries using the location of the divergence. The thick dotted lines mark the equilibrium transition for the left (symmetric) half of the phase diagram for comparison.

The presence or absence of non-analyticities in the expectation values of observables can be studied by looking at the derivatives of these quantities with respect to the final value of the quench parameter. As in Eq. (3.11) the second derivative of

the expectation values of the observables is expanded around the gapless mode at the critical parameter values. Expressing $k_1 = k_{c,1} + \kappa \cos \theta_{\mathbf{k}}$ and $k_2 = k_{c,2} + \kappa \sin \theta_{\mathbf{k}}$, the expansion can be done in powers of κ

$$\left. \frac{\partial^2(\Delta E(\kappa))}{\partial M_f^2} \right|_{M_f=3\sqrt{3}t_2 \sin \phi} = \frac{C_{-2}}{\kappa^2} + \frac{C_{-1}}{\kappa} + C_0 + C_2 \kappa^2 + \dots \quad (3.16)$$

The nature of the non-analyticity (kink) in the observables depends on the divergence of its second derivative with λ_f calculated for the gapless mode at $\lambda_f = \lambda_c$, and the integral measure in Eq. (3.6). It is apparent (comparing Eqs.(3.11) and (3.16)) that the non-analyticity is weaker in 2D compared to 1D.

3.5 Absence of signatures for non-topological gap closings

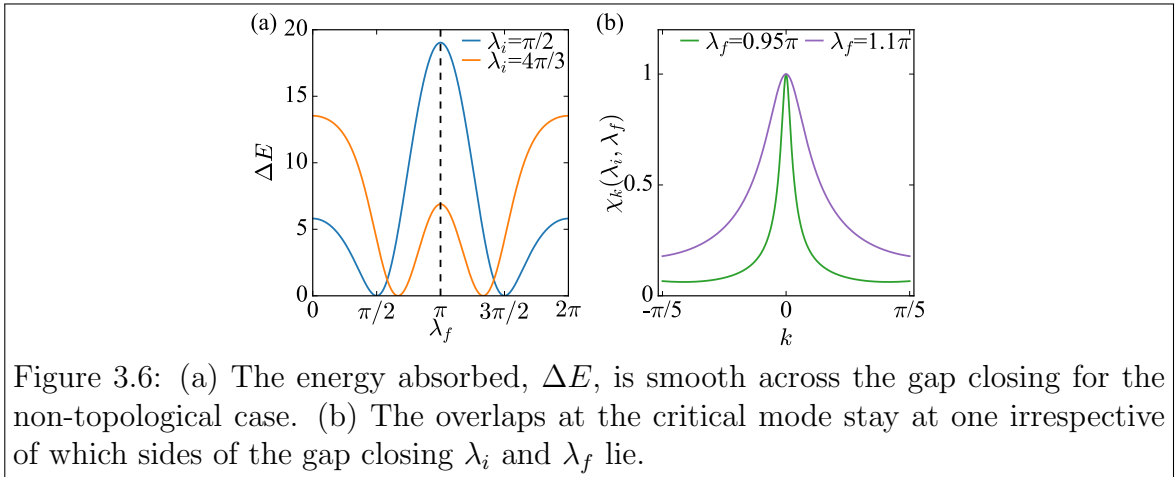


Figure 3.6: (a) The energy absorbed, ΔE , is smooth across the gap closing for the non-topological case. (b) The overlaps at the critical mode stay at one irrespective of which sides of the gap closing λ_i and λ_f lie.

In this section, a situation is demonstrated where there exists a non-topological linear band touching, which does not correspond to any real phase transition and hence does not give rise to any non-analytic signature. Such non-topological gap closings can be studied in a particular two-leg ladder with complex hoppings. Its reciprocal space Hamiltonian takes the form

$$\mathcal{H}_{NT}(k) = -\sin k \sigma^x + (1 - \cos k) \sigma^y + [1 + \cos k + 2 \cos \lambda] \sigma^z. \quad (3.17)$$

The model has a gap closing at $\lambda_c = \pi$ at $k_c = 0$. However, the sign of the effective mass at the gapless mode $2(1 + \cos \lambda)$ remains non-negative so that the gap closing does not change the topological properties of the band. Consequently, the pseudospin texture in the BZ also does not change suddenly across the gap-closing and in fact at the gapless mode always stays pinned at $\langle \sigma \rangle = \{0, 0, 1\}$ for the lower band. This

results in the overlap $\chi_k(\lambda_i, \lambda_f)$ also being pinned to one (see Figure 3.6) and hence there is no sudden change. This manifests itself in the smooth behavior of ΔE across the gap closing as shown in Figure 3.6.

3.6 Summary

In this chapter, it was shown that non-analytic signatures of topological quantum phase transition in non-interacting fermionic systems are manifested in local observables measured on excited states with finite energy densities obtained via a quantum quench. The non-analytic signatures originate from the non-analytic change of the effective pseudospin texture at the gapless mode across the critical point, hence the crucial ingredient for observation of the signatures is an occupation gradient across the energy of the gapless mode. It was also found that a gap closing alone is not enough to show the signatures, rather there has to be a phase transition (which is a topological one for non-interacting fermions) for the signatures to be present.

The findings can be experimentally realised in quantum quench experiments such as in Fläschner *et al.* (2016) designed to study quantum quenches in translation-invariant two-level systems, just like the ones treated in this chapter. The two-component spinor corresponding to each k -mode forms a unit vector parameterised by two angles on the Bloch sphere, which is measured in the experiment as a function of time. Hence, the full information of the quantum state can be extracted and expectation values of any local observable consequently reconstructed. Although the non-analyticities reported in this chapter are strictly observed only after infinite evolution times, sufficiently sharp signatures can be expected within the experimentally accessible time scales of coherent evolution.

Even though topological quantum phase transitions in non-interacting fermionic models often correspond to conventional phase transitions related via non-local transformations, the protocol described in this chapter does not depend on the representation in which the transition is topological. As these signatures are not present if the gap closing in the non-interacting fermionic model does not lead to a change in the topological nature of the underlying energy bands participating in the gap closing, spin models corresponding to such free fermion models have their Hamiltonian parameters restricted in such a way that they are confined to either the ordered or the disordered regimes in their phase diagram. Hence, one could also conjecture that any order-disorder phase transition, if it possesses a bonafide single-particle representation, will turn out to be a topological one in the non-interacting picture. The

non-analyticities in the local observables can be traced back to those in the (extensive number of) Lagrange multipliers characterising the generalised Gibbs ensemble describing the steady state of the integrable systems. Whether the few Lagrange multipliers (for instance, the effective temperature) that describe the Gibbs ensemble for interacting systems have a non-analyticity as well, with a concomitant signature in local observables, is an interesting question for future studies.

Chapter 4

Wavepacket dynamics of Chern band lattices in a trap

The experimental realization of lattices hosting non-trivial Berry curvature profiles using ultracold atoms trapped in optical lattices [Aidelsburger *et al.* (2013); Miyake *et al.* (2013); Jotzu *et al.* (2014)] has led to an increased interest in characterizing their topological nature from non-equilibrium responses [Killi and Paramakanti (2012); Killi *et al.* (2012); Dauphin and Goldman (2013); Hauke *et al.* (2014); Goldman *et al.* (2013); Aidelsburger *et al.* (2015); Sacramento (2014); Price and Cooper (2012); Grushin *et al.* (2016a)]. For ultracold atoms (especially bosons) and for photonic systems, a dynamical situation where the atoms/photons form a spatially localized and evolving wavepacket is more natural than a static situation in which a band is exactly filled. A particularly important theme is the response of a localized wavepacket to an applied force (potential gradient) [Price and Cooper (2012); Dauphin and Goldman (2013); Jotzu *et al.* (2014); Aidelsburger *et al.* (2015); Duca *et al.* (2015)]. One expects Bloch oscillations in the direction of the applied force. In addition, there is also motion perpendicular to the direction of the force, with contributions due to the topological Berry curvature and due to the band dispersion.

A natural framework to describe the motion of wavepackets is to use semiclassical equations of motion, discussed in Chapter 2.

Semiclassical approaches typically rely on the approximation of assigning a sharply defined position and momentum simultaneously to a quantum state. Based on this assumption one can solve the set of coupled differential equations for position and momenta and hence obtain sharply defined trajectories of the particle in both real and momentum space. However, this assumption is *a priori* not valid in realistic situations where the wavepackets have a finite spread in both real and momentum space, a scenario expected in typical ultracold bosonic and photonic experiments.

The focus of this chapter is the influence of the size and initial momentum of a wavepacket placed off-center in a harmonic trap in Haldane’s honeycomb model, and the ability of the semiclassical approach to take such effects into account. The transverse motion of the wavepacket is quantified using the angular velocity $\dot{\theta}$ with respect to the center of the trap.

It is found that the standard point-particle semiclassical approach captures some qualitative features of the dynamics, but is generally insufficient to quantitatively describe the actual real-time dynamics. Therefore, the semiclassical description is reformulated to take into account the finite spread of the wavepacket in momentum space. The exact evolution of $\dot{\theta}$ is compared in detail to predictions from the extended semiclassics and from the standard point-particle semiclassics. In momentum space, the wavepacket moves at a constant rate in the direction of the force, leading to Bloch oscillations. As it crosses different regions of the Brillouin zone, the local Berry curvature and band curvature determine $\dot{\theta}(t)$. For spatially localized wavepackets, the extent in momentum space is finite. The “extended semiclassics” procedure incorporates the variations of band dispersion and Berry curvature in this extended region of momentum space. It is found that, as long as the physics is dominated by one band, this procedure reproduces the full dynamics well. This shows that the basic idea of semiclassics (simultaneously assigning both position and momentum to a quantum particle) can incorporate aspects of the full quantum dynamics to an extent beyond what is known from the usual point-particle treatment.

One might intuitively expect that semiclassical descriptions should work better for spatially large wavepackets, since these correspond to smaller regions in momentum space. This is generally true, but the semiclassical framework still describes the dynamics of rather small wavepackets, especially if momentum-space extent is included. In addition, by considering a tight trap, an example of possible experimental relevance is shown where larger real-space sizes can render the semiclassical description less inaccurate, due to an inhomogeneity of the force within the spatial support region of the wavepacket.

The effect of initializing the wavepacket with a finite momentum is also demonstrated. In addition to zero momentum (Γ point) the wavepacket is initialized at one of the \mathbf{K} points and one of the \mathbf{M} points of the Brillouin zone. Imparting momenta to a gaussian wavepacket using an $e^{i\mathbf{k}\cdot\mathbf{r}}$ -like factor can cause the wavefunction to have significant occupancy in the upper band, including extreme cases where it is almost completely transferred to the upper band. As long as one of the bands dominates, the semiclassical description works well when using the properties (band dispersion and

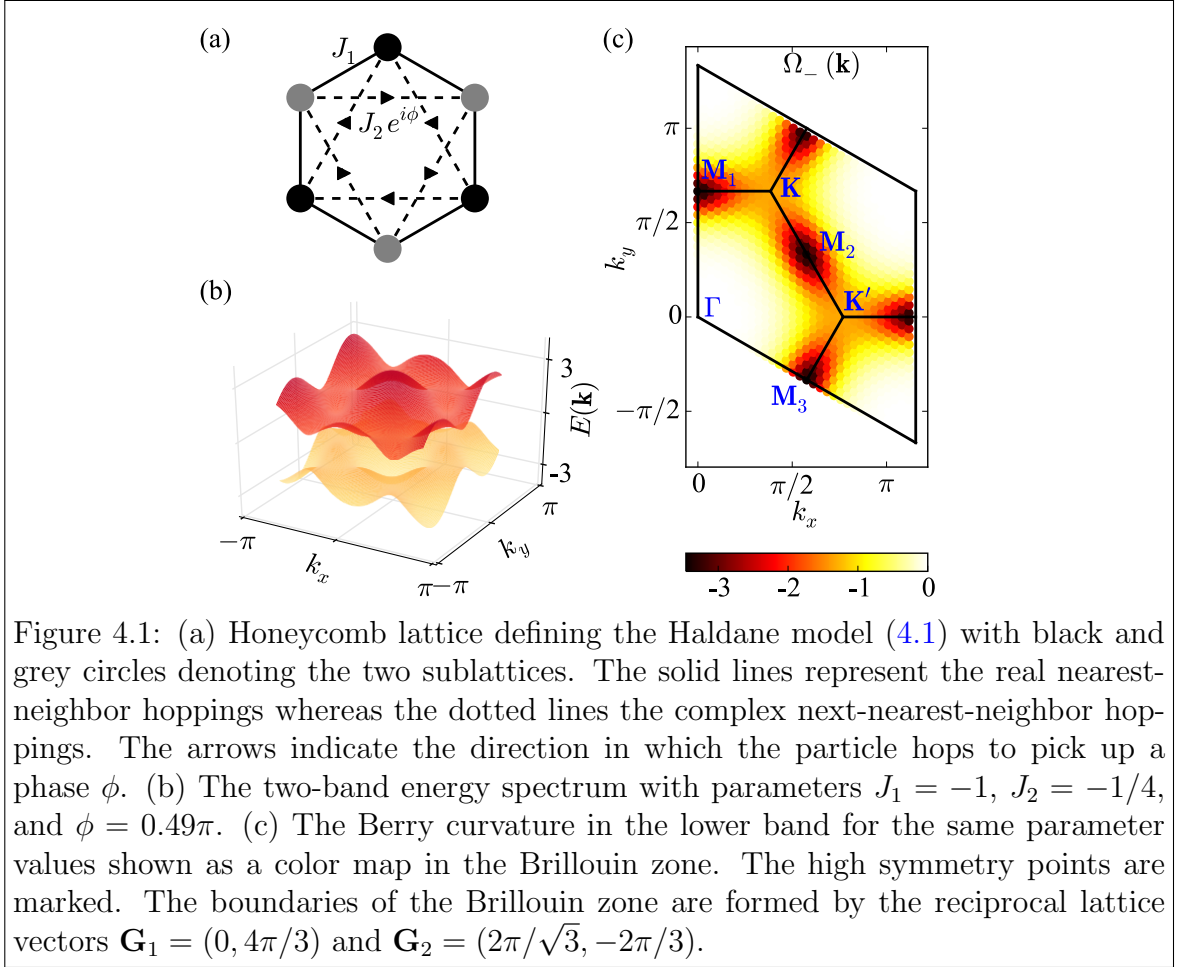


Figure 4.1: (a) Honeycomb lattice defining the Haldane model (4.1) with black and grey circles denoting the two sublattices. The solid lines represent the real nearest-neighbor hoppings whereas the dotted lines the complex next-nearest-neighbor hoppings. The arrows indicate the direction in which the particle hops to pick up a phase ϕ . (b) The two-band energy spectrum with parameters $J_1 = -1$, $J_2 = -1/4$, and $\phi = 0.49\pi$. (c) The Berry curvature in the lower band for the same parameter values shown as a color map in the Brillouin zone. The high symmetry points are marked. The boundaries of the Brillouin zone are formed by the reciprocal lattice vectors $\mathbf{G}_1 = (0, 4\pi/3)$ and $\mathbf{G}_2 = (2\pi/\sqrt{3}, -2\pi/3)$.

Berry curvature) of the band where the state has most of its weight. The single-band semiclassical procedure is naturally insufficient when multiple bands are significantly occupied: Features like interference oscillations are not captured by an incoherent averaging of contributions from different bands.

4.1 Simulations of wavepacket dynamics on the Haldane model

4.1.1 Model Hamiltonian

The model of choice for studying a system with non-trivial Berry curvature is Haldane's honeycomb model [Haldane (1988)] (described in Chapter 2) governed by the Hamiltonian

$$\mathcal{H}_{\text{HM}} = J_1 \sum_{\langle i,j \rangle} \hat{c}_i^\dagger \hat{c}_j + J_2 \sum_{\langle\langle i,j \rangle\rangle} e^{i\phi_{ij}} \hat{c}_i^\dagger \hat{c}_j + \text{h.c} \quad (4.1)$$

where the $\langle i, j \rangle$ denotes the nearest neighbors, $\langle\langle i, j \rangle\rangle$ denotes the next nearest neighbors and \hat{c}_j^\dagger (\hat{c}_j) is the creation (annihilation) operator at site i . Since the dynamics of a single particle is considered, \hat{c}_j^\dagger , \hat{c}_j may be thought of as either fermionic or bosonic operators.

The energy spectrum is gapped if $\phi \neq n\pi$ and is particle-hole symmetric for $\phi = \pi/2$. Throughout this chapter, the parameters used are $J_1 = -1$, $J_2 = -1/4$, and $\phi = 0.49\pi$, for which the energy spectrum is depicted in Fig. 4.1(b). The parameters are chosen so that the two energy bands are quite similar and none of them is excessively flat (since band flatness can introduce additional peculiarities in the dynamics), and so as to avoid exact particle-hole symmetry, since we are interested in generic rather than fine-tuned effects. For these parameters the bands have a finite Chern number; -1 for the lower band and $+1$ for the upper band. The distribution of the Berry curvature of the lower band in the Brillouin zone is shown in Fig. 4.1(c). The upper band has approximately opposite Berry curvature, i.e., positive instead of negative values. Fig. 4.1(c) also shows the high-symmetry points. In addition to zero-momentum (Γ point), there are three inequivalent \mathbf{M} points and two inequivalent \mathbf{K} points. \hbar is set to unity, time is measured in units of \hbar/J_1 and energy in units of J_1 . Space and momentum are in units of lattice spacing (set to unity) and inverse lattice spacing, respectively, and geometric angles are measured in radians.

4.1.2 Construction of wavepackets

The initial wavepacket is prepared with gaussian shape. For zero initial momentum,

$$|\psi(t=0)\rangle = \frac{1}{\mathcal{N}} \sum_l c_l |l\rangle = \frac{1}{\mathcal{N}} \sum_l e^{-\frac{|\mathbf{r}_l - \mathbf{r}_c|^2}{2\sigma^2}} |l\rangle. \quad (4.2)$$

Here $|l\rangle$ denotes a single-particle state, with the particle completely localized at a site indexed by l and \mathcal{N} is a normalization factor, and $\mathbf{r}_l = (x_l, y_l)$ denotes the Euclidean position of site l . The coefficient $c_l(t)$ denotes the amplitude of the wavefunction at time t at site l , and σ is the width of the wavepacket. A finite momentum is obtained by multiplying the coefficients with a site-dependent phase factor:

$$|\psi(t=0; \mathbf{k}_0)\rangle = \sum_l c_l(0) e^{i\mathbf{k}_0 \cdot \mathbf{r}_l} |l\rangle = \frac{1}{\mathcal{N}} \sum_l \exp \left[-\frac{|\mathbf{r}_l - \mathbf{r}_c|^2}{2\sigma^2} + i\mathbf{k}_0 \cdot \mathbf{r}_l \right] |l\rangle. \quad (4.3)$$

In cold-atom experiments, a wavepacket or atomic cloud can be boosted in momentum space in this way using a ‘Bragg pulse’; this is commonly used to determine the excitation spectrum of cold atom systems using Bragg spectroscopy (see [Ernst *et al.*](#)

(2010) for a description of the experimental technique). In experimental spectroscopy, both energy and momentum are well resolved in order to obtain the energy-momentum dispersion. In this case, the wavepacket is supplied with a momentum using the factor $e^{i\mathbf{k}_0 \cdot \mathbf{r}_l}$, but no specific energy. This can be thought of as a Bragg pulse with sharp momentum resolution but poor or non-existent energy resolution. This allows to explore various occupancies of the two energy bands.

The zero-momentum wavepacket (4.2) turns out to predominantly overlap with eigenstates of \mathcal{H}_{HM} at the bottom of the spectrum, in the lower band, as long as σ is not too small. This is generally true in simple lattice models with negative hopping constants. In a complicated model like \mathcal{H}_{HM} , this is not *a priori* obvious, but is the case for the parameters we are using.

Boosting the wavepacket in momentum space as in Eq. (4.3) can result in the wavepacket having support on both the bands of \mathcal{H}_{HM} . This is exemplified in Fig. 4.2 through the overlap of the wavepacket with the eigenstates of \mathcal{H}_{HM} . We denote the overlap of the initial state, $|\psi(t=0)\rangle$ with an eigenstate of \mathcal{H}_{HM} , $|u_\alpha\rangle$ with eigenvalue E_α as $\mathcal{O}_\alpha = |\langle\psi(t=0)|u_\alpha\rangle|^2$. Fig 4.2(a) shows a plot of \mathcal{O}_α against E_α for four out of the six high-symmetry momentum points being the initial momentum of the wavepacket. It can be seen that for $\mathbf{k}_0 = \mathbf{K}$ the wavepacket has support on both bands. The wavepacket corresponding to $\mathbf{k}_0 = \mathbf{M}_1$ is also shifted higher in energy, though it overlaps primarily with the states of the lower band. On the contrary, for $\mathbf{k}_0 = \mathbf{M}_2$ the weight shifts almost entirely to the upper band. Such a drastic difference of behavior between the \mathbf{M}_1 and \mathbf{M}_2 points may seem unexpected because they are related by symmetry. However, the eigenfunction structures are of course inequivalent, so the overlap distributions after a momentum boost cannot be expected to be similar.

The weight of the wavepacket on the lower band, W_- , is quantified by taking the sum of the overlaps of the wavepacket with the eigenstates of the lower band. Mathematically,

$$W_- = \sum_{\alpha=1}^{N/2} \mathcal{O}_\alpha; \quad W_+ = 1 - W_-, \quad (4.4)$$

where W_+ is the weight on the upper band, and N is the number of sites in the lattice and hence the number of single-particle eigenstates. The color map in Fig. 4.2(b) shows the magnitude of W_- for a wavepacket with a given initial momentum in the Brillouin zone.

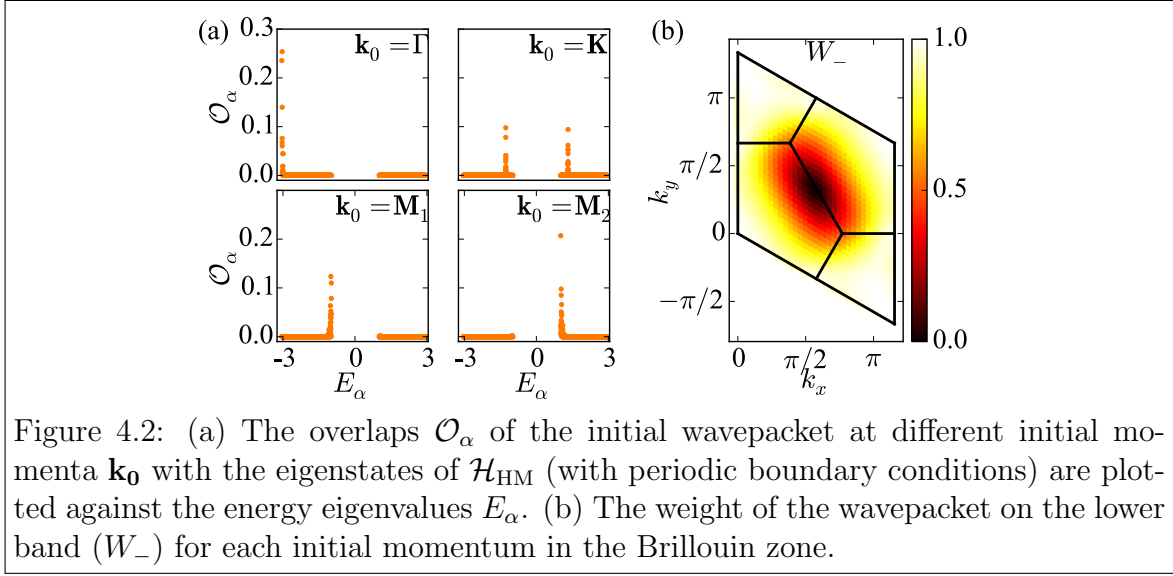


Figure 4.2: (a) The overlaps \mathcal{O}_α of the initial wavepacket at different initial momenta \mathbf{k}_0 with the eigenstates of \mathcal{H}_{HM} (with periodic boundary conditions) are plotted against the energy eigenvalues E_α . (b) The weight of the wavepacket on the lower band (W_-) for each initial momentum in the Brillouin zone.

4.1.3 Harmonic trap

The evolution in time is carried out with the Hamiltonian

$$\mathcal{H} = \mathcal{H}_{\text{HM}} + \mathcal{H}_{\text{trap}} = \mathcal{H}_{\text{HM}} + \sum_l V(l) \hat{c}_l^\dagger \hat{c}_l, \quad (4.5)$$

where

$$V(l) = \frac{V_0}{2} |\mathbf{r}_l - \mathbf{r}_0|^2, \quad (4.6)$$

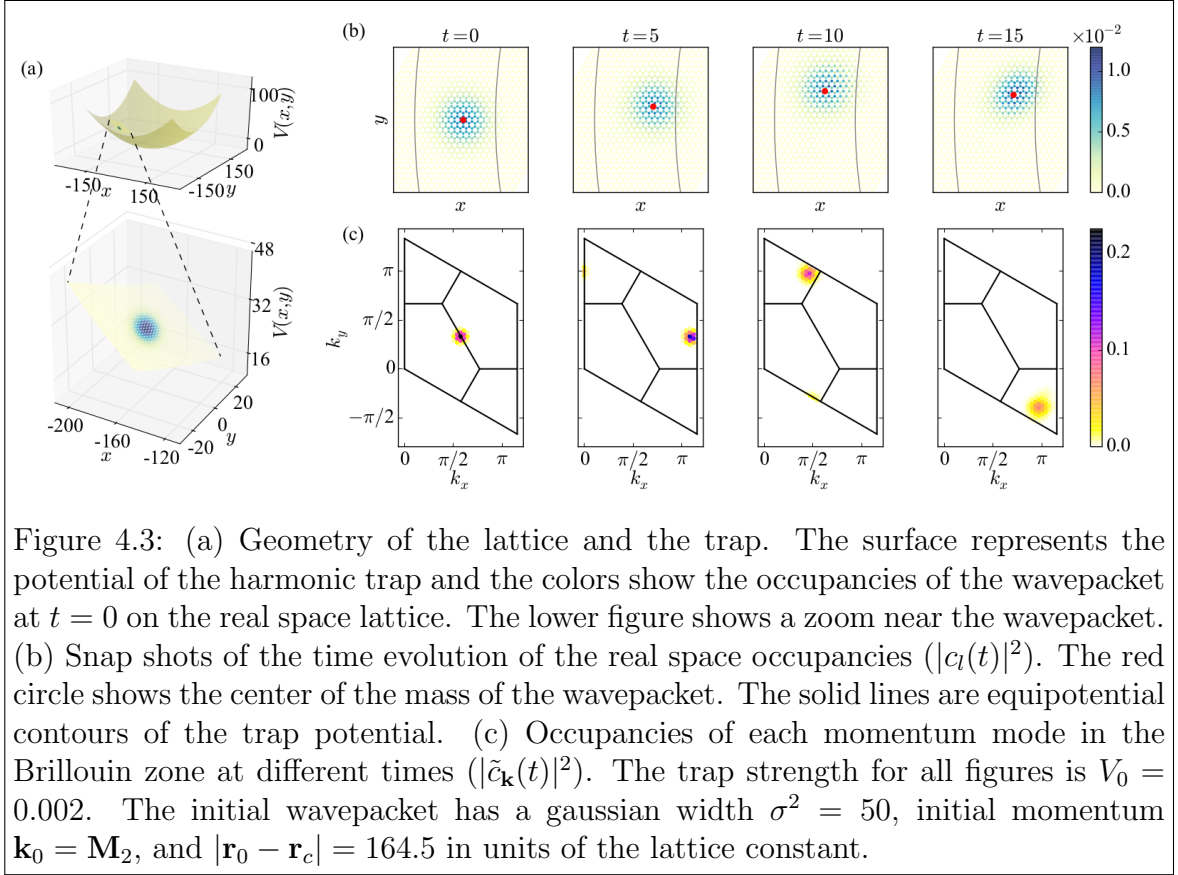
with $\mathbf{r}_0 = (x_0, y_0)$ denoting the center of the harmonic trap and V_0 controlling its strength.

The force exerted by the trap is along the inward radial direction, so that one expects Bloch oscillations in this direction. Particularly interesting is the transverse response, and hence the angular velocity of the wavepacket around the center of the trap is a natural observable to study. The angular variable θ at position $\mathbf{r} = (x, y)$ is given by $\theta = \tan^{-1} \frac{y-y_0}{x-x_0}$. Its average as a function of time is calculated using

$$\langle \theta \rangle(t) = \tan^{-1} \frac{\langle y \rangle(t) - y_0}{\langle x \rangle(t) - x_0}, \quad (4.7)$$

from the average x and y for the time dependent wavefunction

$$\langle x \rangle(t) = \sum_l |c_l(t)|^2 x_l, \quad \langle y \rangle(t) = \sum_l |c_l(t)|^2 y_l. \quad (4.8)$$



4.1.4 Simulations of wavepacket dynamics

Simulations are performed mostly for a relatively weak trap ($V_0 = 0.002$), where the wavepacket width σ is much smaller than the distance (≈ 164.5) to the trap center \mathbf{r}_0 . The trap potential gradient (i.e., the force) does not vary too much over the extent of the wavepacket. In Sec. 4.4 results are also presented for a tighter trap ($V_0 = 0.02$), where the initial distance of the wavepacket to the trap center is 10 times smaller so as to have the same force at the center of the wavepacket. The trap curvature is more significant in this case.

Fig. 4.3(b) shows the real-space evolution of the wavepacket in the weak trap. The motion of the wavepacket on this timescale is not large compared to its width. The force acts in the radial (positive x) direction. A transverse response, perpendicular to the force, is clearly visible; this is analyzed quantitatively through the time dependence of $\langle \dot{\theta} \rangle$. The following sections present a thorough comparison of numerically exact results for $\langle \dot{\theta} \rangle$ obtained through direct simulation (which is referred to as $\langle \dot{\theta} \rangle_{\text{exact}}$) with predictions from the semiclassical formalism, to be defined below.

In addition to the transverse response, there are also Bloch oscillations in the

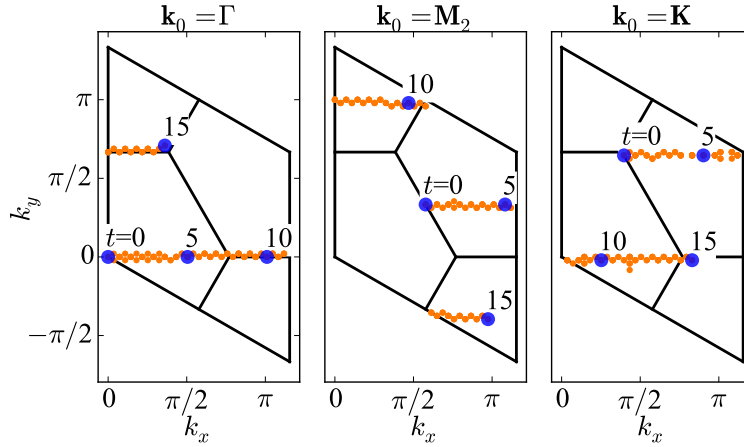


Figure 4.4: Trajectories of the wavepacket in momentum space for three initial momenta showing Bloch oscillations. The orange points represent the trajectory of the center of the wavepacket in momentum space. The blue larger circles denote the position of the wavepacket center in momentum space at four instants of time ($t = 0, 5, 10,$ and 15).

radial direction; this is not obvious in the real-space snapshots but is more evident in momentum space. The motion of the wavepacket in momentum space is obtained by taking a lattice Fourier transform of the coefficients $c_l(t)$ at each instant of time to obtain the occupancies of each momentum, denoted by $\tilde{c}_{\mathbf{k}}(t)$. This motion can be visualized by plotting the coefficients $|\tilde{c}_{\mathbf{k}}(t)|^2$ over the Brillouin zone at different instants of time, as done in Fig. 4.3(c). The wavepacket moves through the Brillouin zone at a constant velocity in the direction of the force. Due to the periodicity of the Brillouin zone, each time the wavepacket exits through the right or top boundary it re-enters through the left or bottom boundary. For visualization, Fig. 4.4 schematically shows the trajectories of the wavepacket centers starting from the three high-symmetry points.

4.2 Semiclassical dynamics

This section sets up the semiclassical framework to calculate the time evolution of $\dot{\theta}(t)$. The basic ‘point-particle’ approach is first formulated, under the standard assumption of simultaneously well-defined position and momentum. An extension is then formulated where the structure of the wavepacket in momentum space is taken into account.

In the most basic semiclassical approach, the structure of the wavepacket in both real and momentum space is ignored, so that the wavepacket or particle is described

by a sharply defined position and momentum (\mathbf{r}, \mathbf{k}) . In addition, it is also assumed that the wavepacket dynamics is completely governed by a single energy band. The semiclassical equations under the assumption that the wavepacket has support only on the lower band are

$$\frac{d\mathbf{r}}{dt} = \nabla_{\mathbf{k}} E_{-}(\mathbf{k}) - \frac{d\mathbf{k}}{dt} \times \boldsymbol{\Omega}_{-}(\mathbf{k}), \quad (4.9a)$$

$$\frac{d\mathbf{k}}{dt} = \mathbf{F}. \quad (4.9b)$$

Here $E_{-}(\mathbf{k})$ is the energy dispersion, and $\boldsymbol{\Omega}_{-}(\mathbf{k})$ is the Berry curvature of the lower band. From the second term in Eq. (4.9a), it can be seen that the Berry curvature induces a velocity perpendicular to the direction of the external force, which leads to the transverse motion of the wavepacket.

Using (4.6), the external force is given by

$$\mathbf{F}(\mathbf{r}) = -\nabla_{\mathbf{r}} V(\mathbf{r}) = -V_0((x - x_0)\hat{x} + (y - y_0)\hat{y}). \quad (4.10)$$

So, the semiclassical equations form a set of four coupled differential equations

$$v_{-,x}(\mathbf{k}) = \frac{dx}{dt} = \frac{\partial E_{-}(\mathbf{k})}{\partial k_x} + V_0(y - y_0)\Omega_{-}^z(\mathbf{k}), \quad (4.11a)$$

$$v_{-,y}(\mathbf{k}) = \frac{dy}{dt} = \frac{\partial E_{-}(\mathbf{k})}{\partial k_y} - V_0(x - x_0)\Omega_{-}^z(\mathbf{k}), \quad (4.11b)$$

$$\frac{dk_x}{dt} = -V_0(x - x_0), \quad (4.11c)$$

$$\frac{dk_y}{dt} = -V_0(y - y_0). \quad (4.11d)$$

This set of equations can be solved explicitly to track the trajectory in time of a particle in real as well as momentum space. $\langle \dot{\theta} \rangle_{-,pp-sc}$ labels the angular velocity corresponding to the real-space trajectories calculated in this way. (The subscript ‘pp-sc’ stands for ‘point-particle semiclassics’ and the $-$ sign denotes that the lower band properties have been used.) A similar calculation can be done with the characteristics of the upper band ($E_{+}(\mathbf{k})$ and $\Omega_{+}^z(\mathbf{k})$) and the angular velocity so calculated is denoted by $\langle \dot{\theta} \rangle_{+,pp-sc}$.

As observed previously, wavepackets can have support on both bands. One reasonable procedure to correctly capture the wavepacket’s motion would be to use the $\langle \dot{\theta}(t) \rangle_{-,pp-sc}$ or $\langle \dot{\theta}(t) \rangle_{+,pp-sc}$ curve, depending on whether the lower or upper band has more occupancy. A somewhat more refined procedure is taking the weighted average

of the two according to the weights W_{\mp} of the initial packet on the two bands. Hence the angular velocity calculated from the point-particle semiclassics is defined as

$$\langle \dot{\theta} \rangle_{\text{pp-sc}} = W_- \langle \dot{\theta} \rangle_{-, \text{pp-sc}} + W_+ \langle \dot{\theta} \rangle_{+, \text{pp-sc}} \quad (4.12)$$

A key assumption above is that the wavepacket can be treated like a point particle in both real and momentum space simultaneously, hence neglecting the quantum nature of the wavepacket. However in realistic quantum experiments and simulations, where the wavepacket is of finite extent, the validity of this assumption is not *a priori* clear. This formalism can be extended to take into account the finite spread of the wavepacket in momentum space. From the geometric definition $\theta = \tan^{-1} \frac{y-y_0}{x-x_0}$,

$$\dot{\theta} = \frac{(x-x_0)v_y - (y-y_0)v_x}{(x-x_0)^2 + (y-y_0)^2}. \quad (4.13)$$

By using the expressions of $v_{\pm,x}(\mathbf{k})$ and $v_{\pm,y}(\mathbf{k})$ obtained from Eq. (4.11a) and Eq. (4.11b), one can obtain the functions $\dot{\theta}_{\pm}(\mathbf{k})$ in the Brillouin zone. Their typical profiles are shown in Fig. 4.5, with parameter values corresponding to the initial position used in Fig. 4.3.

With our parameters, $E_-(\mathbf{k}) \approx -E_+(\mathbf{k})$. Also, $\Omega_+(\mathbf{k}) = -\Omega_-(\mathbf{k})$. Hence one gets $\dot{\theta}_-(\mathbf{k}) \approx -\dot{\theta}_+(\mathbf{k})$. In other words the profiles shown in Fig. 4.5 for the two bands, $\dot{\theta}_{\pm}(\mathbf{k})$, are nearly but not exactly negative of each other.

These profiles of $\dot{\theta}_{\pm}(\mathbf{k})$ can be used to calculate the evolution of the angular velocity in time by taking a weighted average of $\dot{\theta}_{\pm}(\mathbf{k})$, the weights being the occupancies of the wavefunction in momentum space ($|\tilde{c}_{\mathbf{k}}(t)|^2$) multiplied by the weights in each band (W_{\pm}) defined in Eq. (4.4). The angular velocity calculated this way is denoted as $\langle \dot{\theta} \rangle_{\text{wp-sc}}(t)$, the ‘wp’ as a reminder that the wavepacket structure is taken into account. Thus

$$\begin{aligned} \langle \dot{\theta}(t) \rangle_{\text{wp-sc}} &= W_- \langle \dot{\theta}(t) \rangle_{-, \text{wp-sc}} + W_+ \langle \dot{\theta} \rangle_{+, \text{wp-sc}} \\ &= W_- \sum_{\mathbf{k} \in \text{BZ}} |\tilde{c}_{\mathbf{k}}(t)|^2 \dot{\theta}_-(\mathbf{k}) + W_+ \sum_{\mathbf{k} \in \text{BZ}} |\tilde{c}_{\mathbf{k}}(t)|^2 \dot{\theta}_+(\mathbf{k}) \\ &= \sum_{\mathbf{k} \in \text{BZ}} |\tilde{c}_{\mathbf{k}}(t)|^2 \left[W_- \dot{\theta}_-(\mathbf{k}) + W_+ \dot{\theta}_+(\mathbf{k}) \right] \end{aligned} \quad (4.14)$$

This procedure assumes that the force does not change along the spatial extent of the wavepacket; the spread of the wavepacket in momentum space is taken into account while a point-particle description is used in real space. Therefore, this description will break down when the force varies significantly within the real-space support region of the wavepacket (Sec. 4.4). In addition, note that this is not a computationally

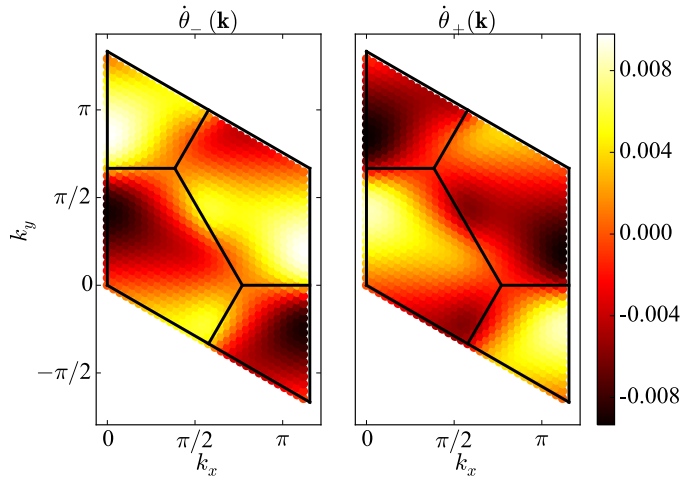


Figure 4.5: Profiles of $\dot{\theta}_-(\mathbf{k})$ and $\dot{\theta}_+(\mathbf{k})$ in the Brillouin zone as calculated from combining the semiclassical equations of motion (4.9a) and the kinematic relation in (4.13). The coordinates of the center of the mass of the wavepacket in real space relative to the center of the trap are given by $x - x_0 = -164.5$ and $y - y_0 = 0.5$, and the trap strength is $V_0 = 0.002$. Here $\dot{\theta}_-(\mathbf{k})$ and $\dot{\theta}_+(\mathbf{k})$ have nearly but not exactly equal and opposite values, $\dot{\theta}_-(\mathbf{k}) \approx -\dot{\theta}_+(\mathbf{k})$.

advantageous approximation for the time evolution, since we are anyway solving the full problem in order to obtain the Fourier transform $\tilde{c}_{\mathbf{k}}(t)$. The purpose here is to investigate whether (and how much) taking the momentum-space spread into account improves the semiclassical description.

In this chapter, the focus is on parameter regimes such that the wavepacket does not have large displacements in real space within the time scales $t \lesssim 20$ of interest (Fig. 4.3). Therefore, a further simplifying assumption is made and $\dot{\theta}$ is taken as position independent, setting \mathbf{r} to be initial position of the wavepacket at $t = 0$, and use the resulting distribution of $\dot{\theta}$ to calculate the average.

4.3 Comparison of semiclassical predictions with exact dynamics

In this section, a comparison between the angular velocities of the wavepacket obtained from the exact simulations, ($\langle \dot{\theta} \rangle_{\text{exact}}$) to those obtained from the semiclassical calculations ($\langle \dot{\theta} \rangle_{\text{pp-sc}}$ and $\langle \dot{\theta} \rangle_{\text{wp-sc}}$) is presented and the regimes of validity of the semiclassical framework are discussed

In Fig. 4.6 the angular velocities are plotted as a function of time for the setup

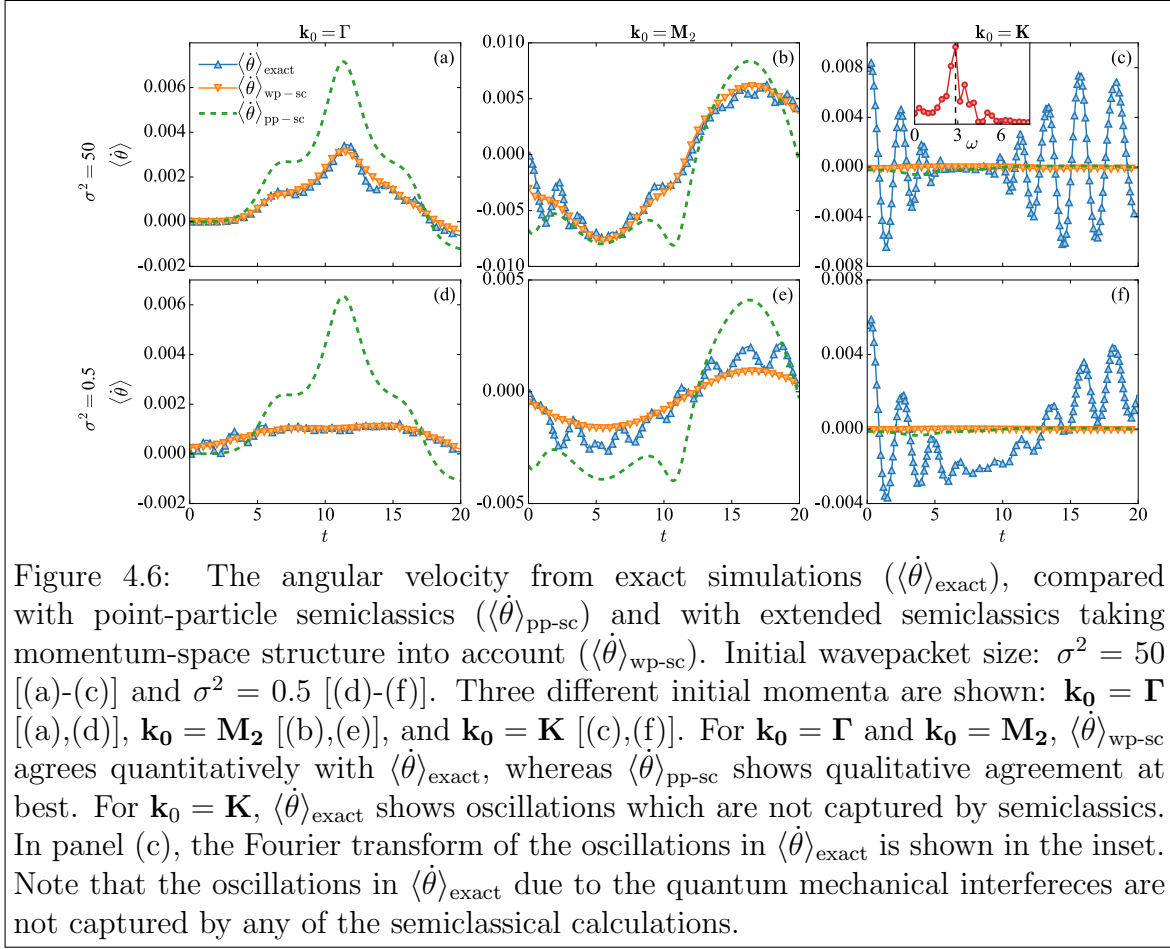


Figure 4.6: The angular velocity from exact simulations ($\langle \dot{\theta} \rangle_{\text{exact}}$), compared with point-particle semiclassics ($\langle \dot{\theta} \rangle_{\text{pp-sc}}$) and with extended semiclassics taking momentum-space structure into account ($\langle \dot{\theta} \rangle_{\text{wp-sc}}$). Initial wavepacket size: $\sigma^2 = 50$ [(a)-(c)] and $\sigma^2 = 0.5$ [(d)-(f)]. Three different initial momenta are shown: $\mathbf{k}_0 = \Gamma$ [(a),(d)], $\mathbf{k}_0 = \mathbf{M}_2$ [(b),(e)], and $\mathbf{k}_0 = \mathbf{K}$ [(c),(f)]. For $\mathbf{k}_0 = \Gamma$ and $\mathbf{k}_0 = \mathbf{M}_2$, $\langle \dot{\theta} \rangle_{\text{wp-sc}}$ agrees quantitatively with $\langle \dot{\theta} \rangle_{\text{exact}}$, whereas $\langle \dot{\theta} \rangle_{\text{pp-sc}}$ shows qualitative agreement at best. For $\mathbf{k}_0 = \mathbf{K}$, $\langle \dot{\theta} \rangle_{\text{exact}}$ shows oscillations which are not captured by semiclassics. In panel (c), the Fourier transform of the oscillations in $\langle \dot{\theta} \rangle_{\text{exact}}$ is shown in the inset. Note that the oscillations in $\langle \dot{\theta} \rangle_{\text{exact}}$ due to the quantum mechanical interferences are not captured by any of the semiclassical calculations.

corresponding to that shown in Fig. 4.3(a) for two different sizes and three different initial wavepacket momenta, Γ , \mathbf{M}_2 and \mathbf{K} . Before detailed discussions, some observations are as follows:

- For the Γ point and \mathbf{M}_2 point initial states, $\langle \dot{\theta} \rangle_{\text{pp-sc}}$ shows similar overall qualitative features as the evolution of the exact $\langle \dot{\theta} \rangle_{\text{exact}}$, but it generally fails to quantitatively reproduce the evolution. On the other hand, $\langle \dot{\theta} \rangle_{\text{wp-sc}}$ reproduces many of the prominent features of the $\langle \dot{\theta}(t) \rangle_{\text{exact}}$ curve.
- For the \mathbf{K} point initial state, there seems to be no noticeable agreement.
- There is generally better agreement between the semiclassics and the exact evolution for the wavepacket that is larger in real space ($\sigma^2 = 50$, top row) compared to the smaller wavepacket ($\sigma^2 = 0.5$, bottom row).
- For the larger wavepacket, the Γ point initial state is almost completely in the lower band ($W_- = 0.999$) and the \mathbf{M}_2 point initial state is almost completely in the upper band ($W_+ = 0.985$). Hence, using only the lower band (Γ) or only the

upper band (\mathbf{M}_2) would give very nearly the same semiclassical curves as the ones shown, which are W_{\pm} -weighted mixtures.

- For the smaller wavepacket, the same is true with the Γ point initial state ($W_- = 0.99$), but the \mathbf{M}_2 point initial state now has significant contribution from the lower band as well ($W_+ = 0.74$). This leads to cancellation of the weighted mixtures, so that, comparing panels (b) and (e), we see much smaller values of $\langle \dot{\theta} \rangle$ for the smaller wavepacket.
- For the \mathbf{K} point initial state, the contributions of the two bands largely cancel each other, resulting in tiny semiclassical predictions for $\langle \dot{\theta}(t) \rangle$.

The larger wavepacket is now discussed in details. A wavepacket with zero initial momentum has support almost completely on the lower band ($W_- = 0.999$), hence the relevant profile of angular velocity is $\dot{\theta}_-(\mathbf{k})$. At the zero momentum (Γ) point, both the gradient of the band dispersion and the Berry curvature in the lower band are zero, leading to a zero angular velocity. As a result, the wavepacket starts with zero $\dot{\theta}$. From the momentum space trajectory in Fig. 4.4(a) and the Brillouin zone profile of Fig. 4.5, one can infer that the wavepacket mostly moves through regions of near-zero $\dot{\theta}$. As a result, the $\dot{\theta}$ remains relatively small as seen in Fig. 4.6(a). The momentum-space shape of the packet plays a strong role in this case: as the trajectory lies roughly between positive and negative regions of $\dot{\theta}_-(\mathbf{k})$, small variations of the shape can cause $\dot{\theta}$ to vary between positive and negative values. Accordingly, the dynamics of $\langle \dot{\theta}(t) \rangle_{\text{exact}}$ is captured notably better by the extended semiclassics $\langle \dot{\theta} \rangle_{\text{wp-sc}}$ than by the point-particle approximation $\langle \dot{\theta} \rangle_{\text{pp-sc}}$.

As discussed in Sec. 4.1.2, the wavepacket with initial momentum at \mathbf{M}_2 has support almost entirely on the upper band ($W_- = 0.015$), hence the upper band characteristics are more relevant here. At the \mathbf{M}_2 point, although the gradient of the band dispersion vanishes, the Berry curvature has a sharp peak [see Fig. 4.1(c)]. As a result, the wavepacket gains a finite angular velocity almost immediately at $t \approx 0$. (Note that the semiclassical approximations, by construction, start with nonzero $\dot{\theta}$ at $t = 0$, which is the value of $\dot{\theta}$ at the \mathbf{M}_2 point. The physical or exact $\dot{\theta}$ starts at zero.) Considering the trajectory Fig. 4.4(b) and the Brillouin zone profile of Fig. 4.5, note that the trajectory moves through regions of large $\dot{\theta}$; this is reflected in the larger absolute values of Fig. 4.6(b). The trajectories in momentum space intersect regions of $\dot{\theta}_+(\mathbf{k}) < 0$ for $t \lesssim 10$ to explore regions $\dot{\theta}_+(\mathbf{k}) > 0$ at later times. The change of sign can be seen in Fig. 4.6(b) in all three curves.

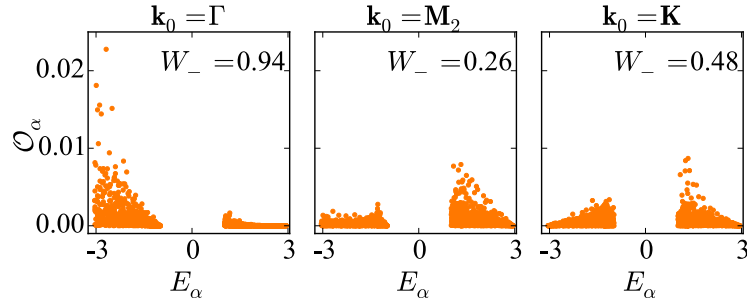
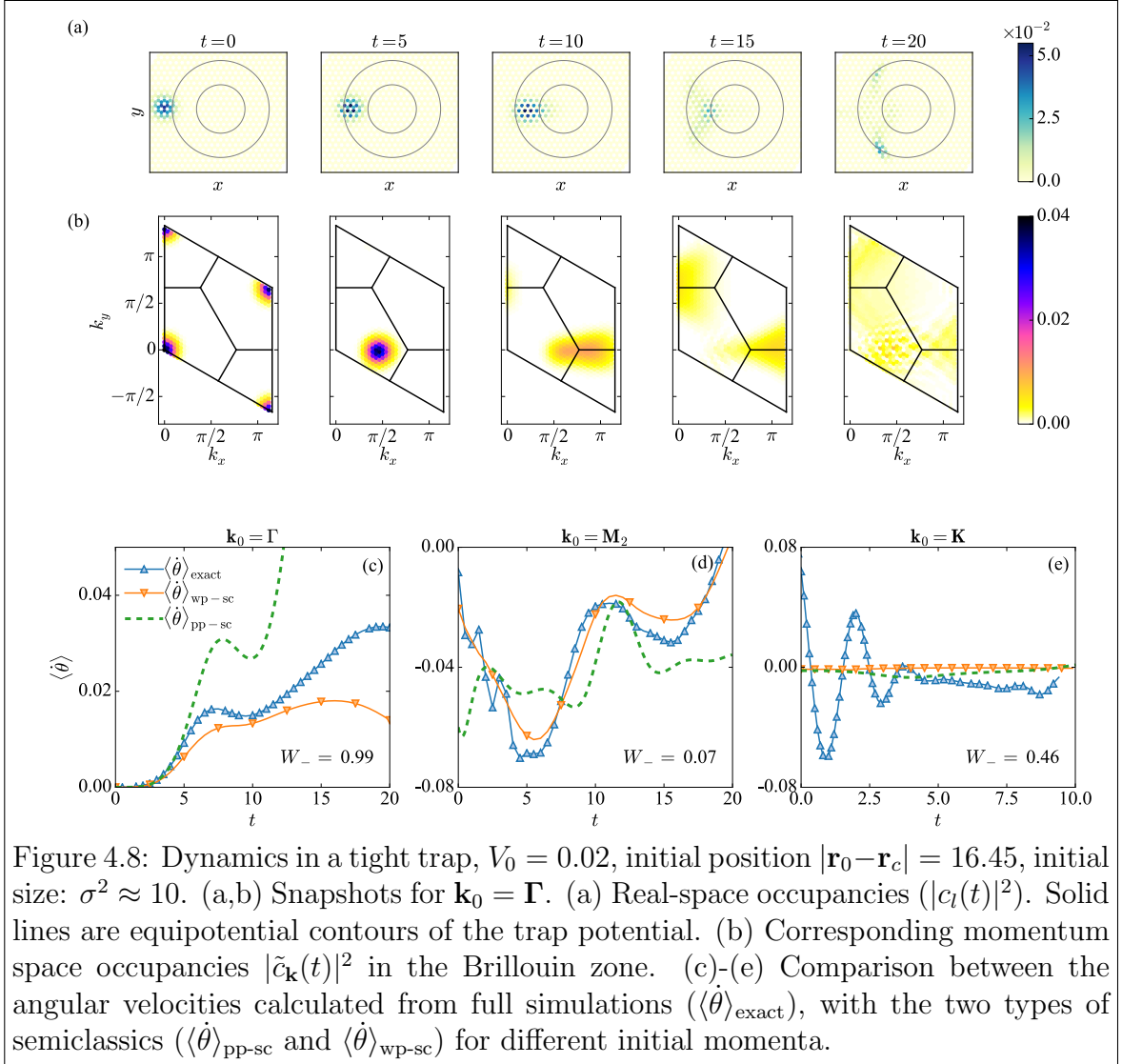


Figure 4.7: Overlaps as in Fig. 4.2(a), for a smaller wavepacket, $\sigma^2 = 0.5$. Comparing with the case of $\sigma^2 = 50$ [Fig. 4.2(a)], this smaller wavepacket has a much more spread-out distribution of weights on the eigenstates of \mathcal{H}_{HM} . The weight of the wavepackets in the lower band W_- are all closer to $1/2$ compared to the larger wavepacket of Fig. 4.2, where we had $W_- = 0.999, 0.015, 0.457$ for these three momenta.

For the wavepacket with $\mathbf{k}_0 = \mathbf{K}$, the dynamics of $\langle \dot{\theta} \rangle_{\text{exact}}$ shows pronounced oscillations which preclude meaningful comparison with the semiclassical predictions. The oscillations are due to the fact that the initial state created according to Eq. 4.3 has significant weight on both lower and upper bands ($W_- = 0.457$), with a relatively well-defined energy gap between eigenstates occupied in the lower band and eigenstates occupied in the upper band. This is seen from the overlaps plotted in Fig. 4.2(a). A Fourier transform of the $\langle \dot{\theta}(t) \rangle_{\text{exact}}$, inset to Fig. 4.6(c), shows that the dominant frequency (peak around ≈ 2.8 with width ≈ 0.3) matches the energy difference (≈ 2.6) between eigenstates of high overlap, Fig. 4.2(a) top right. The weighted band averages shown as semiclassical predictions stay near zero, which could be thought of as the value around which the exact $\langle \dot{\theta}(t) \rangle_{\text{exact}}$ oscillates, but it is currently unclear whether this is a coincidence. It is also currently unclear whether a more sophisticated way of incorporating multiple bands might allow the semiclassics to reproduce the oscillatory behavior or the average curve around which $\langle \dot{\theta}(t) \rangle_{\text{exact}}$ oscillates.

In the lower panels of Fig. 4.6, an initial wavepacket with $\sigma^2 = 0.5$ is used. The Gaussian wavepacket is centered at the center of a hexagon in real space, so that even with such a small σ there are six sites equally occupied. $\langle \dot{\theta}(t) \rangle_{\text{exact}}$ now deviates significantly from $\langle \dot{\theta} \rangle_{\text{pp-sc}}$. The extended semiclassics, $\langle \dot{\theta} \rangle_{\text{wp-sc}}$, continues to describe the overall behavior, for the Γ point and \mathbf{M}_2 point initial states. The exact dynamics now shows oscillations for all three initial momenta. This can be understood through the overlap distribution, shown in Fig. 4.7. For the smaller packet, the overlaps are spread out more in energy and also are far more biased toward more equal occupancies of the two bands (W_- values are closer to $\frac{1}{2}$ compared to the corresponding values



for the bigger packet). As a result, interference oscillations are visible also for the Γ point and \mathbf{M}_2 point initial states, panels (d) and (e) in Fig. 4.6.

4.4 Semiclassics in a tight trap

In Sec. 4.3 it was shown that, as the spread of the initial wavepacket in real space is made bigger, the agreement between the results from the semiclassical approximations and exact simulations improves. The idea is that, increasing size in real space corresponds to decreasing size in momentum space (as reflected also in decreasing spread in energy space); thus the point-particle approximation in momentum space is more justified. However, increasing real-space size can also lead to violation of semiclassics, as the semiclassical equations of motion also assume sharply defined po-

sition. One effect is that the finite spread of the wavepacket in real space could lead to different potential gradients (different forces) at different points within the wave packet. This effect would not play a role for a constant gradient but can occur in a harmonic trap. This kind of ‘tidal’ force makes the point particle notion less justified in real space.

In order to characterize this effect, consider the geometry of Fig. 4.8(a) with $V_0 = 0.02$, one order of magnitude stronger than that in Fig. 4.3. The distance between the center of the trap and the center of the wavepacket is adjusted such that the force at the center of the wavepacket remains the same compared to the geometry shown in Fig. 4.3(a). It can be seen from Fig. 4.8(a) that, in the course of time evolution, the wavepacket breaks apart, spreads out and does not keep the notion of a well defined wavepacket as compared to the shallower trap [Fig. 4.3]. This is also reflected in the evolution of the wavepacket in momentum space as shown in Fig. 4.8(b). For similar time scales as those studied in previous sections, the wavepacket in momentum space gets distorted and diffuses completely, unlike the case in Fig. 4.3(c) where there is still a notion of a well defined peak centered around some value of momentum. Quite surprisingly, our semiclassical calculation does not seem to fail completely even in this extreme case since $\langle \dot{\theta} \rangle_{\text{wp-sc}}$ and $\langle \dot{\theta} \rangle_{\text{exact}}$ still agree qualitatively [see Fig. 4.8]. Even the point-particle semiclassics, $\langle \dot{\theta} \rangle_{\text{pp-sc}}$, reproduces qualitatively some of the peaks and dips of the exact curve.

As in previous cases, for $\mathbf{k}_0 = \mathbf{K}$ there are strong oscillations due to occupancies in both bands.

4.5 Summary

This chapter explored the dynamics of a gaussian wavepacket, with and without initial crystal momentum, on the Haldane’s honeycomb model in the presence of external forces provided by a harmonic potential. The focus was on short-time dynamics and comparisons of the dynamics were made to semiclassical treatments. Semiclassical descriptions of wavepacket dynamics are obviously appealing, but the range of applicability is poorly explored. The aim of this chapter can be regarded as a step toward obtaining detailed understanding on the regimes of validity of the semiclassical manner of predicting trajectories. Formally, single-particle dynamics was treated, but our considerations should be applicable to non-interacting Bose condensates, and approximately to weakly interacting Bose condensates.

It was shown that the point-particle semiclassics reproduces many qualitative features even for wavefunctions that are quite small in real space, and hence extended over non-negligible portions of the Brillouin zone. When this momentum-space extent is taken into account, the agreement can be excellent even when the point-particle approximation fails. This shows that the basic idea of semiclassics, following position and momentum simultaneously, can correctly embody quantum dynamics even when the point-particle approach fails. Using a tight trap, it was shown that this extended semiclassical approach can function reasonably even when the wavepacket is completely distorted or even torn apart (Fig. 4.8). While this is reassuring for the philosophy behind semiclassics, it does not immediately lead to a computationally advantageous approximation, since to obtain the momentum-space structure we first evolved the complete system in time (i.e. solved the problem computationally). However, one can envision an extended semiclassics where the wavepacket in momentum space is assumed to have fixed shape and the center moves according to the point-particle equations (4.9).

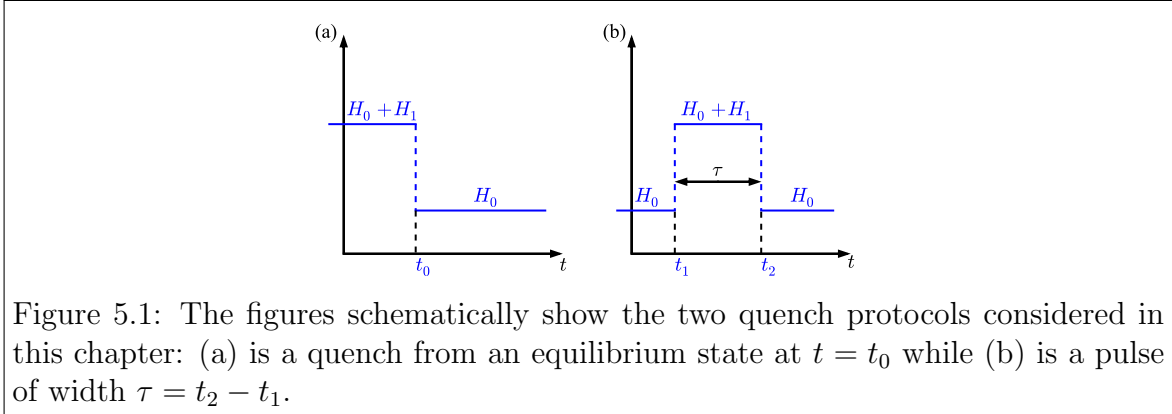
Chapter 5

Spatially local quenches as a probe for Chern insulators

In the previous chapter, it was shown how the non-equilibrium responses can be used to probe the Berry curvature, which encodes the bulk topology of the system. This chapter focusses on the complementary physics of non-equilibrium responses of edge states, which via bulk-boundary correspondence are manifestations of the bulk topology, by studying the effect of *local* quenches on Chern bands filled with fermions. We focus particularly on the real-time chiral response of the edges.

Two kinds of quantum quenches shown schematically in Fig. 5.1 are considered: a single quench and a pulse consisting of two sudden changes of the Hamiltonian. The background Hamiltonian H_0 is taken to be a tight-binding model with topologically non-trivial bands. The perturbing Hamiltonian H_1 is chosen to be a localized density perturbation of the system. In the first case, the initial state is the ground state of $H_0 + H_1$, and then the local perturbation H_1 is removed and time evolution of the state under the Hamiltonian H_0 is followed. In the second case the initial state is the ground state of H_0 and the local perturbation H_1 is turned on for a finite time interval τ .

First a system with open boundary conditions at half-filling is considered (Section 5.2). In this case, the edge of the fermionic system is simply the edge of the lattice. Next, motivated by experiments with cold atomic systems, the effect of power-law traps is explored (Section 5.3), i.e., traps of the form $\sim r^\gamma$. In cold-atom experiments, the atoms are usually loaded in a harmonic trap, i.e., $\gamma = 2$. Since systems in harmonic traps often do not have a well-defined sharp edge, there is significant interest in power-law traps with large exponents γ , which are expected to be more similar to a system with sharp boundaries [Goldman *et al.* (2013); Dauphin and Goldman (2013); Gaunt *et al.* (2013); Meyrath *et al.* (2005)]. Accordingly, fermions



in a Chern band in the presence of a power-law trapping potential $J(r/r_0)^\gamma$ are considered, where J is the hopping energy that sets the energy width of the bands. The parameter r_0 then functions as a trapping length scale, determining the spatial extent of the trapped fermionic cloud [Goldman *et al.* (2013); Dauphin and Goldman (2013); Aidelsburger *et al.* (2015)].

The equilibrium properties in such a trap are first analyzed and then the effect of local quenches on it is studied.

The main findings are as follows. When the bands are topologically non-trivial, a local quench of a site potential at the edge generates a spatially localized pulse that propagates chirally around the edge of the sample. This is a straightforward and very direct manifestation of the topological nature of H_0 . The front of the pulse has speed determined by the hopping scale J , but the peak of the pulse has smaller speed for smaller bulk gaps at the relevant points in the Brillouin zone. This phenomena is attributed to the increasingly poor localization of the edge states as the gap decreases; the perturbation is spread out over increasingly more lattice sites rendering the sharp boundary picture less accurate. In the second part, considering power-law traps with large exponents γ , it is shown how the trap parameter r_0 determines an optimal particle number for mimicking the half-filling situation, and hence for observing the chiral nature of the edge states.

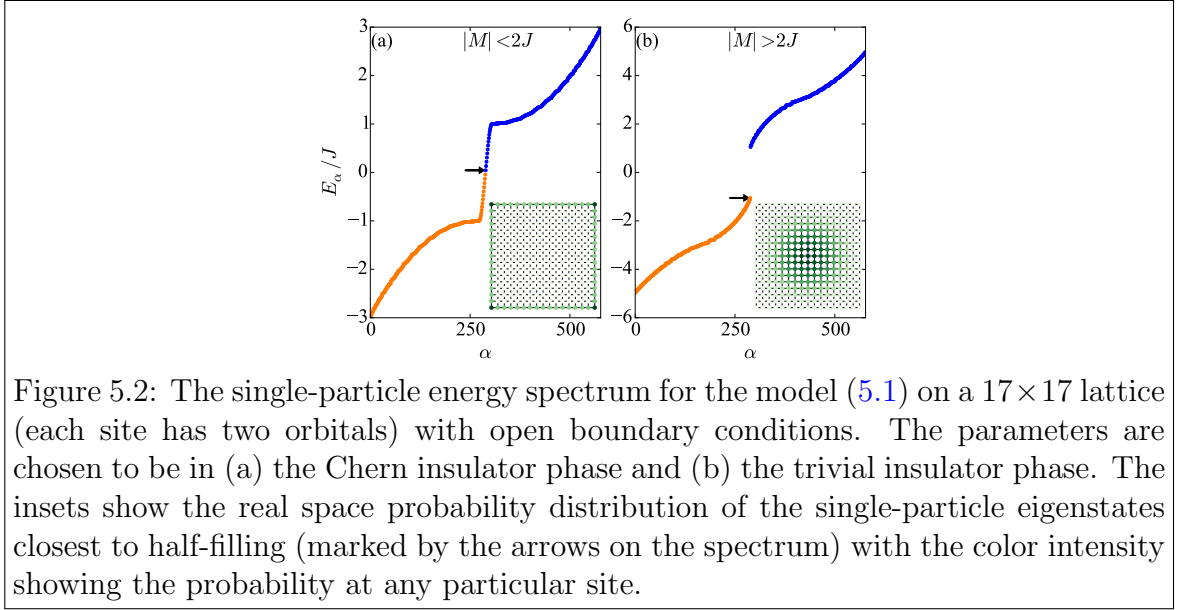


Figure 5.2: The single-particle energy spectrum for the model (5.1) on a 17×17 lattice (each site has two orbitals) with open boundary conditions. The parameters are chosen to be in (a) the Chern insulator phase and (b) the trivial insulator phase. The insets show the real space probability distribution of the single-particle eigenstates closest to half-filling (marked by the arrows on the spectrum) with the color intensity showing the probability at any particular site.

5.1 Model Hamiltonian and quench protocols

To study the dynamics following a quench, the Chern insulator model on square lattice described in Chapter 2 is used governed by the Hamiltonian

$$\mathcal{H}_{\text{CI}} = \left[- \sum_{\mathbf{r}} \left(\Psi_{\mathbf{r}}^\dagger \frac{J_1 \sigma^z + i J_2 \sigma^x}{2} \Psi_{\mathbf{r}+\hat{x}} + \Psi_{\mathbf{r}}^\dagger \frac{J_1 \sigma^z + i J_2 \sigma^y}{2} \Psi_{\mathbf{r}+\hat{y}} - \frac{M}{2} \Psi_{\mathbf{r}}^\dagger \sigma^z \Psi_{\mathbf{r}} \right) \right] + \text{h.c.} \quad (5.1)$$

with hopping $J_1 = J_2 = J$ between the sub-lattices and a staggered chemical potential M . At half-filling such a single particle Hamiltonian represents a Chern insulator with chiral edge states whenever $-2J < M < 2J$. The topological and trivial eigenstates for a finite sample are shown in Fig. 5.2 (a) and (b) respectively, together with the real space probability distribution of the eigenstates closest to zero energy ($E = 0$). In the trivial case, there are no edge states whereas for the Chern insulator, the edge states are clearly visible. At half-filling the Chern insulator state has a Hall conductivity $\sigma_{xy} = Ce^2/h$ where $C = 1$ is the Chern number of the filled lower band.

In Section 5.2 $H_0 = H_{\text{CI}}$ while in Section 5.3 a trapping potential H_{trap} (to be defined later on) will be added to the Hamiltonian: $H_0 = H_{\text{CI}} + H_{\text{trap}}$.

The relevant physical processes are where the system described by Hamiltonian H_0 is acted upon by two types of perturbation. The first is of the form

$$H_e(t) = H_1 \theta(t_0 - t), \quad (5.2)$$

which is referred to as a *quench from equilibrium* [see Fig. 5.1(a)] and the second is defined as

$$H_e(t) = H_1 [\theta(t - t_1) - \theta(t - t_2)], \quad (5.3)$$

that is non-zero for a time $\tau = t_2 - t_1$, and is referred to as a *pulse* [see Fig. 5.1(b)]. The focus is on local density perturbations that we label H_1 . A local density perturbation is defined as an increase or deficit of the charge density around a particular site l with magnitude μ_l

$$H_1^l = \mu_l c_l^\dagger c_l, \quad (5.4)$$

Here no implicit summation is assumed over the site index, but there is an automatic summation over the sublattice index, since c_l and c_l^\dagger are two-spinors.

Next, time evolution is studied by evolving the one-particle density matrix, or the matrix of correlators, $\varrho_{ij} = \langle c_i^\dagger c_j \rangle$; here i, j are site indices and the sublattice indices are implicit. The results are presented by plotting the total densities at each site i , which correspond to the diagonal terms of the correlation matrix, ϱ_{ii} , relative to $\varrho_{ii,0}$, the density at site i calculated from H_0 , with sublattice summation implied.

5.2 Half-filled open-boundary system

In this section, rectangular open-boundary systems (without a trap) are considered with $L = L_x \times L_y$ sites at half filling. The chirality of the topological edge states is explored through perturbations of the form (5.4).

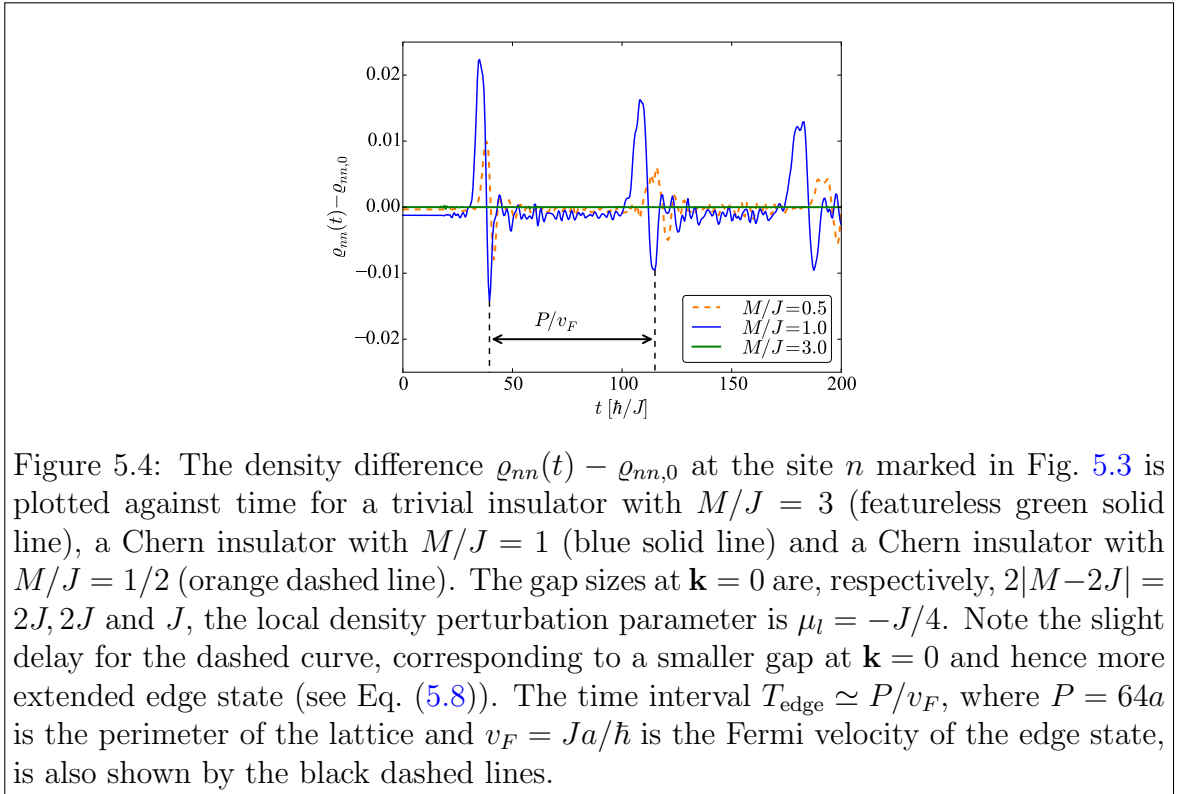
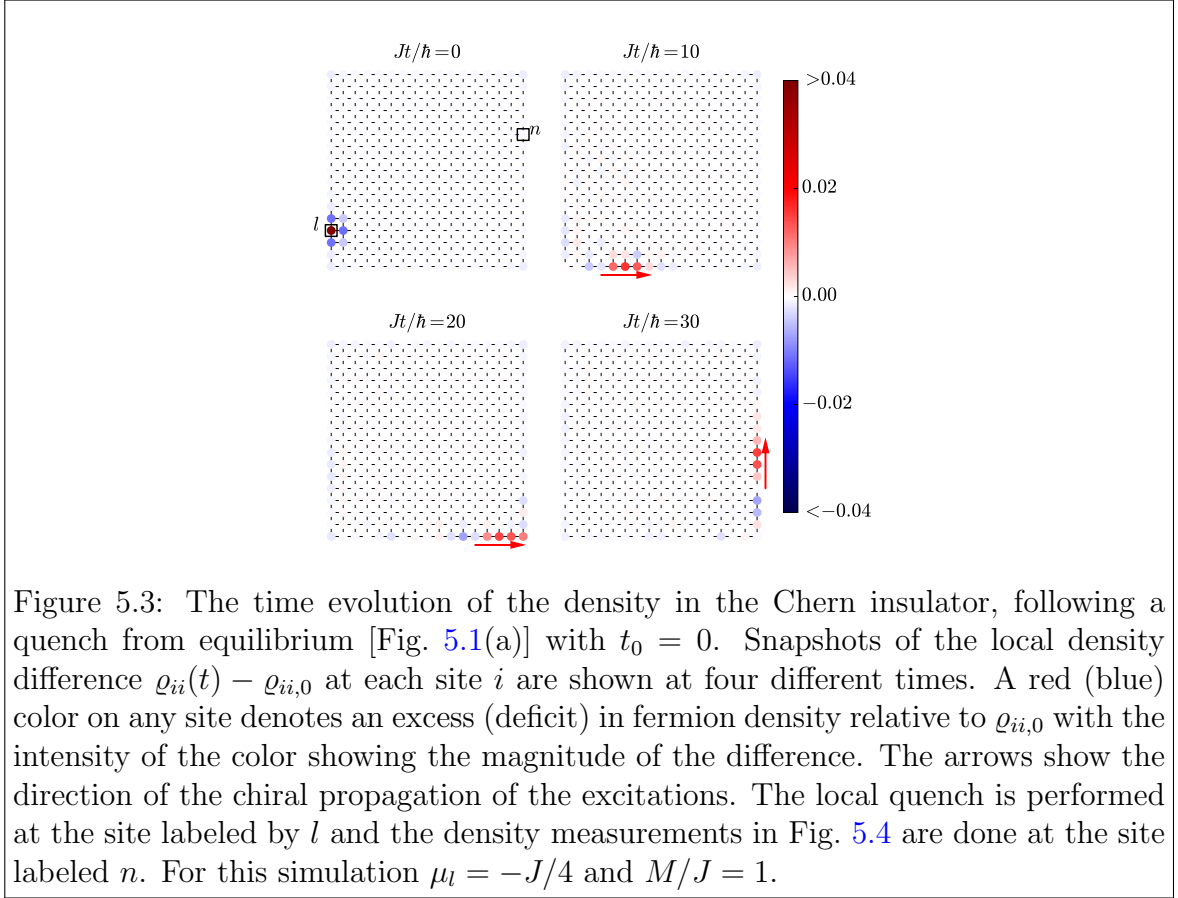
5.2.1 Local density quench from equilibrium

Start with a local density quench, of the type of Fig. 5.1(a), at an edge site l ,

$$H(t) = H_0 + H_1^l \theta(t_0 - t), \quad (5.5)$$

with $H_0 = H_{CI}$ and H_1^l given by (5.4). Through the action of H_1^l the initial ground state has different density at site l compared to the ground state of H_0 . The perturbation μ_l has equal effect on both sublattice components. The particle number is fixed to $N = L_x \times L_y$, i.e. half-filling.

Fig. 5.3 shows the time evolution by presenting four snapshots of the local density difference $\varrho_{ii}(t) - \varrho_{ii,0}$ between the density at site i ($\varrho_{ii}(t)$) and the one corresponding to the half-filled ground state of H_0 . It is clear from the snapshots that the perturbations travel along the edge of the simulated lattice with a well-defined chirality, in this case



counterclockwise. The effect of the perturbation on the edge site labeled n , marked in Fig. 5.3, is shown in Fig. 5.4. The density difference at site n shows a periodic pattern with a period $T_{\text{edge}} \simeq P/v_F$, where P is the perimeter of the lattice and v_F is the Fermi velocity of the edge state. The perimeter for this particular simulation is $P = 16 \times 4 = 64$, where the length is in units of the lattice constant which is set to unity.

In order to shed light on these numerical results, the value of v_F and the localization length of the edge is estimated from the low energy theory of the model (5.1). To do so, H_0 is expanded around each high-symmetry point of the Brillouin zone, $\mathbf{k}^{(i,j)} = \pi(i, j)$ with $i, j = 0, 1$. The emergent effective low energy model is a massive Dirac equation around each of them that takes the form

$$H^{(i,j)}(\mathbf{k}) = -J [(-1)^i k_x + (-1)^j k_y] + m_{(i,j)} \sigma_z, \quad (5.6)$$

with four mass terms defined by

$$m_{(i,j)} = M - [(-1)^i + (-1)^j] J. \quad (5.7)$$

If $|M/J| < 2$, i.e. in the topological phase, only three out of the four mass terms have the same sign. On the other hand when $|M/J| > 2$, the trivial state, all of them have the same sign. For $M/J > 0$ (< 0) the boundary between the Chern insulator and a trivial insulator (e.g. vacuum) is modelled by choosing $m_{(0,0)} = m(y)$ ($m_{(\pi,\pi)} = m(y)$) such that $m(y)$ changes sign at the boundary, which we take to be at $y = 0$. The corresponding Dirac equation has only k_x as a good quantum number and has a gapless solution that decays exponentially as [Ludwig *et al.* (1994)]

$$\Psi_{\text{edge}}(y) \sim e^{-\int_0^y m(y') dy'} \begin{bmatrix} 1 \\ 1 \end{bmatrix}. \quad (5.8)$$

Fixing $M/J > 0$, a sharp edge can be modeled by $m(y) = m_{(0,0)} [\theta(y) - \theta(-y)]$, that determines the localization of the edge state to be inversely proportional to $|M - 2J|$ (the case where $M/J < 0$ is obtained by simply replacing $m_{(0,0)} \rightarrow m_{(\pi,\pi)}$). Such an edge state has a dispersion $E = \pm v_F k_y$ ($E = \pm v_F k_x$) for edges along the y (x) direction. The sign is determined by the sign of the Chern number C of the lower band and v_F is set by the bulk dispersion Fermi velocity. For this model it is isotropic and takes the value $v_F = J$ (in units of \hbar).

From this analysis it follows that, if $m_{(0,0)}$ is reduced, the edge states will have a finite extent, having in general support on several columns close to the edge. This in turn will affect the period between the density pulses reaching a particular site,

i.e., the period between the peaks in Fig. 5.4. Since the edge perturbation now has more sites to explore as it propagates, one expects that the front of the propagating wave travels at the same speed as in a narrow edge, but the peak of the density wave will travel more slowly due to the larger width of the propagation channel. This effect is shown in Fig. 5.4 where the local density $\rho_{nn}(t)$ at a site n is shown for two different instances within the Chern insulator phase, corresponding to $M/J = 1$ and $M/J = 1/2$. Fig. 5.4 shows how the highest crest of the oscillations shifts to later times as $|M - 2J|$ decreases from J to $J/2$ as argued above. The speed of the front of the wave is apparently unaltered as expected because v_F is independent of $m_{(0,0)}$.

Such an effect is observable in a simple toy model of the conducting chiral edge by analyzing how a perturbation propagates along a conducting strip modeled as a trivial tight binding square lattice of linear dimensions $l_x \times l_y$ with $l_x \gg l_y$, as a function of the strip thickness l_y . Although in this case the propagation is not chiral and thus an exact comparison is not possible, the wavepacket indeed explores more sites as l_y is increased, which effectively reduces the peak velocity in the x direction, similar to what is observed for the Chern insulator edge.

The apparent decay of the main peak in Fig. 5.4 on the other hand is likely to be due to the spread of the wavepacket along the edge rather than decay into the bulk. The latter is strongly suppressed by the initial perturbation being localized at the edge, having therefore no overlap with bulk states.

Fig. 5.4 also shows data for the trivial insulator case, $M/J = 3$ (featureless solid green line). There is no chiral propagation in this case due to the absence of edge states, so there are no features observed in the density at site n .

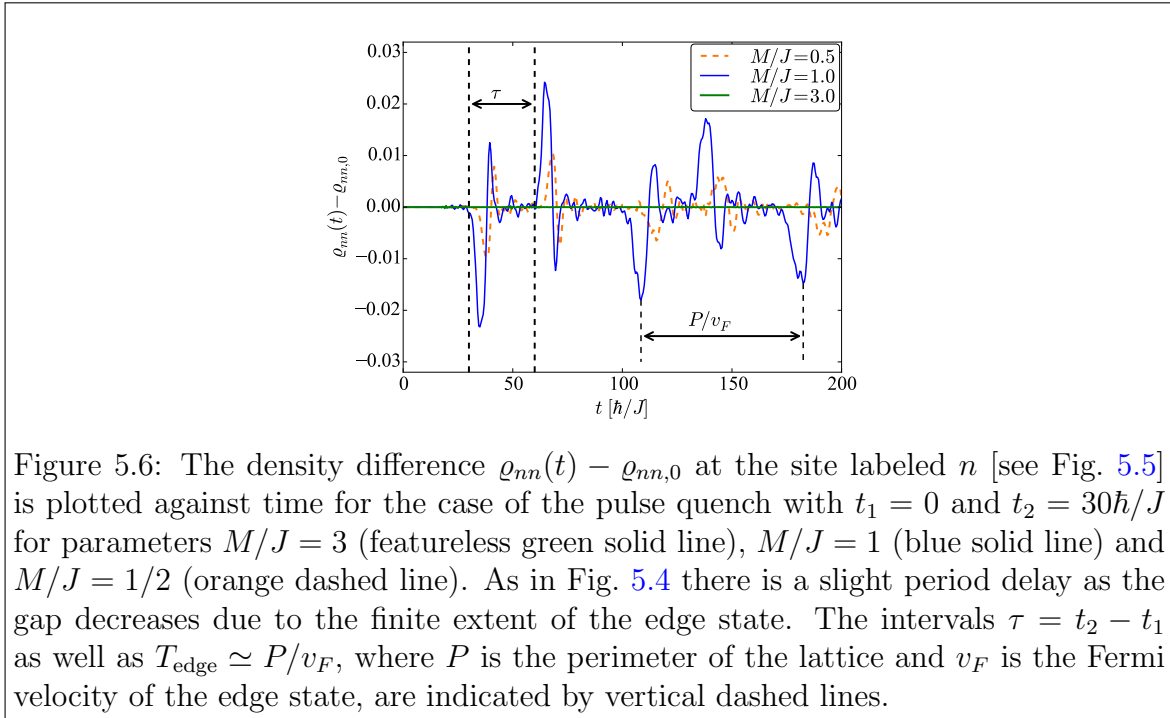
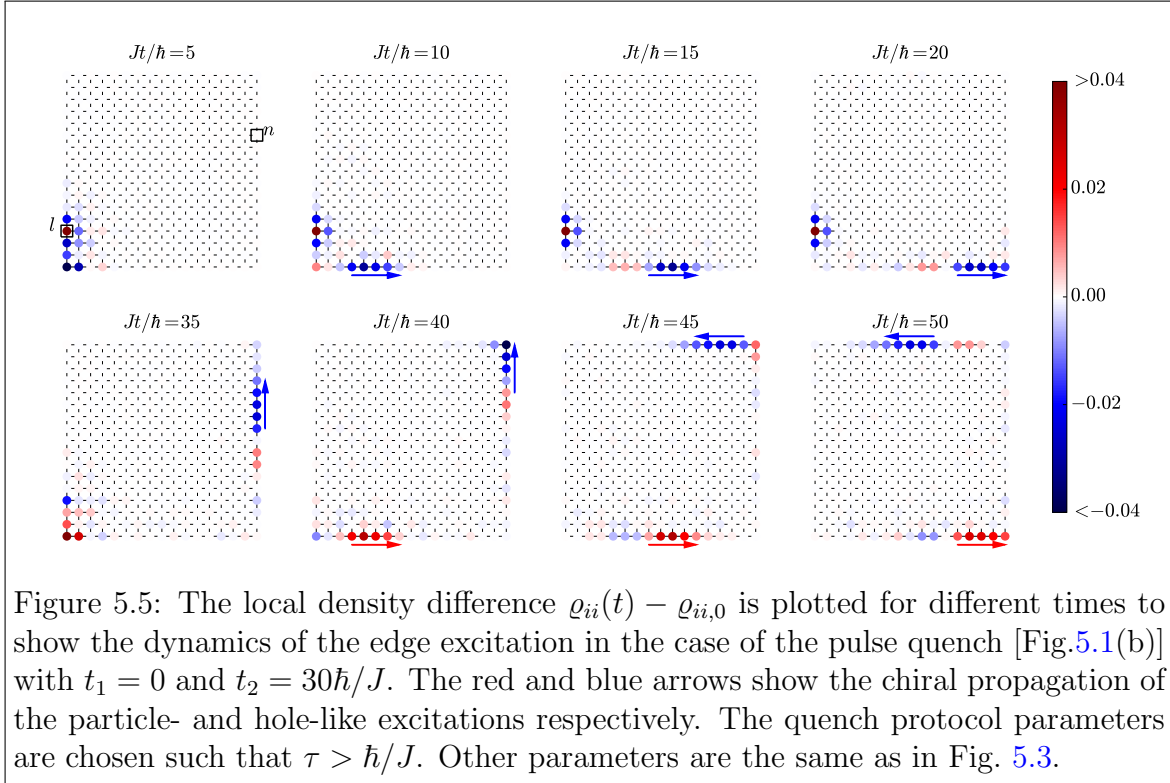
Finally, the decay of a local perturbation at a bulk site is also studied, as a function of the gap size. The resulting disturbance spreads out in all directions and there is no notion of chirality in the propagation of the excitation. Further, no correlation with the gap are found. This is attributed to the fact that a spatially localized bulk perturbation is strongly delocalized in momentum space and thus it is insensitive to the size of the gap.

5.2.2 Local density pulse

A density perturbation pulse [see Fig. 5.1(b)] of width τ is now studied,

$$H(t) = H_0 + H_1^l [\theta(t - t_1) - \theta(t - t_2)], \quad (5.9)$$

with $H_0 = H_{\text{CI}}$ and $\tau = t_2 - t_1$. Without loss of generality we choose $t_1 = 0$ and $t_2 = \tau$.



As before, focussing on a local edge perturbation (at site l) the time evolution is studied as a function of τ . Since the relevant energy scale is J one expects two different regimes depending on whether $\tau < \hbar/J$ or $\tau > \hbar/J$. Indeed, in the former case ($\tau < \hbar/J$) the perturbation is too localized in time to react separately to both the turning on of the perturbation at t_1 and releasing at t_2 . Accordingly, the system generates a single signal traveling along the edge of the system, which is allowed to conduct chirally due to the non-trivial topology of the Hamiltonian. Such a disturbance evolves in time qualitatively as was shown in Fig. 5.3 and thus is not shown here.

On the other hand, when $\tau > \hbar/J$ the system can react to both the pressing at t_1 and the release at t_2 . In this case, two pulses are generated, one at time t_1 when the system is ‘pressed’ (perturbation is turned on) and one at t_2 when the local density perturbation is released [see Fig. 5.5].

The Fermi velocities of both pulses are set by $v_F = J$ since the arguments presented in the previous section still apply. Similarly, by changing M [see Fig. 5.6] a slight delay in the wavepacket center propagation, analogous to that observed in Fig. 5.4, is evident.

5.3 Chiral ‘edge’ dynamics in power-law traps

In this section, fermions in a Chern-band lattice in the presence of a power-law trap are considered,

$$H_0 = H_{\text{CI}} + H_{\text{trap}}, \quad (5.10a)$$

$$H_{\text{trap}} = J \sum_i \left(\frac{r_i}{r_0} \right)^\gamma c_i^\dagger c_i, \quad (5.10b)$$

where r_i is the distance of site i from the center of the trap, which in the simulations is taken to be the center of the lattice. The purpose of considering a trapped Chern lattice is to make contact to possible cold-atom realizations of such Chern lattice systems.

Cold-atom experiments are generally performed in the presence of harmonic traps, i.e., $\gamma = 2$ traps. In such a trap, it may be difficult to distinguish between edge and bulk regions. As a result there is considerable interest in power-law traps with larger exponents, i.e., large γ .

Motivated by the interest in large γ , in this section equilibrium spatial structures of fermions loaded in a $\gamma = 50$ trap are presented, and based on this knowledge the chiral responses of the ‘edges’ of such fermionic clouds to local quenches are explored.

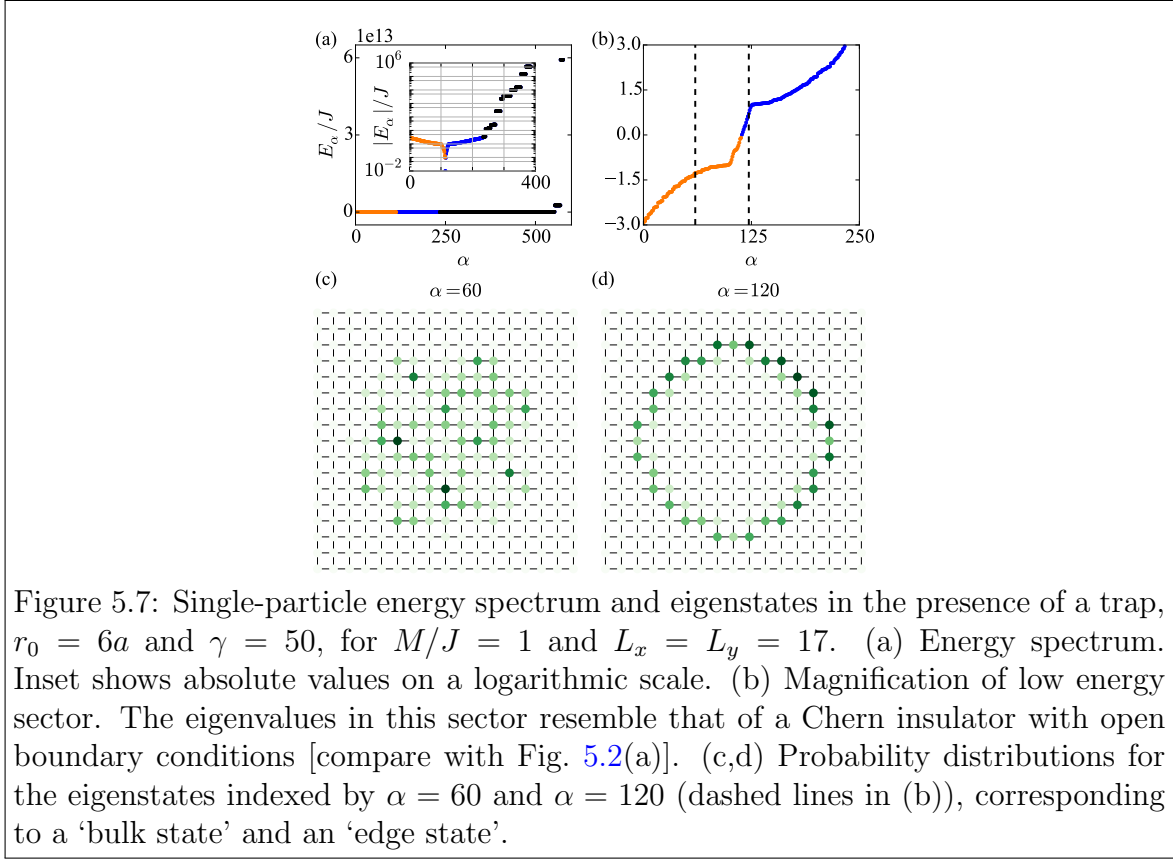


Figure 5.7: Single-particle energy spectrum and eigenstates in the presence of a trap, $r_0 = 6a$ and $\gamma = 50$, for $M/J = 1$ and $L_x = L_y = 17$. (a) Energy spectrum. Inset shows absolute values on a logarithmic scale. (b) Magnification of low energy sector. The eigenvalues in this sector resemble that of a Chern insulator with open boundary conditions [compare with Fig. 5.2(a)]. (c,d) Probability distributions for the eigenstates indexed by $\alpha = 60$ and $\alpha = 120$ (dashed lines in (b)), corresponding to a ‘bulk state’ and an ‘edge state’.

The effect of a large- γ trap is to separate energetically single-particle eigenstates which are spatially ‘inside’ the trap (within distance r_0 from the trap center) from those ‘outside’ the trap. A low-energy sector thus emerges which closely resembles a uniform system of radius r_0 . By ‘half-filling’ this region, i.e., by having $N \sim \pi r_0^2/a^2$ fermions in the entire system, one can then mimic a half-filled region with a reasonably well-defined edge. Such an ‘edge’ also shows chiral dynamics as in the open-boundary case without a trap treated in the previous section.

In Fig. 5.7, a square lattice with sides larger than $2r_0$ is used, and $\gamma = 50$. The top panels show the single-particle eigenspectrum. The higher energy sectors contain eigenstates whose weights are spatially concentrated in regions $r > r_0$. The zoom onto the low-energy sector [see top right panel in Fig. 5.7(b)] resembles the spectrum of a Chern lattice without a trap and with open boundary conditions. Indeed, eigenstates with $-1 < E/J < 1$ have an edge-like distribution localized around $r \sim r_0$, exemplified in Fig. 5.7(d). On the other hand, eigenstates with $1 < |E/J| < 3$ are extended over $r < r_0$, resembling the bulk behavior of a Chern insulator [see Fig. 5.7(c)].

Note that the midgap ‘edge’ states with $-1 < E/J < 1$ are not as sharply defined

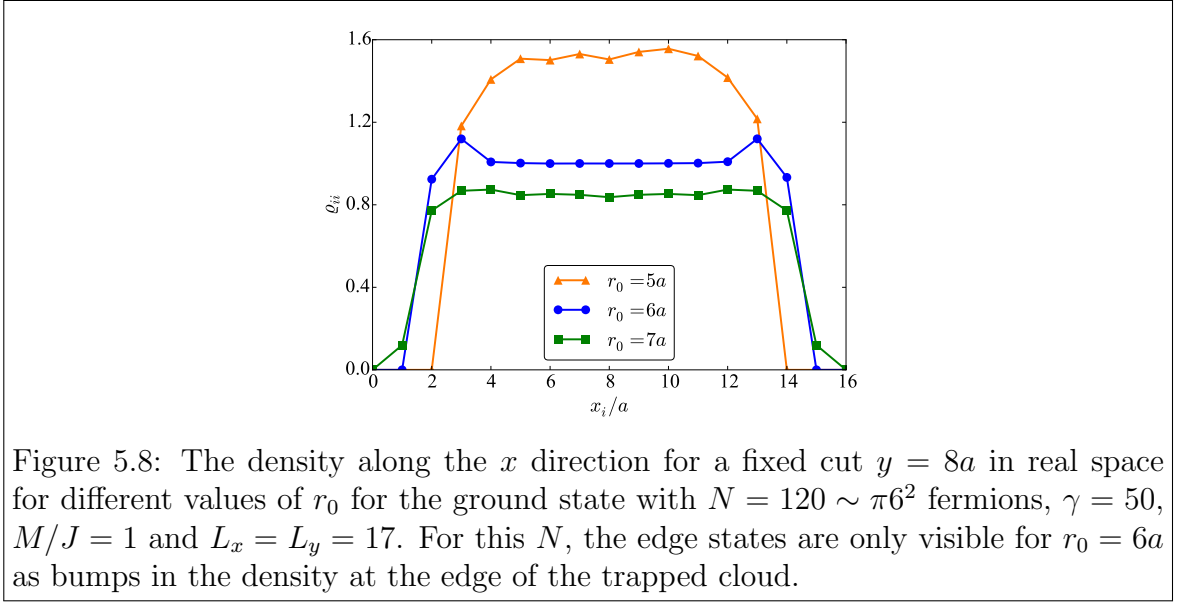


Figure 5.8: The density along the x direction for a fixed cut $y = 8a$ in real space for different values of r_0 for the ground state with $N = 120 \sim \pi 6^2$ fermions, $\gamma = 50$, $M/J = 1$ and $L_x = L_y = 17$. For this N , the edge states are only visible for $r_0 = 6a$ as bumps in the density at the edge of the trapped cloud.

as in the free Chern insulator case, as can be seen by comparing the lower panels in Fig. 5.7 with Fig. 5.2 (a). This is because, even at such large γ , the lack of a hard wall induces mixing between eigenstates with edge and bulk character. Nevertheless, the edge modes are well-defined enough to display chirality in real-time dynamics.

To access the chiral character of these effective edge states, it is necessary to mimic the situation of half-filling. This is achieved by having the fermion number to be close to $\pi r_0^2/a^2$. In Fig. 5.8, the fermion number is fixed to be $N = 120 \sim \pi 6^2 \simeq 113$, and the density profiles along the horizontal (x -) direction for traps with $r_0 = 5a$, $r_0 = 6a$, and $r_0 = 7a$ are compared. The figure shows that this particular filling provides enough fermions to occupy the effective edge states when $r_0 = 6a$. The edge occupancy is only visible in the $r_0 = 6a$ case through the bumps in the density profile peaked at $x = 3a$ and $x = 13a$; the other curves lack this feature. This exemplifies the fact that, depending on the trap shape (set by r_0), there is an optimal particle number for accessing the chiral edge states of the system.

In order to highlight the importance of the filling fraction with respect to the trap parameters, in Fig. 5.9 the real-time evolution to a perturbation at site l using the non-equilibrium protocol of Fig. 5.1(a) for $r_0 = 6a$ and $r_0 = 7a$ is shown. The particle number is fixed for both cases to be $N = 120$, the same value as in Fig. 5.7. Therefore the edge states are only populated for $r_0 = 6a$ but not for $r_0 = 7a$. For $r_0 = 6a$ (upper panels of Fig. 5.9), the perturbation follows the profile of the trap in a chiral fashion, a situation similar to a half-filled open-boundary system. For $r_0 = 7a$, the density disturbance does not propagate along the new ‘trap-induced’ edge, but

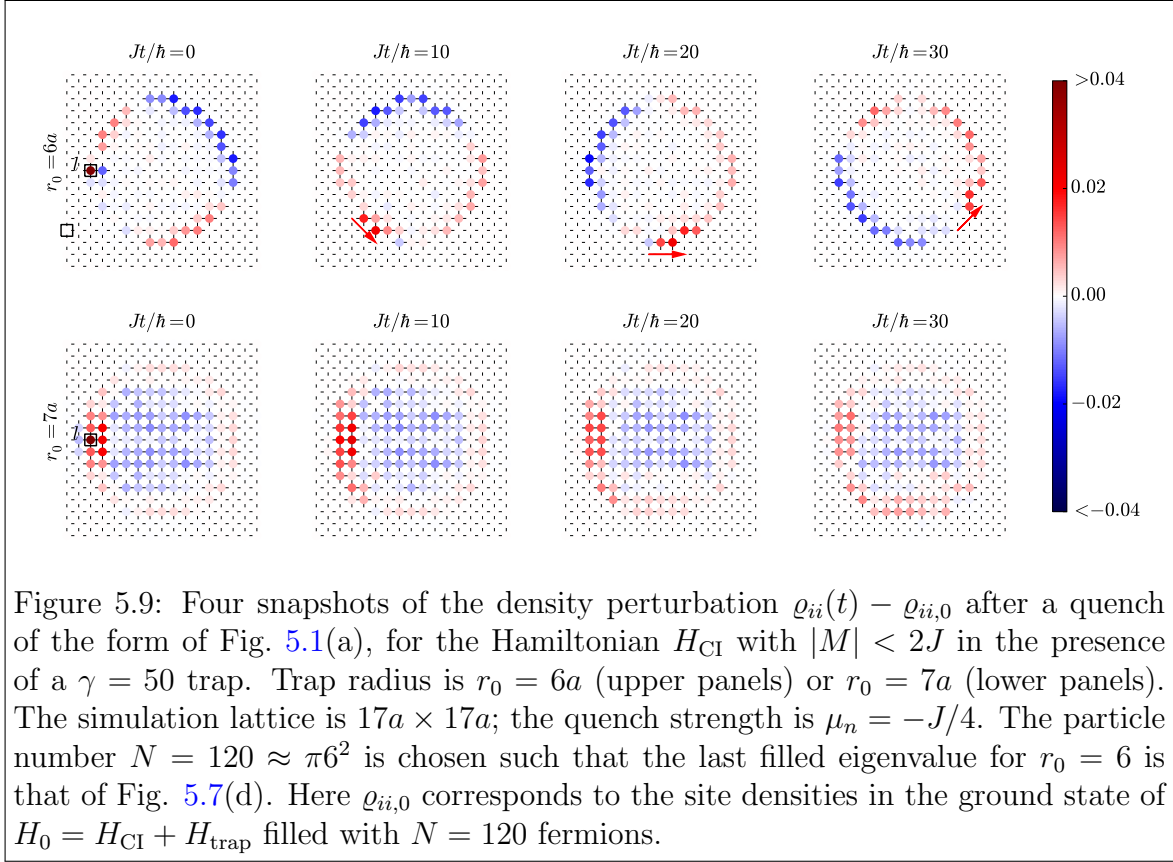


Figure 5.9: Four snapshots of the density perturbation $\varrho_{ii}(t) - \varrho_{ii,0}$ after a quench of the form of Fig. 5.1(a), for the Hamiltonian H_{CI} with $|M| < 2J$ in the presence of a $\gamma = 50$ trap. Trap radius is $r_0 = 6a$ (upper panels) or $r_0 = 7a$ (lower panels). The simulation lattice is $17a \times 17a$; the quench strength is $\mu_n = -J/4$. The particle number $N = 120 \approx \pi 6^2$ is chosen such that the last filled eigenvalue for $r_0 = 6$ is that of Fig. 5.7(d). Here $\varrho_{ii,0}$ corresponds to the site densities in the ground state of $H_0 = H_{\text{CI}} + H_{\text{trap}}$ filled with $N = 120$ fermions.

dissipates into the bulk.

Note that there is some flexibility in varying N for a fixed r_0 (and vice versa) while still obtaining a visible edge state. As long as the state at the Fermi energy is one of the edge states, the physics of edge states is accessible. The number of edge states is approximately $2\pi r_0$, the circumference of the interior region. The lattice geometry will affect the exact number, of course, but for $r_0 \gg 1$, this is a reasonable estimate. For smaller r_0 , the spectrum in Fig. 5.7 exemplifies the situation: in this case ($r_0 = 6a$), the edge states run from eigenstate $\alpha \sim 95$ to eigenstate $\alpha \sim 131$. The physics of edge states is visible as long as N is in this range.

For the $r_0 = 6a$ case, as the gap is decreased by changing the ratio M/J appropriately, the effective edge states become less localized. Fixing the rest of parameters we observe a retardation effect of the wavepacket, consistent with that discussed in Section 5.2 for the evolution in the absence of H_{trap} .

For completeness, the pulse quench protocol was also investigated under the effect of the trap and we found results similar to the scenario without a trap as long as the system is close to the optimal filling discussed above. This protocol generates two pulses confined to the boundary of the trap with similar properties as those discussed

in previous sections. Finally it is expected that the effect of softer traps, i.e. smaller values of γ , addressed for instance in [Stanescu *et al.* \(2010\)](#); [Goldman *et al.* \(2013\)](#), will result in an overall broadening of the edge states and greater mixing between bulk and edge. To what extent the chirality in real-time dynamics is visible for smaller γ remains an open question.

5.4 Summary

In this chapter, the effect of local edge quenches on the dynamics of Chern bands was investigated. Two types of local density quench protocols to probe directly the chirality of the edge states, both with and without confining traps were discussed. When the bands are topologically non-trivial, these quenches generate localized edge excitations that propagate chirally along the sample with a group velocity that decreases as the gap controlling the spatial delocalization of the edge modes decreases. In addition, it was shown that, in the presence of a sharp trap with a characteristic length scale r_0 , the chiral dynamics is only observable if the filling is such that the effective trap confinement region is half-filled. These results emphasize the importance of the effective filling within the trap to observe edge dynamics, even when the trap potential is quite sharp.

We focus on large-exponent power-law traps (large γ). While this is not the common situation in current cold-atom experiments, interest in producing and utilizing such traps is high, particularly in the context of topological matter [[Goldman *et al.* \(2013\)](#); [Dauphin and Goldman \(2013\)](#); [Gaunt *et al.* \(2013\)](#); [Meyrath *et al.* \(2005\)](#)]. The data were shown for $\gamma = 50$, but it is expected that traps with exponents down to $\gamma \approx 4$ will have similar properties [[Kolovsky *et al.* \(2014\)](#)]. By analyzing the spectrum, it was shown that the ‘inside’ and ‘outside’ of the trap are energetically separated. The ‘inside’ region is found to cover πr_0^2 lattice sites. This observation allowed for the specification of the particle number which mimics the physics of half filling in the ‘inside’ region. It was shown that the chiral dynamics is not visible when the number of fermions is very different from this optimal, because the effective filling then differs from half-filling.

It is plausible that the protocols considered in this work can be realized in cold atomic set-ups. Addressing and imaging these systems with single-site resolution have become available in cold-atom laboratories during the past few years [[Bakr *et al.* \(2010\)](#)]. Thus, performing local quenches on the recently realized Chern-band

lattices [Dauphin and Goldman (2013); Aidelsburger *et al.* (2013, 2015)] and following the ensuing site density dynamics in real time should be technologically feasible.

This might also be relevant in solid state set-ups. For instance, the Chern insulator state has been recently realized by magnetically doping a thin-film structure of a three-dimensional topological insulator [Chang *et al.* (2013)]. In this context, the protocol in Fig. 5.1(a) theoretically can be thought of as an STM tip perturbing the system locally and then releasing the state. The typical time scales governing such dynamics in this case are several orders of magnitude faster than in cold-atom experiments, rendering such a proposal practically unviable experimentally. However, fast, out-of-equilibrium photo excitation of electrons has been measured with recent pump-probe techniques [Wang *et al.* (2013)]. In this experiment, the local dynamics occurring within typical electron timescales of femtoseconds were measured at the surface of a three-dimensional topological insulator. In light of these results one can reinterpret the protocol in Fig. 5.1(b) in a first approximation as a laser pulse of duration τ that probes the electrons locally in space and time. It is therefore not unrealistic to think that implementing such a protocol might be possible by probing the Chern insulator state of Chang *et al.* (2013), especially considering that the Chern insulators are grown from essentially the same family of materials that were pump-probed [Wang *et al.* (2013)].

Chapter 6

Chern numbers and chiral anomalies in Weyl butterflies

The semiclassical framework introduced in Chapter 2 is now used in this chapter to study an exotic class of three-dimensional systems, namely Weyl semimetals [Hosur and Qi (2013); Vafeek and Vishwanath (2014)]. These semimetals host pairs of protected band touchings (nodes) that disperse linearly with momentum. Each pair is composed of a left and right chirality node, a quantum number resembling the valley degree of freedom in graphene. As discussed in Chapter 2, Weyl nodes are sources or sinks of Berry flux denoted by their chirality, *i.e.*

$$\eta = \pm 1 = \frac{1}{4\pi} \oint_S d\mathbf{s} \cdot \boldsymbol{\Omega}(\mathbf{k}_s), \quad (6.1)$$

where the Berry curvature is integrated over a closed surface in momentum space enclosing the Weyl node. η being ± 1 corresponds to the left and right chirality of the Weyl nodes. The underlying topology of the energy bands on these semimetals, encoded in the chiralities and locations of Weyl points leads to interesting electromagnetic responses [Hosur *et al.* (2012); Landsteiner (2014)]. For instance, although the sum of right- and left-chiral fermions is conserved, non-orthogonal magnetic (\mathbf{B}) and electric (\mathbf{E}) fields pump one chirality to the other at a rate $\propto \mathbf{E} \cdot \mathbf{B}$, so that their difference is not conserved. This phenomenon, known as the chiral anomaly [Bertlmann (2000); Nielsen and Ninomiya (1983)] is actually one of the defining characteristics of Weyl semimetals which manifests itself as negative magnetoresistance [Son and Spivak (2013); Burkov (2015)], and the chiral magnetic effect [Goswami and Tewari (2013b); Kharzeev (2014)]. The response of Weyl fermions to external electromagnetic fields is well understood both in the linear response regime [Volovik (2003); Burkov and Balents (2011); Zyuzin *et al.* (2012); Aji (2012); Grushin (2012); Liu *et al.* (2013); Goswami and Tewari (2013a); Landsteiner (2014)] and the Landau level limit [Nielsen

and Ninomiya (1983); Goswami and Tewari (2013a); Klier *et al.* (2015); Bulmash and Qi (2016); Ominato and Koshino (2016)]. The equation of continuity satisfied by the chiral charge and the chiral current (the difference of the charges and currents for the two kinds of fermions corresponding to different chiralities) is

$$\sum_{\mu=0}^3 \partial_{\mu} j_5^{\mu} = \frac{2e^2}{h^2 c} \mathbf{E} \cdot \mathbf{B}, \quad (6.2)$$

where $j_5 = (j_5^0, \mathbf{j}_5)$ is four-vector with the time-like component j_5^0 denoting the chiral charge and the space-like component \mathbf{j}_5 denoting the current. The convention of using j_5 to denote the chiral current is borrowed from the fact that traditionally in relativistic field theories, the chirality operator is denoted by γ_5 . However, as is often the case in physics with competing physical effects on comparable length scales, the fate of the chiral anomaly takes a much more interesting turn in the presence of large magnetic fields, specifically in the Hofstadter limit, *i.e.*, when the magnetic length l_B becomes comparable to the lattice spacing a [Hofstadter (1976)]. The non-renormalization theorem of the chiral anomaly beyond one loop [Bertlmann (2000)] breaks down, and the \mathbf{B} -dependence of the anomaly is periodic in units of the flux quantum, Φ_0 per unit cell.

Hence, the focus of this chapter is to understand the topology of the spectrum of Weyl a semimetal in the presence of large magnetic fields, dynamically probe the spectrum using wavepacket dynamics analyzed using semiclassical equations of motion, and study the resulting chiral anomaly. It is found that the chiral anomaly tracked through the rate of chiral charge pumping shows a fractal of linear regimes proportional to \mathbf{B} with quantized integer slopes, intimately connected to a fractal set of emergent Weyl nodes at commensurate fluxes. The integer slopes are given by the Chern numbers of the Weyl butterfly – a three-dimensional fractal which describes the spectrum of a Weyl semimetal under large magnetic fluxes. The physics resulting from the third dimension is not a mere generalization of the two-dimensional Hofstadter case. In fact, the Weyl butterfly can be thought of as a collection of 2D Hofstadter butterflies as a function of the third momentum. Crucially, there is an analytical connection between the evolution of the fractal spectrum along the third momentum direction, its Chern numbers, and the fractal nature of the chiral anomaly.

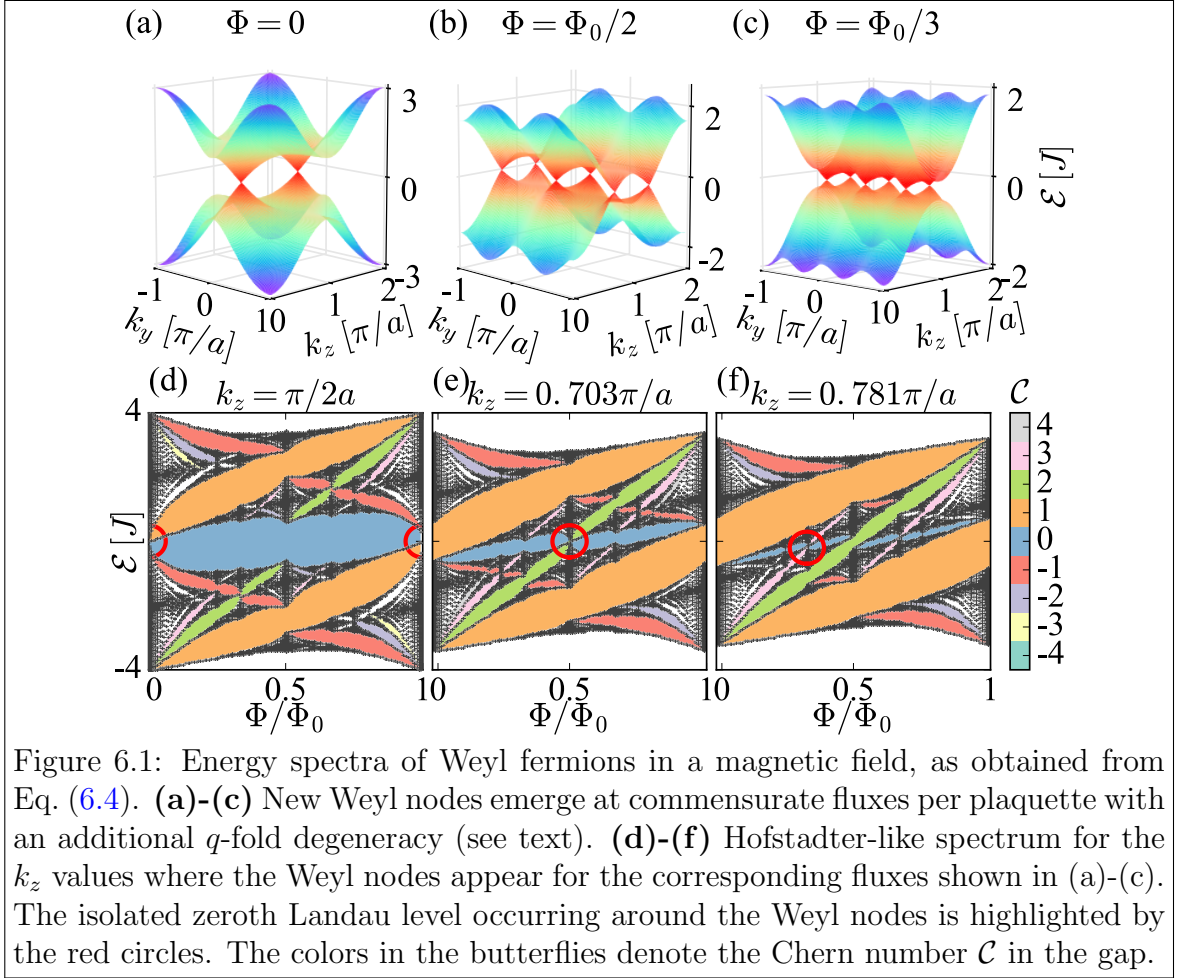


Figure 6.1: Energy spectra of Weyl fermions in a magnetic field, as obtained from Eq. (6.4). (a)-(c) New Weyl nodes emerge at commensurate fluxes per plaquette with an additional q -fold degeneracy (see text). (d)-(f) Hofstadter-like spectrum for the k_z values where the Weyl nodes appear for the corresponding fluxes shown in (a)-(c). The isolated zeroth Landau level occurring around the Weyl nodes is highlighted by the red circles. The colors in the butterflies denote the Chern number \mathcal{C} in the gap.

6.1 Weyl semimetal in magnetic fields

To describe a Weyl semimetal, the two-band Hamiltonian of spinless fermions on a cubic lattice $\mathcal{H}_{\mathbf{k}} = \mathbf{d}_{\mathbf{k}} \cdot \boldsymbol{\sigma}$ (introduced in Chapter 2 in Eq. (2.13)) is employed, with

$$\mathbf{d}_{\mathbf{k}} = -\{J_2 \sin k_x, J_2 \sin k_y, -M + J_1 \sum_{i=x,y,z} \cos k_i\}. \quad (6.3)$$

This model breaks time-reversal symmetry and is motivated by the model proposed in Dubček *et al.* (2015), which is composed of the two time-reversal partners of Eq. (6.3) separated in momentum space. It has a pair of linearly dispersing Weyl cones at $\mathbf{k} = \{0, 0, \pm \cos^{-1}(M/J_1 - 2)\}$ for $1 < |M/J_1| < 3$. For the remainder of the chapter, $J_2 = J_1 = J$ and $M/J = 2$. Figure 6.1(a) shows the band structure in the (k_y, k_z) plane. This model is constructed from Chern insulators in the (k_x, k_y) plane with a k_z dependent gap such that the Chern number \mathcal{C}_{k_z} changes whenever a Weyl node is crossed, as shown by the dashed line in Figure 6.2(b).

Consider applying magnetic field $\mathbf{B} \parallel \hat{z}$ with flux $\Phi = \Phi_0 p/q$ per plaquette, equivalent to an Aharonov-Bohm phase of $\phi = 2\pi p/q$ upon tunneling around a plaquette. In the Landau gauge, $\mathbf{A} = \Phi x \hat{y}$, the Hamiltonian becomes

$$\mathcal{H}_{\mathcal{WH}} = \begin{pmatrix} \mathcal{M}_1 & \mathcal{R}/2 & 0 & \cdots & \mathcal{S}/2 \\ \mathcal{R}^\dagger/2 & \mathcal{M}_2 & \mathcal{R}/2 & \cdots & 0 \\ \vdots & \ddots & \ddots & \ddots & \vdots \\ \mathcal{S}^\dagger/2 & 0 & \cdots & \mathcal{R}^\dagger/2 & \mathcal{M}_q \end{pmatrix},$$

where,

$$\begin{aligned} \mathcal{M}_n(k_y, k_z) &= [M - J(\cos(k_y + \phi n) + \cos k_z)]\sigma^z - J \sin(k_y + \phi n)\sigma^y, \\ \mathcal{R} &= -J(\sigma^z - i\sigma^x); \quad \mathcal{S}(k_x) = -J(\sigma^z + i\sigma^x)e^{-ik_x}, \end{aligned} \quad (6.4)$$

and the subscript \mathcal{WH} stands for Weyl-Hofstadter. Each k_z exhibits a Hofstadter-like spectrum [Araújo and Castro (2014)], (see Figure 6.1) forming the energy spectrum that we refer to as the Weyl butterfly.

One unexpected aspect of the Weyl butterfly is that, for commensurate fluxes, new pairs of Weyl nodes emerge with q -fold degeneracy unlike the two-dimensional Hofstadter butterfly which has Dirac nodes only for even q . By inspection of the spectrum it seems likely that given a commensurate value of $\Phi/\Phi_0 = p/q$ there is a particular value of k_z where q Weyl nodes appear somewhere in the spectrum (not necessarily at zero energy). Unfortunately rigorous proof is still elusive although heuristic arguments can be made to support the conjecture as follows: Start by noting that the effective two-dimensional Hamiltonian obtained by considering the Weyl semimetal Hamiltonian (6.3) at a fixed k_z slice can be decomposed into three kinds of terms, the intra-sublattice hoppings (J_1), the inter-sublattice hoppings (J_2), and a staggered chemical potential $M_{\text{eff}} = M - J_1 \cos k_z$. For $J_2=0$, the Hamiltonian represents two decoupled square lattices; the spectra of each of these copies are shifted in energy by $\pm M_{\text{eff}}$.

It was shown by Wen and Zee [Wen and Zee (1989)] that the single-particle spectrum of fermions hopping on a square lattice with a magnetic flux Φ per plaquette has at least q isolated nodes at zero energy for q even. This implies that the spectrum of Hamiltonian Eq. (6.3) at a fixed k_z and $J_2 = 0$ has $2q$ nodes (q nodes per sublattice) with q of them located at $\mathcal{E} = M_{\text{eff}}$ and q of them at $\mathcal{E} = -M_{\text{eff}}$, where \mathcal{E} denotes their energies. However, a $J_2 \neq 0$ induces a mixing between the spectra of the two sublattices making the q pairs of nodes gapped. Such inter-sublattice hopping is analogous to a Haldane-like topological gap [Haldane (1988)] effectively breaking time-reversal symmetry. As long as the two competing gaps, due to M_{eff} and J_2 ,

are of the same order, the spectrum can be fine-tuned by varying k_z to find gapless nodes in the spectrum. The periodicity of the Brillouin zone ensures that there are q of them and since the spectrum depends on k_z via $\cos(k_z)$, the spectra at $\pm k_z$ are identical thus resulting in q pairs of nodes.

Figure 6.1(d)-(f) highlights some of the emergent Weyl nodes that cross near $\mathcal{E} = 0$ for particular values of k_z . The emergence of such new Weyl nodes is related to the fractal structure of the butterfly, while the q -fold degeneracy comes from noting that the shift $k_y \rightarrow k_y + 2\pi p/q$ in Eq. (6.4) amounts to changing \mathbf{A} in steps of Φ , which has no effect on the spectrum. Since q such translations traverse the BZ, there should be q copies of the spectrum.¹ Perturbing the flux around one of these emergent Weyl nodes splits it into Landau levels dispersing along k_z , including a chiral zeroth Landau level [Nielsen and Ninomiya (1983)]. As the flux is further increased, the Landau levels split and merge with those of the upcoming Weyl node, a feature which is explored in more detail later.

6.2 Chern numbers via wavepacket dynamics

A non-trivial topological invariant that characterizes the emergent Weyl nodes at rational flux is the Chern number in each momentum plane. An experimentally feasible probe of this invariant in cold-atomic systems is the semi-classical motion of wavepackets [Dauphin and Goldman (2013); Li *et al.* (2016)], which has successfully been used in both the two-dimensional Hofstadter [Aidelsburger *et al.* (2015)] and Haldane [Jotzu *et al.* (2014)] models. The principle (for details, refer to Chapter 2, Section 2.2) is that, under an external force, wavepackets Hall drift transverse to the direction of the force with amplitude proportional to the Chern number.

Such Hall-like response can be used to characterize the Weyl butterfly.

6.2.1 Wavepackets localized in momentum

First, we consider preparing a wavepacket sharply peaked around a finite momentum k_z along the axis of Weyl node separation. Such a wavepacket could be achieved experimentally by initially decreasing the lattice depth along the z -direction to create a sharp k_z peak then taking it to the desired k_z via a ramped magnetic field [Greiner *et al.* (2002)] or optical gradient [Aidelsburger *et al.* (2015)], lattice acceleration [Ben Dahan *et al.* (1996)], or Bragg pulse [Ernst *et al.* (2010)]. Then consider a wavepacket

¹More generally, the degeneracy will be some multiple nq of q for integer values of n , as we know that if n Weyl pairs exist, then we can create nq copies by shifting k_y . For all the cases considered in this chapter, $n = 1$.

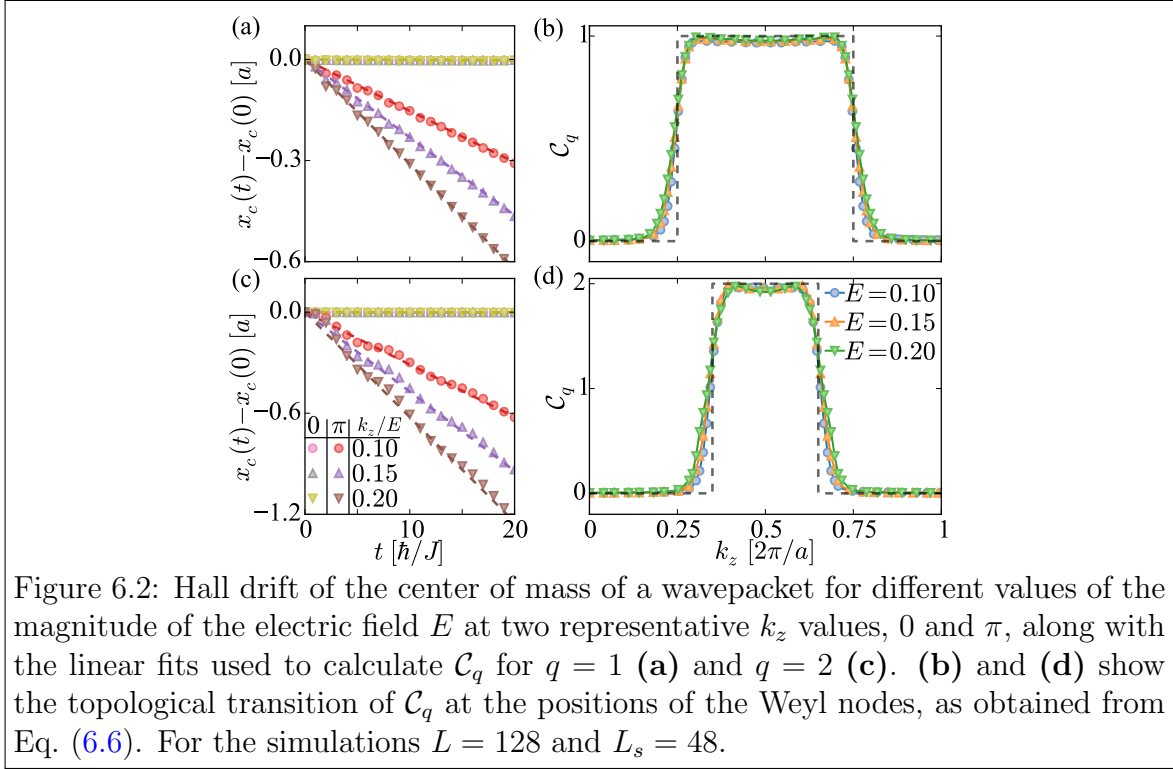


Figure 6.2: Hall drift of the center of mass of a wavepacket for different values of the magnitude of the electric field E at two representative k_z values, 0 and π , along with the linear fits used to calculate \mathcal{C}_q for $q = 1$ (a) and $q = 2$ (c). (b) and (d) show the topological transition of \mathcal{C}_q at the positions of the Weyl nodes, as obtained from Eq. (6.6). For the simulations $L = 128$ and $L_s = 48$.

initially confined within a $L_s \times L_s$ sub-region of an $L \times L$ lattice ($L_s < L$) in the (x, y) plane [Dauphin and Goldman (2013)]. At $t = 0$, the xy -confinement is removed to give approximately uniformly filled bands² in (k_x, k_y) , and a constant force $\mathbf{F} = EJ/a \hat{y}$ is applied [Aidelsburger *et al.* (2015); Greiner *et al.* (2002); Ben Dahan *et al.* (1996)]. The center-of-mass motion in the n^{th} band is governed by the semiclassical equations of motion [Xiao *et al.* (2010)]

$$\dot{\mathbf{r}}_c = \nabla_{\mathbf{k}} \mathcal{E}_{n,\mathbf{k}} + \dot{\mathbf{k}} \times \boldsymbol{\Omega}_{n,\mathbf{k}}; \quad \dot{\mathbf{k}} = \mathbf{F}; \quad (6.5)$$

where $\mathcal{E}_{n,\mathbf{k}}$ and $\boldsymbol{\Omega}_{n,\mathbf{k}}$ are, respectively, the energy dispersion and Berry curvature of the band, and the subscript c in \mathbf{r}_c denotes it is the position of the center of mass of the wavepacket. The net drift of the many-fermion wavepacket can be obtained by integrating Eq. (6.5) over time and summing over the responses for all the filled bands. For q uniformly filled bands, the drift is [Dauphin and Goldman (2013)]

$$\mathbf{r}_c(t) - \mathbf{r}_c(0) = -\frac{Et}{2\pi} \sum_{n=1}^q \mathcal{C}_n \hat{x} \equiv -\frac{Et}{2\pi} \mathcal{C}_q \hat{x}, \quad (6.6)$$

²A uniform population of the band is expected if the hierarchy of energy scales $\Delta \gg k_B T \gg W$ is satisfied, where W is the bandwidth, Δ is the band gap, and $k_B T$ is the temperature energy scale. This criterion is satisfied for high flatness ratios, which have been demonstrated in the experiment in Aidelsburger *et al.* (2015).

where $\mathcal{C}_n = (1/2\pi) \int dk_x dk_y \Omega_{n,\mathbf{k}}^z$ is the Chern number of the n^{th} band.

For flux Φ , we can use this technique to measure the sum of the Chern numbers of the q lowest bands, \mathcal{C}_q , for emergent Weyl nodes which connect the q^{th} and $(q+1)^{\text{th}}$ bands. The Hall drift given by Eq. (6.6), and its corresponding \mathcal{C}_q are shown in Figure 6.2 for two different fluxes as a function of k_z . As k_z crosses a Weyl node, the q^{th} and $(q+1)^{\text{th}}$ bands undergo a topological phase transition where the sign of the gap of the Chern insulator flips. Consequently, since there are q such Weyl points, the Chern number changes by $\pm q$ with sign determined by the chirality of the Weyl nodes. Thus from the wavepacket dynamics as a function of k_z , one can extract the location, chiralities, and multiplicities of the Weyl points.

6.2.2 Wavepackets with finite momentum spread

In experiments, it is often easier to prepare a finite-width distribution of the occupations W_{k_z} than a sharply-peaked k_z . Controlling the width of this distribution through external trapping or temperature also allows to infer information about the spectrum. In this case, the Hall drift with the Fermi level in the q^{th} gap yields a non-quantized effective Chern number, $\mathcal{C}_{q,\text{eff}} = \sum_{k_z} \mathcal{C}_{q,k_z} W_{k_z}$, which is the average of \mathcal{C}_{q,k_z} weighted by W_{k_z} . For instance, if Gaussian distributions are created centered at $k_z = 0$ with width σ for the particular case of two Weyl nodes at $\pm K_0/2$, the dependence of the Hall drift on σ saturates to $\mathcal{C}_{q,\text{eff}} = \mathcal{C}_{q,k_z=\pi/a} - (\mathcal{C}_{q,k_z=\pi/a} - \mathcal{C}_{q,k_z=0})K_0/2\pi$ in the $\sigma \rightarrow \infty$ limit and to $\mathcal{C}_{q,\text{eff}} = \mathcal{C}_{q,k_z=0}$ for $\sigma \rightarrow 0$. Varying σ interpolates between these limits; a simple fit can then extract the Chern number profile. The following illustrates how tuning the spread of wavepackets without changing the average momentum can be used to reconstruct the Chern number profile. In particular, by tuning parameters such as temperature, density, trapping profile, and lattice depth [Anderson *et al.* (1995); Davis *et al.* (1995); Bradley *et al.* (1995); Greiner *et al.* (2002, 2003); Regal *et al.* (2004); Jochim *et al.* (2003); Zwierlein *et al.* (2003); Bloch *et al.* (2008)], cold-atom experiments routinely realize a wide variety of momentum-space distributions. Furthermore, the distribution can not only be tuned via experimentally accessible parameters, but measured with high accuracy in time of flight. As discussed above, this tunability of the momentum profile in the z -direction can be directly used to measure the Chern number profile as a function of k_z , for which a particular example is now discussed.

To model a wavepacket with finite momentum spread, pick the simplest case of a

Gaussian profile centered around $k_z = 0$ with width σ

$$W(k_z) = \frac{1}{\sqrt{2\pi}\sigma} \frac{e^{-k_z^2/2\sigma^2}}{\text{Erf}(\pi/\sqrt{2}\sigma)}, \quad (6.7)$$

where the error function (Erf) results from normalizing the Gaussian distribution over the compact Brillouin zone. The Hall drift in the (x, y) plane would then yield the non-quantized effective Chern number

$$\mathcal{C}_{\text{eff}} = \sum_{k_z=-\pi}^{\pi} W(k_z) \mathcal{C}_{k_z}. \quad (6.8)$$

Consider the case as in our model of the Weyl semimetal where (possibly degenerate) Weyl nodes occur at $k_z = \pm K_0/2$. The Chern number profile follows $\mathcal{C}_{k_z} = \mathcal{C}_{k_z=0}$ for $|k_z| < K_0/2$, and $\mathcal{C}_{k_z} = \mathcal{C}_{k_z=\pi}$ otherwise (cf. Figure 6.2). Hence, the problem has now been reduced to inferring three quantities, namely K_0 , $\mathcal{C}_{k_z=0}$ and $\mathcal{C}_{k_z=\pi}$, from measurements of \mathcal{C}_{eff} for various values of σ .

Taking a wavepacket that is well localized near $k_z = 0$ such as a Bose-Einstein condensate [Anderson *et al.* (1995); Davis *et al.* (1995); Bradley *et al.* (1995)] corresponds to $\sigma \approx 0$. Inspection of Eqs. (6.7) and (6.8), trivially reveals that $\mathcal{C}_{\text{eff}}(\sigma = 0) = \mathcal{C}_{k_z=0}$. Hence, the Hall drift with a wavepacket localized in k_z would yield $\mathcal{C}_{k_z=0}$, one of the three quantities of interest.

The other extreme limit, a ‘‘high-temperature’’ wavepacket completely delocalized in k_z (while remaining in the lowest band) has uniform distribution $W(k_z) = 1/2\pi$. In this limit, \mathcal{C}_{eff} would saturate to

$$\mathcal{C}_{\text{sat}} = \mathcal{C}_{k_z=\pi} - (\mathcal{C}_{k_z=\pi} - \mathcal{C}_{k_z=0})K_0/2\pi. \quad (6.9)$$

\mathcal{C}_{sat} relates the remaining two quantities of interest, K_0 and $\mathcal{C}_{k_z=\pi}$.

The behavior of \mathcal{C}_{eff} as a function of the width of the wavepacket between these two limits is shown in Figure 6.3. For small σ there is flat plateau at $\mathcal{C}_{k_z=0}$ as the wavepacket has all its weight in the $\mathcal{C}_{k_z} = \mathcal{C}_{k_z=0}$ region of the Brillouin zone for $\sigma \ll K_0$. Beyond this threshold, the tails of Gaussian (6.7) pick up contributions from the $\mathcal{C}_{k_z} = \mathcal{C}_{k_z=\pi}$ region and \mathcal{C}_{eff} deviates from the plateau. Therefore, the length of this plateau is directly related to the separation of the Weyl nodes, K_0 . To determine this quantity it is useful to define empirically

$$|\mathcal{C}_{\text{eff}}(\sigma_\Lambda) - \mathcal{C}_{k_z=0}| = \Lambda, \quad (6.10)$$

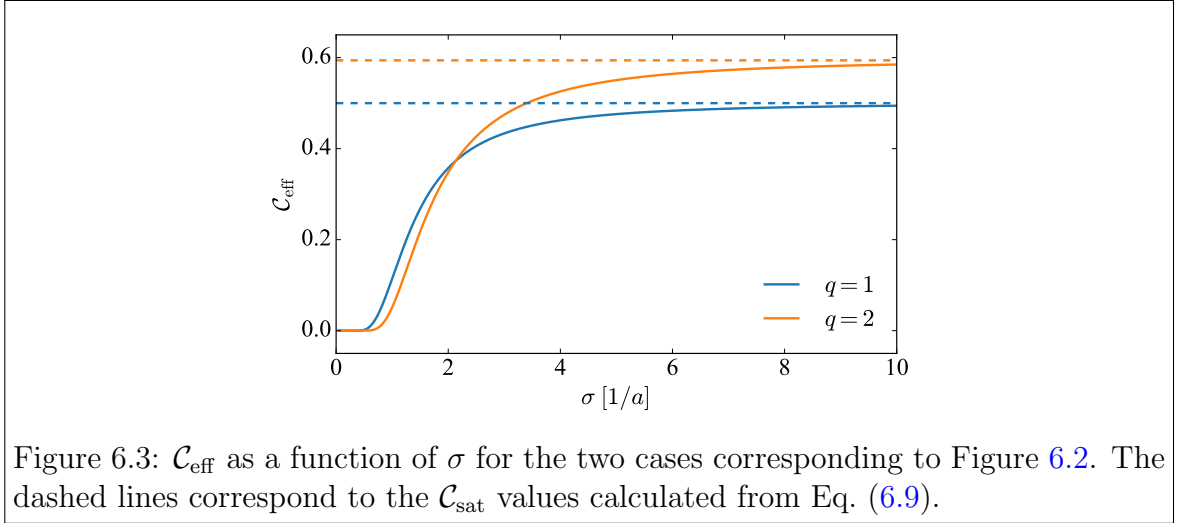


Figure 6.3: \mathcal{C}_{eff} as a function of σ for the two cases corresponding to Figure 6.2. The dashed lines correspond to the \mathcal{C}_{sat} values calculated from Eq. (6.9).

where $\Lambda \ll |\mathcal{C}_{k_z=0} - \mathcal{C}_{k_z=\pi}|$, and σ_Λ is the empirical length of the plateau. Using the asymptotic properties of the error function, Eq. (6.10) can be expressed as

$$\frac{2\sqrt{2}\sigma_\Lambda}{K_0} e^{-K_0^2/8\sigma_\Lambda^2} = \Lambda |\mathcal{C}_{k_z=\pi} - \mathcal{C}_{k_z=0}|, \quad (6.11)$$

which can further simplified using Eq. (6.9) to

$$\frac{2\sqrt{2}\sigma_\Lambda}{K_0} \left(1 - \frac{K_0}{2\pi}\right) e^{-K_0^2/8\sigma_\Lambda^2} = \Lambda |\mathcal{C}_{\text{sat}} - \mathcal{C}_{k_z=0}|. \quad (6.12)$$

Note that \mathcal{C}_{sat} and $\mathcal{C}_{k_z=0}$ are experimentally accessible quantities and σ_Λ is an empirically chosen quantity. Hence, solving the transcendental equation (6.12) the value of K_0 can be obtained and used in Eq. (6.9) to obtain $\mathcal{C}_{k_z=\pi}$. One may also perform a simple three-parameter fit given the measured profile $W(k_z)$ and obtain these parameters without any further analytical insight.

Therefore, it has been shown that from experimentally realistic procedures it is indeed possible to reconstruct the Chern number profile of a Weyl semimetal. Note that in the absence of interactions these topological properties of the band structure are in principle equally accessible via bosons or fermions. Indeed, condensation has recently been measured in a two-dimensional Hofstadter model that can be thought of as a precursor to the Weyl semimetal [Kennedy *et al.* (2015)]. Combined with wave packet measurements of Hall drift and Chern number that have been demonstrated in similar two-dimensional models [Aidelsburger *et al.* (2015); Jotzu *et al.* (2014)], these ideas for probing the topological physics of the Weyl semimetal is well within the reach of current technology.

6.3 Chiral anomalies in the Weyl butterfly

This section discusses the central focus of this chapter; the fate of the chiral anomaly in the Hofstadter regime. The starting point is Eq. (6.3) at $\Phi = 0$ with chemical potential chosen to be at the Weyl nodes ($\mathcal{E}_F = 0$). Upon applying a finite flux ($\Phi/\Phi_0 \lesssim 1/4$) the spectrum first breaks into Landau levels (cf. Figure 6.4a) that disperse with k_z . Due to the chiral anomaly, if an additional electric field is applied at $t = 0$ satisfying $\mathbf{E} \parallel \hat{z}$, we expect the occupancies to shift along k_z turning left-handed into right-handed fermions via the bottom of the band. To characterize the chiral anomaly, define the chiral charge density

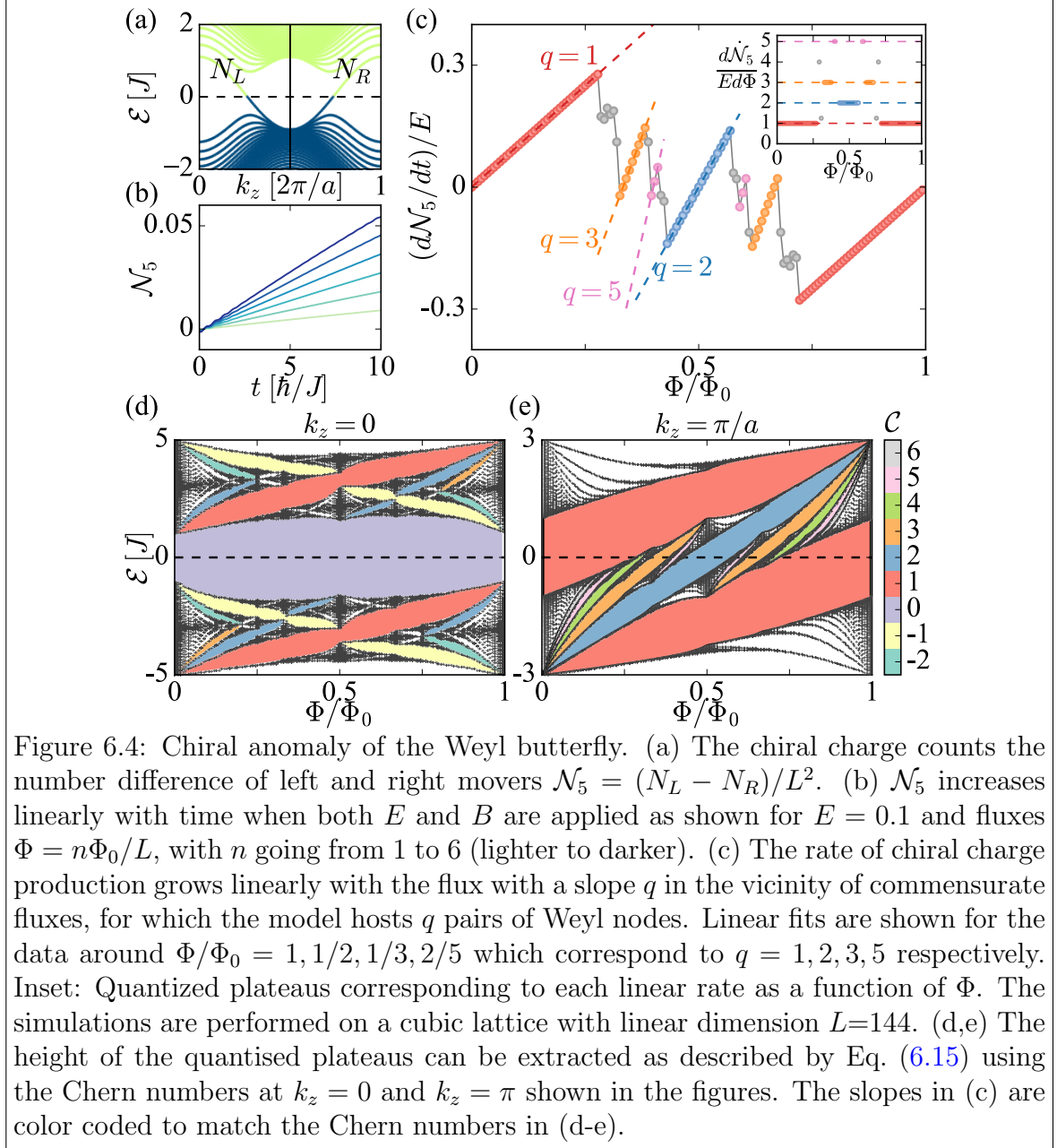
$$\mathcal{N}_5 = \left(\frac{1}{L^2} \right) \sum_{k_y=0}^{2\pi/a} \left[\sum_{k_z=0}^{\pi/a} n_{k_y, k_z} - \sum_{k_z=\pi/a}^{2\pi/a} n_{k_y, k_z} \right], \quad (6.13)$$

where n_{k_y, k_z} is the total number of filled fermionic states with momentum k_y, k_z . This quantity monitors the amount of charge pumped from one half of the Brillouin zone to another; its rate of increase is proportional to the applied electric field. The definition (6.13) implies that only the states that cross the Fermi level can contribute to the pumping of chiral charge. For $\Phi/\Phi_0 \lesssim 1/4$ it is found that \mathcal{N}_5 grows linearly with time (Figure 6.4b). In addition, the rate of growth $d\mathcal{N}_5/Edt$ is linear as a function of Φ (Figure 6.4c). So far, both of these results are consistent with the conventional chiral anomaly, $d\mathcal{N}_5/dt \propto \mathbf{E} \cdot \mathbf{B}$.

As the flux is increased ($\Phi/\Phi_0 > 1/4$) the linear behavior of $d\mathcal{N}_5/Edt$ with Φ breaks down. As shown in Figure 6.4c, several linear regimes where $d\mathcal{N}_5/dt \propto \Phi$ appear, with unequal slopes. Each linear regime is centered around commensurate fluxes $\Phi/\Phi_0 = p/q$, with slope quantized to q . This is a direct consequence of the emergence of q pairs of Weyl nodes, leading to q copies of the Landau levels crossing the Fermi energy. Hence, as the flux is ramped, the Landau level degeneracy grows as $q\Delta\Phi$, leading to chiral charge production $d\mathcal{N}_5/dt \propto Eq\Delta\Phi$. The full behaviour is thus composed of jumps between the linear regimes in Figure 6.4 around commensurate values of the flux.

In the thermodynamic limit, the self-similar fractal structure of the butterfly implies that these linear regimes should themselves form a fractal of integer-valued slopes.

In order to establish a more physical understanding of the fractal nature of the anomaly it can be connected to the Chern number in the gaps of Weyl butterfly. Recall first that the rate of chiral charge pumping $(d\mathcal{N}_5/dt)/E$ counts the number of



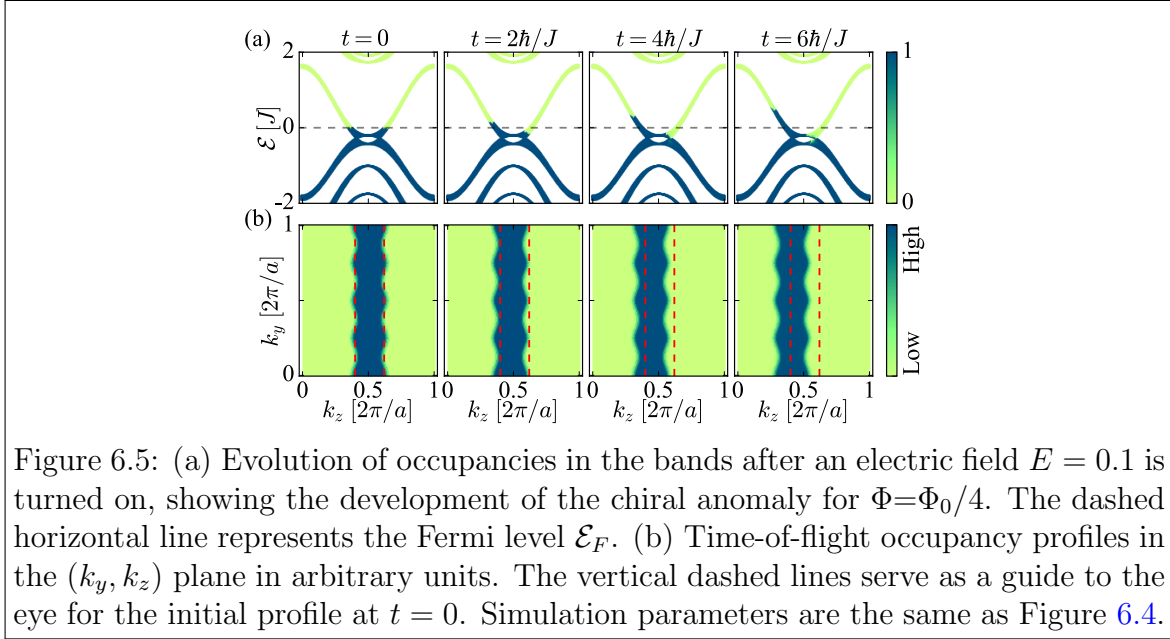


Figure 6.5: (a) Evolution of occupancies in the bands after an electric field $E = 0.1$ is turned on, showing the development of the chiral anomaly for $\Phi = \Phi_0/4$. The dashed horizontal line represents the Fermi level \mathcal{E}_F . (b) Time-of-flight occupancy profiles in the (k_y, k_z) plane in arbitrary units. The vertical dashed lines serve as a guide to the eye for the initial profile at $t = 0$. Simulation parameters are the same as Figure 6.4.

chiral channels at the Fermi level. Second, it is emphasized that the Weyl butterfly has, for fixed k_z , a series of gaps at $\mathcal{E}_F = 0$ (cf. Figure 6.4(d)-(e)), each characterized by its Chern number \mathcal{C}_{k_z} . The Chern number determines how density is modified when applying a magnetic field through the Streda formula [Streda (1982)]

$$d\rho_{2D}^{k_z}/dB_z = \mathcal{C}_{k_z}|_{\mathcal{E}_F=0}/\Phi_0 . \quad (6.14)$$

Consider adding one flux quantum to the system $\Phi = \Phi_0/L^2$. For $k_z = 0$, $\mathcal{C} = 0$ at $\mathcal{E}_F = 0$, so the density is unaffected. For $k_z = \pi/a$, $\mathcal{C} = 1$, so to increase ρ_{2D} as in Eq. (6.14), one conduction level must move to the valence band. The difference must be accommodated between these momenta, leading to one extra chiral channel. Since, for our inversion-symmetric Weyl semimetal, the Weyl points always appear in $\pm k_z$ pairs with opposite chirality, it suffices to consider $k_z = 0, \pi/a$. This predicts that the chiral anomaly generalizes to

$$(1/E)d\dot{\mathcal{N}}_5/d\Phi = \mathcal{C}_{k_z=\pi/a} - \mathcal{C}_{k_z=0} , \quad (6.15)$$

which is confirmed in Figure 6.4(c)-(e). Furthermore, since the butterfly at $k_z = \pi/a$ consists of a fractal set of gapped Chern insulators, we see that the anomaly will become a fractal set of linear anomalies with quantized slopes in the thermodynamic limit. Eq. (6.15) succinctly summarizes the main results of this chapter. It highlights the topological connection between different k_z sectors which determine the quantized slopes of the chiral anomaly, a result only possible in three dimensions.

The experimental prospects to probe the chiral anomaly are now discussed. Lack of reservoirs and relaxation make transport measurements difficult, but this also helps to distinguish the chiral anomaly in cold atoms from other competing effects. In practice, the most direct probe is time of flight, which directly maps out the momentum-space occupancies [Bloch *et al.* (2008)]. Figure 6.5(a) and Figure 6.5(b) shows the calculated occupancies and time-of-flight images for $\Phi/\Phi_0 = 1/4$ upon applying $\mathbf{E} \parallel \mathbf{B}$ at $t = 0$. The pumping rate $\dot{\mathcal{N}}_5$ can be monitored to probe the chiral anomaly and experimentally access the observables in Figure 6.4.

The analysis extends to models without inversion symmetry, which may have multiple pairs of Weyl nodes. In particular, time-of-flight measurements could track each pair of Weyl nodes independently to measure the chiral pumping. The results can thus be experimentally tested using existing technology in realistic models such as that in Dubček *et al.* (2015), which already incorporates the high magnetic field necessary for the Weyl butterfly, or the three dimensional variant [Wang and Liu (2016)] of the model proposed in Liu *et al.* (2014).

6.4 Summary

It was shown that the chiral anomaly generalizes to a quantized fractal in the high-magnetic-field limit, connecting the longitudinal chiral anomaly response to the transverse Hall response characterized by the Chern number. The results hold for any model of Weyl semimetal with inversion symmetry. The evolution of the spectral butterfly in the third momentum direction determines the universal three-dimensional physics of the chiral anomaly which is summarized by Eq. (6.15). This particular interplay between two-dimensional planes and the emergence of Weyl nodes for all q distinguishes the Weyl butterfly from two-dimensional [Hofstadter (1976)], and three-dimensional variants of the Hofstadter problem [Kohmoto *et al.* (1992); Hasegawa (1992); Koshino *et al.* (2001, 2002); Goryo and Kohmoto (2002); Koshino and Aoki (2003, 2004); Brüning *et al.* (2004)] and opens the possibility of exploring generic features that relate different models. Contrary to the Hofstadter butterfly which has Dirac nodes only for even q , there are strong arguments for the presence of Weyl nodes in Weyl butterflies at any commensurate flux, though a rigorous proof is the subject of future research.

Chapter 7

Disordered Floquet Chern insulators

One of the interesting outcomes of the interplay between non-equilibrium quantum dynamics and topology is the presence of exotic topological phases exclusive to such out-of-equilibrium scenarios. In this context, Floquet systems have emerged as ideal platforms for realization of such phases as, formally, their dynamics can be described stroboscopically by an effective Floquet Hamiltonian or equivalently the unitary time evolution operator over one period. Hence, how the topology of the phases is encoded in these operators is a question. Moreover, since disorder plays such an interesting and crucial role in quantum Hall systems, its effect on Floquet Chern insulating phases is naturally an interesting question. This chapter aims to answer these question by analyzing the phase diagram of the simple Chern insulator introduced in Chapter 2 subjected to a Floquet drive with and without disorder.

Generally, periodically driven systems are described via Hamiltonian parameters varying sinusoidally in time. Many of their qualitative aspects can however be modeled using simpler, tractable two-step modulations and their n -step generalizations [[Goldman and Dalibard \(2014\)](#)]. In two dimensions these systems can carry stroboscopic, chiral propagating modes localized on the edges. Bulk-edge correspondence suggests that presence of such edge modes is associated with some bulk topological order. Contrary to static non-interacting Chern insulators, Chern numbers are insufficient to classify the topological phases in Floquet systems due to the periodicity in the Floquet quasienergy which plays the role analogous to the energy of a static system. For instance, Floquet systems can have trivial bulk quasienergy bands with zero Chern number coexisting with topologically protected edge states [[Kita-gawa *et al.* \(2010\)](#); [Rudner *et al.* \(2013\)](#)]. Hence, more general winding numbers

that fully characterize the time evolution over one period of the bulk have been constructed [Kitagawa *et al.* (2010); Rudner *et al.* (2013)] and generalized for disordered systems [Titum *et al.* (2016)].

To analyze the topological phase diagram of the Chern insulator model subjected to a Floquet drive, the necessary topological invariants for a Floquet system are first discussed in Section 7.1. The specific Chern insulator model and the Floquet protocol is described in Section 7.2. Then the exact phase diagram of the translation invariant system is mapped out in Section 7.3 by locating the critical points by studying the topological gap closings in the Floquet quasienergy spectrum and characterizing the phases via winding invariants appropriate for the Floquet systems. The Floquet system is found to have a richer set of phases than the static system - with topological phases and associated chiral edge modes exclusive to Floquet systems. In fact, topological phases can appear in the Floquet systems at parameter regimes far away from those which host topological order in the static system. Interestingly, the topological phase depends only on the mean of the two-step periodic drive and not on the amplitude. However, the amplitude does affect the gaps in the Floquet quasienergy spectrum which in turn affect the localization lengths of the edge modes. In fact, there are regimes in the phase diagram where there exist non-topological gap closings, which do not lead to any phase transition but cause the Floquet edge modes to disappear through a divergence in their localization length. The effect of uncorrelated quenched disorder on the phase diagram is then discussed in Section 7.4. Although in a static two-dimensional system, disorder localizes all bulk states, systems with quantum Hall-like topological order necessarily have a narrow window of energy possessing delocalized states, which can be further understood from the response of the system to gauge flux insertion [Halperin (1982)]. The Floquet system considered in this work also has a similar behavior, however quasienergies of the delocalized states depend on the particular underlying topological phase. The phases in the presence of disorder are characterized by calculating the appropriate Floquet invariants generalized to include disorder [Kitagawa *et al.* (2010); Titum *et al.* (2016)]. Analysis of the bulk order indicates a transition to trivial phase at strong disorder. Robustness of the Floquet topological phases and hence the critical disorder for a disorder-induced topological transition is intimately connected to the localization lengths of the disorder free edge states and hence the gaps in the Floquet quasienergy spectrum. It is found that the disorder-induced topological phase transitions take place via a *levitation and annihilation* mechanism [Onoda *et al.* (2007)] generalized for Floquet systems. As shown schematically in Fig. 7.1, the delocalized states are present close to the edges of the

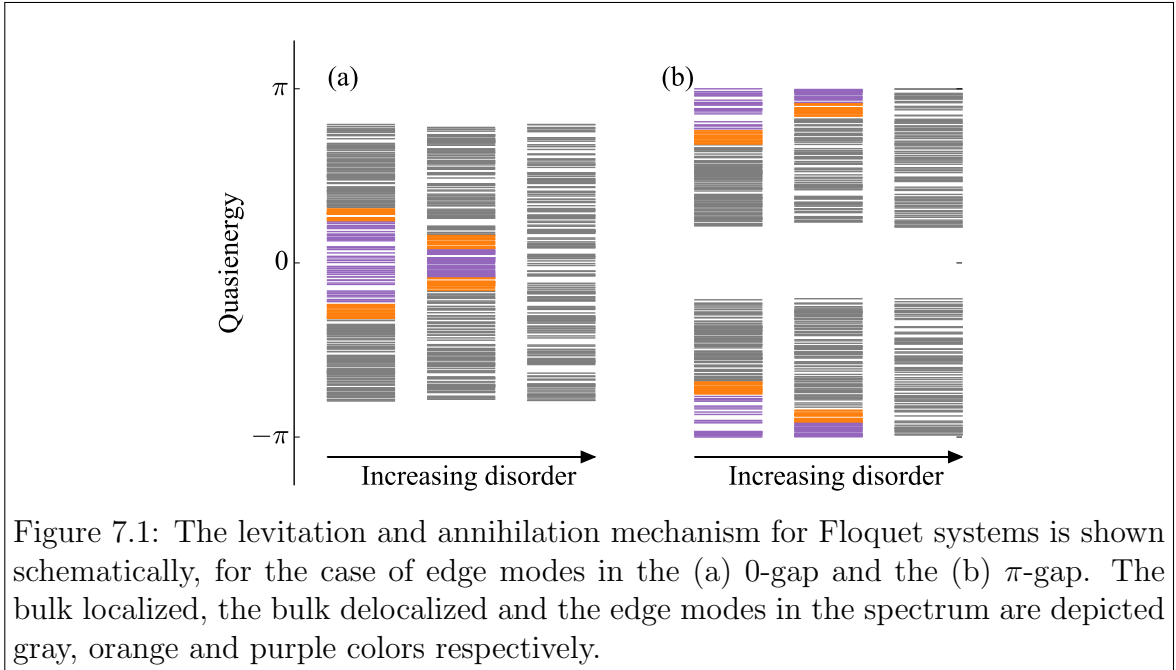


Figure 7.1: The levitation and annihilation mechanism for Floquet systems is shown schematically, for the case of edge modes in the (a) 0-gap and the (b) π -gap. The bulk localized, the bulk delocalized and the edge modes in the spectrum are depicted gray, orange and purple colors respectively.

bulk bands immediately surrounding the edge modes. As disorder is increased, the delocalized states from two bands levitate towards the gap before finally meeting and annihilating each other at the critical disorder. Evidence for this mechanism is presented by carefully analyzing energy resolved level-spacing statistics for the Floquet quasienergies.

7.1 Topological invariants for the Floquet system

Chern numbers of single particle bands provide a complete characterization of the edge modes in a static system in the absence of any symmetries [Ryu *et al.* (2010)]. Chern number of a band equals the difference between the chirality of edge modes above and below the band. Since the spectrum of the Hamiltonian is bounded, there are 0 chiral modes below the lowest energy band and above the highest band. As a result, the Chern numbers of the bands completely determine the counting of edge modes (chirality determines the number of modes, in the absence of any symmetries).

In close analogy to the notion of energy spectrum of a static Hamiltonian, one can define the quasienergy spectrum for a Floquet system. Quasienergies correspond to the argument of the complex unimodular eigenvalues of the unitary time evolution operator over a period of time. The quasienergies are periodic and are well defined modulo the frequency of the drive *i.e.* $\omega \equiv \omega + \frac{2\pi}{T}$. The quasienergy spectrum also has bands analogous to the energy bands of a static Hamiltonian. Chern number of

a such a Floquet band is again equal to the difference between the chirality of modes above and below. However, periodicity of the quasienergies implies that there is no notion of highest or lowest bands near which the number of edge modes can be fixed. The result is that Chern numbers do not completely characterize the number of edge modes. A striking instance of this is the anomalous Floquet Chern insulator in which all bands of the spectrum have zero Chern number but carry a chiral mode in every gap between the bands [Rudner *et al.* (2013)].

A bulk invariant which correctly characterizes such a Floquet system was introduced in Rudner *et al.* (2013) and generalized to the case of disordered systems in Titum *et al.* (2016). These invariants are used extensively in this work to numerically characterize the phases exhibited by our model system. A brief intuitive explanation and motivation for this invariant is presented in this section. The main result of the discussion is contained in Eq. (7.7).

Let $U(t)$, $t \in [0, T]$ be the time evolution operator of our system. For simplicity, in this section, assume units where $T = 1$. Consider a system with a modified time evolution of the following form

$$\mathcal{U}(t) = \begin{cases} U(2t) & t \in [0, \frac{1}{2}] \\ \exp[-i2H_{\text{eff}}(1-t)] & t \in [\frac{1}{2}, 1] \end{cases}, \quad (7.1)$$

where H_{eff} is the effective Hamiltonian, defined as

$$\exp[-iH_{\text{eff}}] = U(1). \quad (7.2)$$

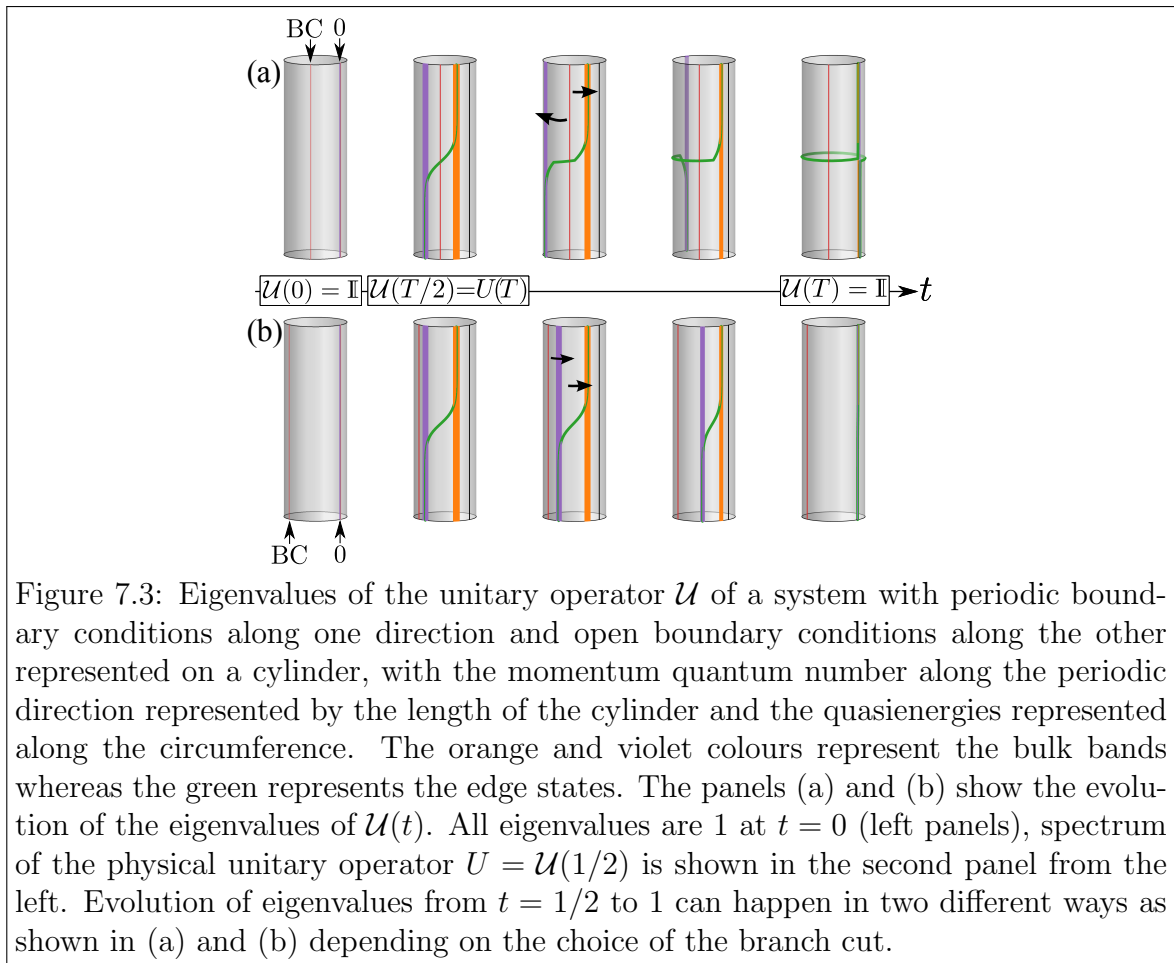
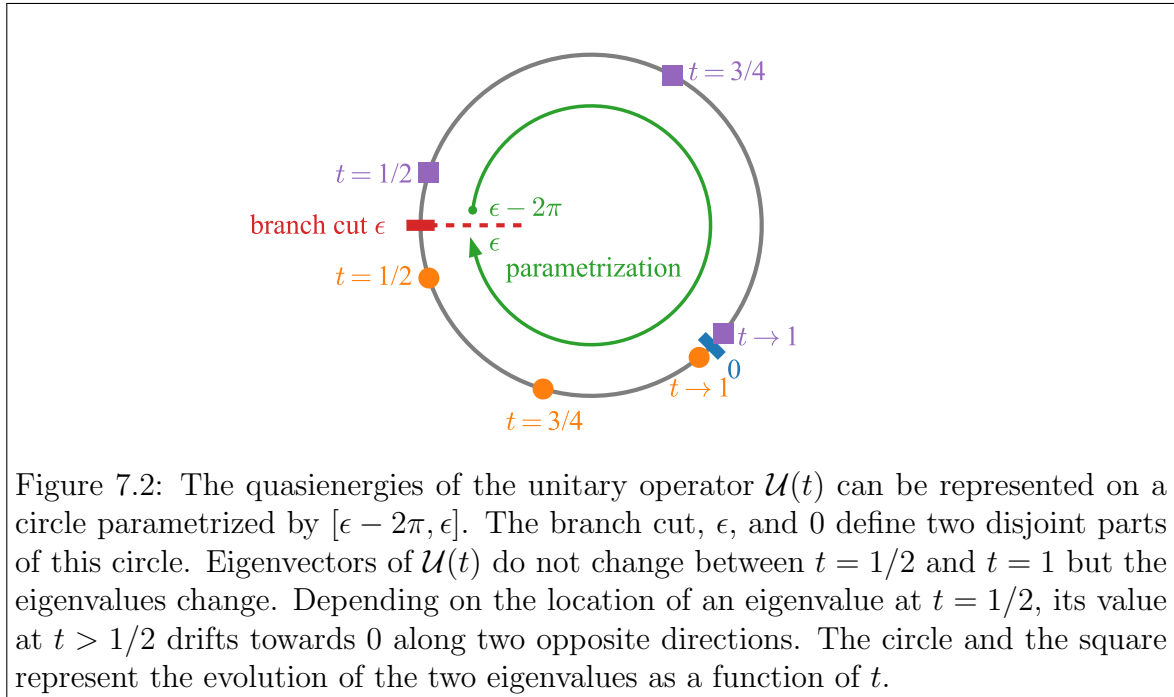
Eq. (7.2) does not uniquely define H_{eff} , and as will be discussed below, the definition of the winding number makes use of this freedom to probe the edge modes in different band gaps. If the eigenvalues and vectors of $U(1)$ are $\{u_i\}$ and $\{|i\rangle\}$, for some choice $\epsilon \in [0, 2\pi]$ of the branch cut, we can define H_{eff}^ϵ as

$$H_{\text{eff}}^\epsilon = \sum_i \omega_i |i\rangle \langle i|, \quad \omega_i = -\arg^\epsilon(u_i) \quad (7.3)$$

where \arg^x is defined to be between $x - 2\pi$ and x . With this choice, the modified unitary operator $\mathcal{U}(t)$ for the interval $t \in [\frac{1}{2}, 1]$ takes the form:

$$\mathcal{U}(t) = \sum_i \exp[-i\omega_i 2(1-t)] |i\rangle \langle i| \quad (7.4)$$

As t goes from $\frac{1}{2}$ to 1, $\mathcal{U}(t)$ interpolates from $U(1)$ to \mathbb{I} . The eigenvectors remain the same but the eigenvalues change from $e^{-i\omega_i}$ to 1. During the interpolation, the



eigenvalues on the two sides of the branch cut drift towards 1 along two different paths as shown in Fig. 7.2.

Consider the operator $\mathcal{U}(t)$ (7.1) for a two dimensional Floquet system with periodic boundary conditions along the y -direction such that the momentum k_y is a good quantum number, and open boundaries along the x -direction with chiral edge modes whose quasienergies are within the bulk gap surrounding some quasienergy ω_{edge} . This can be represented on a cylinder as shown in Fig. 7.3(a) (second panel), where the length of the cylinder represents the k_y -axis and the circular direction represents the quasienergies. If the branch cut ϵ is chosen to lie in the same gap that contains ω_{edge} , the operator $\mathcal{U}(t)$ for $t \in [1/2, 1]$ has an edge mode in the same gap. As t goes from 1/2 to 1, this edge mode is stretched in such a way that $\mathcal{U}(t \rightarrow 1)$ has an edge mode that winds around the entire cylinder, whereas all the bulk modes shrink to quasienergy 0. This is schematically shown in Fig. 7.3(a). The contrary scenario where the branch cut is chosen to be in a different gap results in the edge modes also shrinking to 0 as shown in Fig. 7.3(b).

The total number of chiral edge modes of $U(1)$ at quasienergy ϵ is the same as that of $\mathcal{U}^\epsilon(t \rightarrow 1)$ where \mathcal{U}^ϵ is the modified time evolution operator (7.1) defined with the branch cut placed at ϵ . This is captured by the winding number $\int \frac{dk_y}{2\pi} \text{Tr}[\mathcal{U}^{\epsilon\dagger} \partial_{k_y} \mathcal{U}^\epsilon]$, since this is identical to the total winding of the quasienergies $\nu = \sum_i \int \frac{dk_y}{2\pi i} \partial_{k_y} \omega_i$. The number of chiral modes on a single edge is obtained by projecting the integrand to sites on one half of the system as

$$n(\epsilon) = \int \frac{dk_y}{2\pi i} \text{Tr}[\mathcal{P} \mathcal{U}^{\epsilon\dagger}(1) \partial_{k_y} \mathcal{U}^\epsilon(1)] = \int_0^1 dt \partial_t \int \frac{dk_y}{2\pi i} \text{Tr}[\mathcal{P} \mathcal{U}^{\epsilon\dagger}(t) \partial_{k_y} \mathcal{U}^\epsilon(t)], \quad (7.5)$$

where \mathcal{P} is the projector onto one half of the system, Tr represents the trace over all sites, and $n(\epsilon)$ is the number of chiral edge modes at quasienergy ϵ . The second equality arises from the fact that the argument of ∂_t is a real-valued non-singular quantity that changes from 0 to n as t changes from 0 to 1. Note that the integrand in the above winding number is defined for an open system. The support of the integrand can be moved to the bulk by adding a total derivative $\partial_{k_y} \text{Tr}[\mathcal{P}(\mathcal{U}^{\epsilon\dagger} \partial_t \mathcal{U}^\epsilon)]$ to the integrand, giving

$$n(\epsilon) = \int \frac{dk_y dt}{2\pi i} \text{Tr}[\mathcal{U}^{\epsilon\dagger} \partial_{k_y} \mathcal{U}^\epsilon [\mathcal{P}, \mathcal{U}^{\epsilon\dagger} \partial_t \mathcal{U}^\epsilon]]. \quad (7.6)$$

Since \mathcal{P} is equal to the identity matrix close to the edges, the commutator in the integrand is non-zero only in the bulk, around the region where the diagonal of \mathcal{P} changes from 1 to 0. Assuming \mathcal{U} has a finite range, it can be replaced with the unitary

operator \mathcal{U} defined for a system with periodic boundary conditions. Expressing the operators in the momentum basis, one arrives at

$$n(\epsilon) = \int \frac{d^2\mathbf{k}dt}{8\pi^2} \text{Tr} [\mathcal{U}^{\epsilon\dagger} \partial_t \mathcal{U}^\epsilon [\mathcal{U}^{\epsilon\dagger} \partial_{k_x} \mathcal{U}^\epsilon, \mathcal{U}^{\epsilon\dagger} \partial_{k_y} \mathcal{U}^\epsilon]]. \quad (7.7)$$

$\mathcal{U}^\epsilon \equiv \mathcal{U}^\epsilon(t, k_x, k_y)$ is the modified time evolution operator defined for a system with periodic boundary conditions,

$$\mathcal{U}^\epsilon(t, k_x, k_y) = \begin{cases} U_{\mathbf{k}}(2t) & t \in [0, \frac{1}{2}] \\ \exp[-i2H_{\text{eff},\mathbf{k}}^\epsilon(1-t)] & t \in [\frac{1}{2}, 1] \end{cases}, \quad (7.8)$$

where $H_{\text{eff},\mathbf{k}}^\epsilon$ is the effective Hamiltonian defined with all quasienergies inside the interval $[\epsilon - 2\pi, \epsilon]$.

Note that the original time evolution operator U does not return to itself at $t = T$ since $U(t = T) \neq U(t = 0)$. The modified time evolution, while preserving the edge counting (in the gap selected by the branch cut) satisfies $\mathcal{U}(t = T) = \mathcal{U}(t = 0)$. This allows us to compactify time and characterize \mathcal{U} using homotopy classes of maps from $S_t^1 \times S_{k_x}^1 \times S_{k_y}^1$ to the unitary group [Bott and Seeley (1978)]. The characterizing invariant is given by Eq. (7.7).

The Floquet system considered in this chapter has two gaps - around 0 and π , and the topology of the drive is defined by the counting of the edge modes in the two gaps. Thus the phases of the Floquet system can be fully characterized by the pair (ν_0, ν_π)

$$\nu_0 = n(0) \text{ and } \nu_\pi = n(\pi). \quad (7.9)$$

Although insufficient to characterize the phases of the Floquet system, the Chern number of the Floquet bulk bands, \mathcal{C} , within a quasienergy window $\omega \in [0, \pi]$ is the difference in the number of chiral edge modes at 0 and π and can be formally expressed as

$$\mathcal{C} = \nu_0 - \nu_\pi = \int \frac{d\mathbf{k}}{4\pi} \text{Tr} [\mathcal{P}_{\mathbf{k}} [\partial_{k_x} \mathcal{P}_{\mathbf{k}}, \partial_{k_y} \mathcal{P}_{\mathbf{k}}]], \quad (7.10)$$

where $\mathcal{P}_{\mathbf{k}}$ is the projector onto eigenstates of $H_{\text{eff},\mathbf{k}}^\epsilon$ having quasienergies in window $[0, \pi]$.

The winding number described above can be generalized to the case of disordered systems by considering a periodic superlattice constructed with the entire disordered system as the unit cell. Presence of an edge mode in a single disordered sample implies the presence of an edge mode also in the superlattice. The above expressions can now be used to probe the presence of an edge mode in this system also. The quasimomenta

on this lattice appear as twisted boundary conditions across each unit cell due to the phase gained by hopping from one unit cell to another. After a change in basis, the twisted boundary conditions can be reinterpreted as flux insertions through the two holes of the torus as the quasimomentum phase gained at the edge can be redistributed over the entire system via a gauge transformation. This results in a form of the winding number similar to the one in Eq. (7.7) but $\mathcal{U}(t, k_x, k_y)$ is now replaced by $\mathcal{U}(t, \theta_x, \theta_y)$ representing the unitary operator for a system with periodic boundary conditions but with fluxes $\theta_{x,y}$ through the holes of the two-torus representing the two spatial directions.

7.2 Model and two-step Floquet drive

7.2.1 Static properties

The model of choice for explicit calculations is the Chern insulator model on a square lattice described in Chapter 2 Section 2.1.2. The Hamiltonian for the model can be reduced to a family of two-level Hamiltonians in reciprocal space, each corresponding to a momentum mode which can be represented using Pauli matrices as $\mathcal{H}_{\mathbf{k}} = \mathbf{d}_{\mathbf{k}} \cdot \boldsymbol{\sigma}$ where,

$$\mathbf{d}_{\mathbf{k}} = -\{J \sin k_x, J \sin k_y, J \cos k_x + J \cos k_y - M\}. \quad (7.11)$$

The vector $\mathbf{d}_{\mathbf{k}}$ in Eq. (7.11) represents a pseudospin texture in the Brillouin zone, whose skyrmion number gives the Chern numbers of the two underlying bands. Since they have to sum up to zero, they are negative of each other. As mentioned in Section 2.1.2, the model hosts topological phase transitions at $M = 0$ and $M/J = \pm 2$ with the Chern number of the lower band being 0 for $|M/J| > 2$ and $\text{sgn}(M/J)$ for $|M/J| < 2$. The transitions are accompanied by linear gap closings in the energy spectrum at the high-symmetry points of the Brillouin zone, they being $(0, 0)$ for $M = 2J$, (π, π) for $M = -2J$, and $(0, \pi)$ and $(\pi, 0)$ for $M = 0$. Consistent with the understanding that ground state spinors of two-level systems (determined by $\mathbf{d}_{\mathbf{k}} \cdot \boldsymbol{\sigma}$) in different topological phases are orthogonal at least at one point in the Brillouin zone, it turns out that the $\mathbf{d}_{\mathbf{k}}$ s (7.11) in different adjacent topological phases are indeed anti-parallel¹ at the gap closing high-symmetry point(s). This can be confirmed by

¹The modulus of the overlap squared of ground state spinors corresponding to $\mathbf{d}_1 \cdot \boldsymbol{\sigma}$ and $\mathbf{d}_2 \cdot \boldsymbol{\sigma}$ is given by $(1 + \mathbf{d}_1 \cdot \mathbf{d}_2)/2$.

analyzing the skyrmion textures at the high-symmetry points which turn out to be

$$\begin{aligned}\mathbf{d}_{(0,0)} &= \{0, 0, 2J - M\}, \\ \mathbf{d}_{(\pi,\pi)} &= \{0, 0, -2J - M\}, \\ \mathbf{d}_{(0,\pi)} &= \mathbf{d}_{(\pi,0)} = \{0, 0, M\}.\end{aligned}\tag{7.12}$$

It is sufficient to focus only at the high-symmetry points as the skyrmion textures corresponding to two different values, M_A and M_B , can become anti-parallel only at the high-symmetry points. This is because, $\mathbf{d}_{A,\mathbf{k}} = -\mathbf{d}_{B,\mathbf{k}}$ implies $d_{\mathbf{k}}^x = 0 = d_{\mathbf{k}}^y$ as $d_{\mathbf{k}}^x$ and $d_{\mathbf{k}}^y$ are independent of M which is evident from Eq. (7.11). Hence, critical points in the parameter space can be deduced from the zeros of $\mathbf{d}_{\mathbf{k}}$ at the high-symmetry points in Eq. (7.12).

7.2.2 Two-step Floquet drive

We subject the Chern insulator model to a two-step Floquet drive by periodically modulating the mass term in the Hamiltonian as

$$M(t) = \begin{cases} M_A; & nT < t < (n + 1/2)T \\ M_B; & (n + 1/2)T < t < (n + 1)T. \end{cases}\tag{7.13}$$

The resulting time-periodic Hamiltonian is denoted as

$$\mathcal{H}_{\mathbf{k}}(t) = \begin{cases} \mathbf{d}_{A,\mathbf{k}} \cdot \boldsymbol{\sigma}; & nT < t < (n + 1/2)T \\ \mathbf{d}_{B,\mathbf{k}} \cdot \boldsymbol{\sigma}; & (n + 1/2)T < t < (n + 1)T, \end{cases}\tag{7.14}$$

where

$$\mathbf{d}_{X,\mathbf{k}} = -J\{\sin k_x, \sin k_y, \cos k_x + \cos k_y - \frac{M_X}{J}\}.\tag{7.15}$$

In the rest of the chapter, T is set to unity such that the parameter space is spanned by J , M_A , and M_B . The properties of a periodically driven system are governed by the time-evolution operator (Floquet operator) over one period, $U(1) = U_{\mathcal{F}}$. For the time-periodic Hamiltonian (7.14), $U_{\mathcal{F},\mathbf{k}}$ can be expressed as

$$U_{\mathcal{F},\mathbf{k}} = e^{-i\mathbf{d}_{B,\mathbf{k}} \cdot \boldsymbol{\sigma}/2} e^{-i\mathbf{d}_{A,\mathbf{k}} \cdot \boldsymbol{\sigma}/2} = d_{0,\mathbf{k}} \mathbb{I}_2 - i \mathbf{d}_{\text{eff},\mathbf{k}} \cdot \boldsymbol{\sigma},\tag{7.16}$$

and $\omega_{\pm,\mathbf{k}} = \pm \cos^{-1} d_{0,\mathbf{k}}$ are the Floquet quasienergies which also satisfy $\omega_{\pm,\mathbf{k}} = \pm \sin^{-1} |\mathbf{d}_{\text{eff},\mathbf{k}}|$. For the model (7.11), $\mathbf{d}_{\text{eff},\mathbf{k}}$ can be explicitly obtained by using Eq. (7.15) in Eq. (7.16) which gives

$$\begin{aligned}\mathbf{d}_{\text{eff},\mathbf{k}} &= \sin(d_{A,\mathbf{k}}/2) \cos(d_{B,\mathbf{k}}/2) \hat{\mathbf{d}}_{A,\mathbf{k}} + \cos(d_{A,\mathbf{k}}/2) \sin(d_{B,\mathbf{k}}/2) \hat{\mathbf{d}}_{B,\mathbf{k}} + \\ &\quad \sin(d_{A,\mathbf{k}}/2) \sin(d_{B,\mathbf{k}}/2) \hat{\mathbf{d}}_{A,\mathbf{k}} \wedge \hat{\mathbf{d}}_{B,\mathbf{k}}.\end{aligned}\tag{7.17}$$

7.3 Phase diagram for translation-invariant system

The topological phase transitions in the Floquet system can be understood by examining the nature of the gap closings in the spectrum of the Floquet quasienergies. The gapless points in the quasienergy spectrum can be found by setting $\mathbf{d}_{\text{eff},\mathbf{k}} = 0$. This naturally implies that, at the gapless points, $d_{0,\mathbf{k}} = 1$ or $d_{0,\mathbf{k}} = -1$. The former corresponds to the gap closing at $\omega_{\pm} = 0 \pmod{2\pi}$ whereas the latter corresponds to the ones at $\omega_{\pm} = \pm\pi \pmod{2\pi}$. If the gap closings happen at the high-symmetry points in the Brillouin zone, it leads to a topological phase transition accompanied by a change in ν_0 or ν_{π} , the former corresponding to a gap closing at $\omega = 0$ whereas the latter to $\omega = \pi$. Interestingly, the Floquet drive can lead to gap closings in the quasienergy spectrum elsewhere in the Brillouin zone which do not correspond to any topological transition, but lead to disappearance of the Floquet topological edge modes at these singular points (lines) in the phase diagram. This has further ramifications on the robustness of these edge states and the quantitative nature of the phase diagram in the presence of disorder discussed in Section 7.4.

Closing of a gap in the Floquet quasienergy spectrum necessitates $\hat{\mathbf{d}}_{A,\mathbf{k}} \wedge \hat{\mathbf{d}}_{B,\mathbf{k}}$ itself to be zero, or the coefficient of $\hat{\mathbf{d}}_{A,\mathbf{k}} \wedge \hat{\mathbf{d}}_{B,\mathbf{k}}$ in Eq. (7.17) to be zero, as $\hat{\mathbf{d}}_A \wedge \hat{\mathbf{d}}_B$ is perpendicular to both $\hat{\mathbf{d}}_A$ and $\hat{\mathbf{d}}_B$. As argued in Section 7.2.1, the former can happen only at the high-symmetry points in the Brillouin zone. Inspection of Eq. (7.17) reveals that at these high-symmetry points, $d_{\text{eff}}^x = 0 = d_{\text{eff}}^y$. Hence, by tuning the parameters of the Floquet system, one can flip the sign of d_{eff}^z effectively making the skyrmion texture anti-parallel at the high-symmetry points leading to a phase transition. Analysis of Eq. (7.17) also shows that for the latter case, where the coefficient of $\hat{\mathbf{d}}_{A,\mathbf{k}} \wedge \hat{\mathbf{d}}_{B,\mathbf{k}}$ vanishes, for the vector \mathbf{d}_{eff} to vanish, $d_A = 2n\pi$ and $d_B = 2m\pi$ necessarily. This can happen generically anywhere in the Brillouin zone away from the high-symmetry points and such gap closings do not correspond to any phase transitions.

7.3.1 Topological phase transitions

For a topological transition to occur in the Floquet system, $\hat{\mathbf{d}}_{A,\mathbf{k}} \wedge \hat{\mathbf{d}}_{B,\mathbf{k}} = 0$, implying $\hat{\mathbf{d}}_{A,\mathbf{k}}$ and $\hat{\mathbf{d}}_{B,\mathbf{k}}$ are parallel or anti-parallel, which can happen only at the high-symmetry points in the Brillouin zone as argued at the end of Section 7.2.2. At

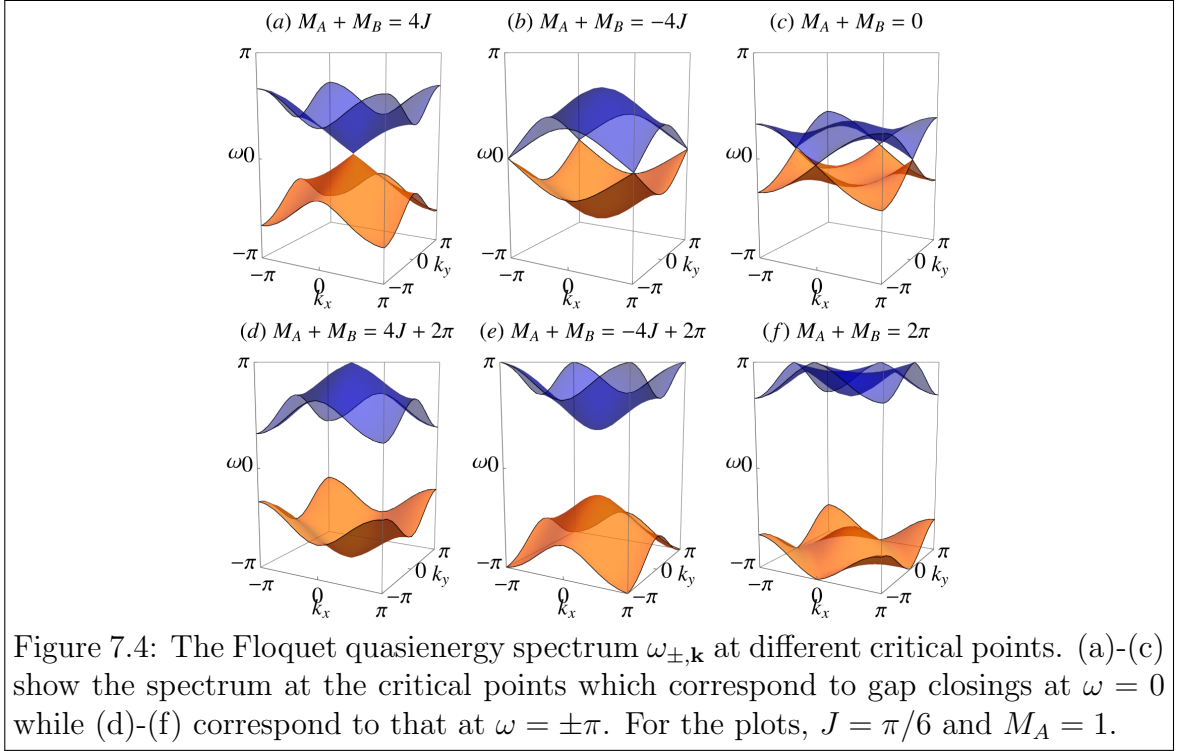


Figure 7.4: The Floquet quasienergy spectrum $\omega_{\pm, \mathbf{k}}$ at different critical points. (a)-(c) show the spectrum at the critical points which correspond to gap closings at $\omega = 0$ while (d)-(f) correspond to that at $\omega = \pm\pi$. For the plots, $J = \pi/6$ and $M_A = 1$.

these points, the Floquet quasienergies have the forms

$$\begin{aligned}
 \omega_{\pm, (0,0)} &= \pm(4J - M_A - M_B)/2, \\
 \omega_{\pm, (\pi, \pi)} &= \pm(4J + M_A + M_B)/2, \\
 \omega_{\pm, (0, \pi)} &= \omega_{\pm, (\pi, 0)} = \pm(M_A + M_B)/2.
 \end{aligned} \tag{7.18}$$

By setting of $\omega_{\pm, \mathbf{k}} = 0$ and $\omega_{\pm, \mathbf{k}} = \pi$ in Eq. (7.18), the critical points can be obtained as

$$M_A + M_B = 4J\eta + (4n + 2\zeta)\pi, \tag{7.19}$$

where ζ takes values 0(+1) for a transition with a gap closing at $\omega = 0(\pi)$ and η takes values -1, 0 and +1 depending on the particular symmetry point at which the gap closes. One of the most important observations from the expression for the critical points (7.19) is that they only depend on $M_A + M_B$, which physically means that the topological properties of the Floquet system depend only on the mean of the binary drive and not on the amplitude. Moreover, Eq. (7.19) also reveals that the phase diagram is periodic in $M_A + M_B$ with a period of 4π . Representative Floquet quasienergy spectra at different critical points are plotted in Fig. 7.4 showing the gap closings at the corresponding high-symmetry points.

Having established the critical points of the Floquet system, the transitions are characterized in terms of the change in the Floquet winding numbers ν_0/π and the Chern number \mathcal{C} . If there exists a topological gap closing, then the effective Hamiltonian in the vicinity of the gapless mode has the form

$$\sum_{i,j=x,y} \kappa_i \mathcal{A}_{ij} \sigma^j + \lambda \sigma^z, \quad (7.20)$$

where λ is the effective mass which goes to zero at the transition. Across a transition, the change in the Chern number of the band arises from the vicinity of the gapless mode. The change is given by $\sum_{\mu} \text{sgn}(\text{Det}[\mathcal{A}^{\mu}])(\text{sgn}\lambda_{+}^{\mu} - \text{sgn}\lambda_{-}^{\mu})/2$ [Bernevig and Hughes (2013)] where μ indexes the gapless momenta and λ_{\pm}^{μ} is the effective mass on either side of the critical point. Hence, the nature of transitions can be understood by studying $\mathbf{d}_{\text{eff},\mathbf{k}}$ in the vicinity of the high-symmetry points. In the vicinity of the gapless mode at $\mathbf{k} = (0, 0)$, the effective Hamiltonian has the form of Eq. (7.20) with

$$\mathcal{A}_{ij} = -J \left[\frac{\sin\left(J - \frac{M_A}{2}\right) \cos\left(J - \frac{M_B}{2}\right)}{2J - M_A} + \frac{\cos\left(J - \frac{M_A}{2}\right) \sin\left(J - \frac{M_B}{2}\right)}{2J - M_B} \right] \delta_{ij}, \quad (7.21)$$

and $\lambda = \sin[(M_A + M_B - 4J)/2]$. Consequently, $\text{Det}[\mathcal{A}] = 2A_{xx}^2 > 0$, resulting in $\text{sgn}(\text{Det}[\mathcal{A}]) = 1$ and the effective mass being $\sin((M_A + M_B - 4J)/2)$. Hence across the phase transition between two points in the parameter space such that $M_A + M_B - 4J < 4n\pi$ and $M_A + M_B - 4J > 4n\pi$, the effective mass changes from negative to positive, hence the Chern number changes by $+1$. Since the topological transition is accompanied by a gap closing at $\omega = 0$, ν_0 also changes by $+1$. Correspondingly, between two points such that $M_A + M_B - 4J < (4n+2)\pi$ and $M_A + M_B - 4J > (4n+2)\pi$, the Chern number changes by -1 consistent with the change of the sign of effective mass and consequently ν_{π} changes by $+1$.

Similarly, close to $\mathbf{k} = (\pi, \pi)$

$$\mathcal{A}_{ij} = -J \left[\frac{\sin\left(J + \frac{M_A}{2}\right) \cos\left(J + \frac{M_B}{2}\right)}{2J + M_A} + \frac{\cos\left(J + \frac{M_A}{2}\right) \sin\left(J + \frac{M_B}{2}\right)}{2J + M_B} \right] \delta_{ij}, \quad (7.22)$$

with $\lambda = \sin[(M_A + M_B + 4J)/2]$, again leading to $\text{Det}[\mathcal{A}] = 2A_{xx}^2 > 0$. Consequently, $\text{sgn}(\text{Det}[\mathcal{A}]) = 1$ and the effective mass is of the form $\sin((M_A + M_B + 4J)/2)$. Hence similar to the $\mathbf{k} = (0, 0)$ case, the Chern number changes by $+1$ across a transition at $M_A + M_B = -4J + 4n\pi$ and by -1 across a transition at $M_A + M_B = -4J + (4n+2)\pi$.

Finally around $\mathbf{k} = (0, \pi)$,

$$\mathcal{A}_{ij} = -J \left[\frac{\cos(M_B/2) \sin(M_A/2)}{M_A} + \frac{\cos(M_A/2) \sin(M_B/2)}{M_A} \right] \delta_{ij} (\delta_{ix} - \delta_{iy}) \quad (7.23)$$

Critical points	$\Delta\mathcal{C}$	$\Delta\nu_0$	$\Delta\nu_\pi$
$M_A + M_B = 4J + 4n\pi$	-1	-1	0
$M_A + M_B = 4J + (4n + 2)\pi$	+1	0	-1
$M_A + M_B = 4n\pi$	+2	+2	0
$M_A + M_B = (4n + 2)\pi$	-2	0	+2
$M_A + M_B = -4J + 4n\pi$	-1	-1	0
$M_A + M_B = -4J + (4n + 2)\pi$	+1	0	-1

Table 7.1: Summary of the phase transitions of the periodically driven Chern insulator. The four columns show the critical points, the changes in \mathcal{C} , ν_0 , and ν_π .

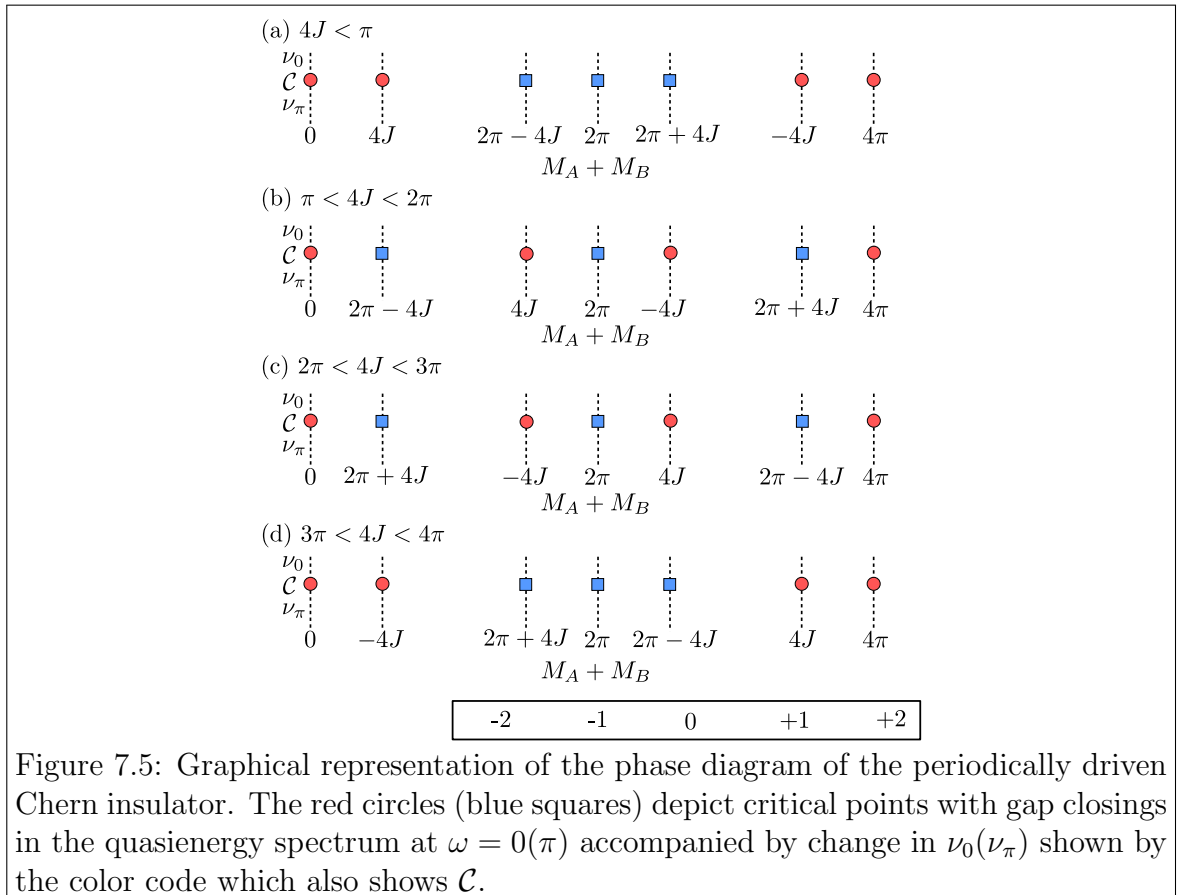


Figure 7.5: Graphical representation of the phase diagram of the periodically driven Chern insulator. The red circles (blue squares) depict critical points with gap closings in the quasienergy spectrum at $\omega = 0(\pi)$ accompanied by change in $\nu_0(\nu_\pi)$ shown by the color code which also shows \mathcal{C} .

and $\lambda = \sin[(M_A + M_B)/2]$. Consequently $\text{Det}[\mathcal{A}] = -2A_{xx}^2 < 0$. At both gapless modes at $\mathbf{k} = (0, \pi)$ and $\mathbf{k} = (\pi, 0)$, the effective mass has a form $\sin((M_A + M_B)T/2)$ and $\text{sgn}(\text{Det}[\mathcal{A}]) = -1$, hence the gap closings at $\omega = 0$ lead to change in the Chern number of -2 and those at $\omega = \pi$ lead to change in the Chern number by $+2$ as there are two inequivalent points in the Brillouin zone where the gap closes.

These set of rules completely characterize the phase diagram and the topological phase transitions of the periodically driven Chern insulator and are summarized in Table. 7.1.

The phase diagram is corroborated by explicitly calculating ν_0 , ν_π , and \mathcal{C} using Eqs. (7.7) and (7.10), and a generic phase diagram for the model is shown graphically in Fig. 7.5. It is interesting to note that with regard to sequence of $\nu_{0,\pi}$ and \mathcal{C} in the phase diagram, there are only two distinct kinds of phase diagrams hosted by the model which correspond to Fig. 7.5(a) and (b). While the latter corresponds to the case $4J[\text{mod}4\pi] \in [\pi, 3\pi]$, the former corresponds to the case otherwise.

7.3.2 Non-topological gap closings

In addition to the topological critical points, there also exist certain gap closings of the Floquet quasienergy spectrum which do not lead to any change in the topology of the Floquet bands. Since these gap closings happen away from the high-symmetry points, generically we have $\hat{\mathbf{d}}_A \wedge \hat{\mathbf{d}}_B \neq 0$, hence its coefficient in Eq. (7.17) has to vanish, implying $\sin d_A = 0$ and/or $\sin d_B = 0$. Inspection of Eq. (7.17) reveals that for \mathbf{d}_{eff} to vanish, both of them have to vanish simultaneously. Hence, formally the solutions of these gap closings can be obtained from the family of solutions of the system of equations

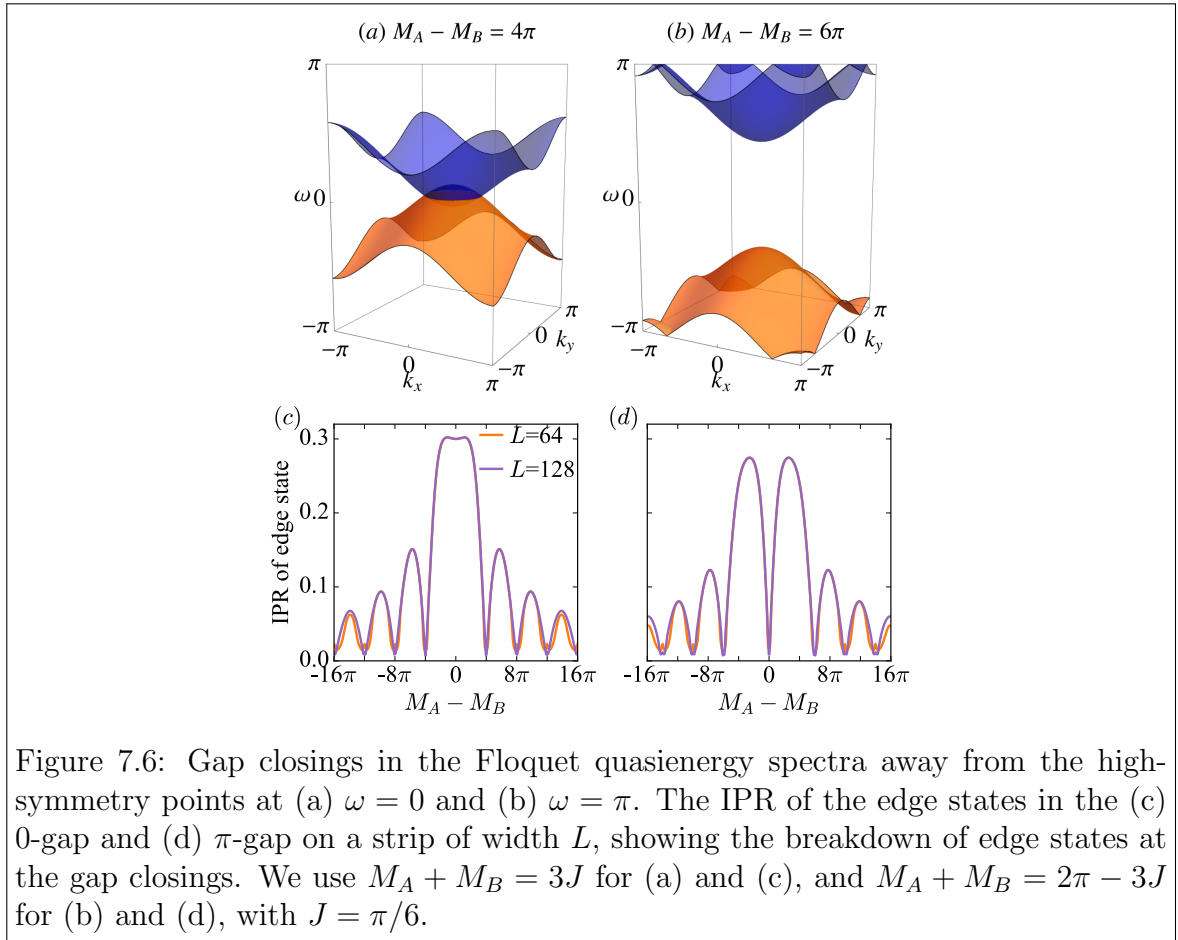
$$2J^2(1 + \cos k_x \cos k_y) + M_A^2 - 2JM_A(\cos k_x + \cos k_y) = 4n^2\pi^2, \quad (7.24)$$

$$2J^2(1 + \cos k_x \cos k_y) + M_B^2 - 2JM_B(\cos k_x + \cos k_y) = 4m^2\pi^2, \quad (7.25)$$

where n and m are integers. A tractable closed form of solutions to Eqs. (7.24) and (7.25) could not be obtained, however a numerical analysis of the quasienergy spectrum shows that these gap closings happen at

$$M_A - M_B \approx 2n\pi; \quad n \in \mathbb{Z}, |n| \geq 2, \quad (7.26)$$

at $\omega = 0(\pi)$ for n being even (odd). Note that these points depend only on the amplitude of the periodic drive and not the mean. This is consistent with the observation made in Section 7.3.1 below Eq. (7.19) that the topological properties of the Floquet bands depend only on the mean and not the amplitude of the drive.



Although the topological properties of the Floquet bands, and hence the presence (absence) and the chiralities of the Floquet edge modes do not change across these gap closings, they do have important bearings on the robustness of the edge modes. The localization length of the edge modes is inversely proportional to the minimum gap around the corresponding quasienergy (0 or π) in the spectrum *i.e.*

$$\xi_0^{-1} \propto \min[\omega_{+, \mathbf{k}}]; \quad \xi_\pi^{-1} \propto \pi - \max[\omega_{+, \mathbf{k}}], \quad (7.27)$$

where $\xi_{0(\pi)}$ is the localization length of the edge modes in the $0(\pi)$ -gap. Hence, as the gap in the quasienergy spectrum decreases, the localization length increases. At the point where the gap closes, ξ_0 or ξ_π diverges depending on if the quasienergy where the gap closes is at 0 or π , and the edge state vanishes. By explicitly calculating the inverse participation ratio (IPR) of the edge states as a function of $M_A - M_B$, it can be seen that it indeed goes to zero at the gap closings signaling a breakdown of the edge state through divergence of its localization length. Representative quasienergy spectra showing such gap closings are shown in Fig. 7.6 which also shows the vanishing IPR of the edge states at the gap closings. The IPR of a state $|\psi\rangle$ is defined as $\sum_{\mathbf{r}} |\psi(\mathbf{r})|^4$. The IPR of a localized state is inversely proportional to the localization length, whereas for a delocalized state it is inversely proportional to the system size. Consequently, in Fig. 7.6, the minima of the IPR indicate the edge-mode delocalizations that are concurrent with the non-topological gap closings. It should be reiterated that on either side of this gap closing, there is no change in the chiralities of the edge states.

7.4 Phase diagram in presence of disorder

In this section, the effect of disorder on the phase diagram of the periodically driven Chern insulator is discussed. The phases are characterized by calculating the winding invariants, ν_0 and ν_π , generalized for disordered systems [Kitagawa *et al.* (2010); Titum *et al.* (2016)]. Further, by analyzing energy resolved level spacing statistics, the mechanism behind the disorder-induced transitions is shown to be, what is referred to as *levitation and annihilation* [Onoda *et al.* (2007)], extended for Floquet systems. The uncorrelated Anderson disorder is taken to be of the form

$$\begin{aligned} M_{\mathbf{r}, \alpha} &= M + \delta M_{\mathbf{r}, \alpha}; & M_{\mathbf{r}, \beta} &= -M + \delta M_{\mathbf{r}, \beta}, \\ \delta M_{\mathbf{r}, \alpha}, \delta M_{\mathbf{r}, \beta} &\in [-W/2, W/2]. \end{aligned} \quad (7.28)$$

Note that the translation invariant part of $M_{\mathbf{r}}$ has the staggered structure on the two sublattices, but the disorder does not, and only the translation invariant part is driven periodically in time as similar to Eq. (7.13). The realization of the disorder δM stays constant with time.

7.4.1 Topological invariants with disorder

Since in the presence of disorder, momentum ceases to be good quantum number, the formulation of the topological invariants needs to go beyond the Brillouin zone. Drawing inspiration from Laughlin's argument [Laughlin (1981)] for quantized charge transfer in a system with quantum Hall-like edge states under threading of fluxes, consider that the Hamiltonian of the system has additional time-independent fluxes $\boldsymbol{\theta} = (\theta_x, \theta_y)$ threaded through the lattice. For a system with periodic boundary conditions on a torus, the fluxes play the role analogous to that of quasimomenta for the superlattice, for which the unit cell is composed of the $2 \times L_x \times L_y$ disordered lattice. Hence one can define a family of return maps, $\mathcal{U}_{\boldsymbol{\theta}}^{\epsilon}$, (for each $\boldsymbol{\theta}$), similar to Eq. (7.1), but for the disordered driven system by replacing $U(t)$ by $U_{\boldsymbol{\theta}}(t)$ which represents the time-evolution operator in the presence of flux $\boldsymbol{\theta}$. The winding numbers are then defined as

$$\nu_{\epsilon} = \int_0^1 dt \int \frac{d^2\boldsymbol{\theta}}{8\pi^2} \left[\text{Tr}(\mathcal{U}^{\epsilon\dagger} \partial_t \mathcal{U}^{\epsilon} [\mathcal{U}^{\epsilon\dagger} \partial_{\theta_x} \mathcal{U}^{\epsilon}, \mathcal{U}^{\epsilon\dagger} \partial_{\theta_y} \mathcal{U}^{\epsilon}]) \right], \quad (7.29)$$

where $\mathcal{U}^{\epsilon} \equiv \mathcal{U}_{\boldsymbol{\theta}}^{\epsilon}(t)$. Within this framework, we indeed obtain $\nu_0 - \nu_{\pi} = \mathcal{C}$, where \mathcal{C} is the Chern number of the disordered system defined as

$$\mathcal{C} = \int \frac{d^2\boldsymbol{\theta}}{4\pi} \text{Tr}(\mathcal{P}_{\boldsymbol{\theta}} [\partial_{\theta_x} \mathcal{P}_{\boldsymbol{\theta}}, \partial_{\theta_y} \mathcal{P}_{\boldsymbol{\theta}}]), \quad (7.30)$$

where $\mathcal{P}_{\boldsymbol{\theta}}$ is the projector onto the eigenstates of the Floquet operator having quasienergy eigenvalues $-\pi < \omega < 0$. Note that in the numerical implementation of Eqs. (7.29) and (7.30), a certain amount of disorder averaging is necessary to wash out the fluctuations due to finite size effects. However, since the quantities are topological invariants, no disorder averaging is deemed necessary in the thermodynamic limit [Hastings and Michalakis (2015)].

7.4.2 Features of the phase diagram

The effect of disorder on the phases is studied by numerically calculating ν_0/π using Eq. (7.29) for parameters corresponding to the two qualitative kinds of phase diagrams

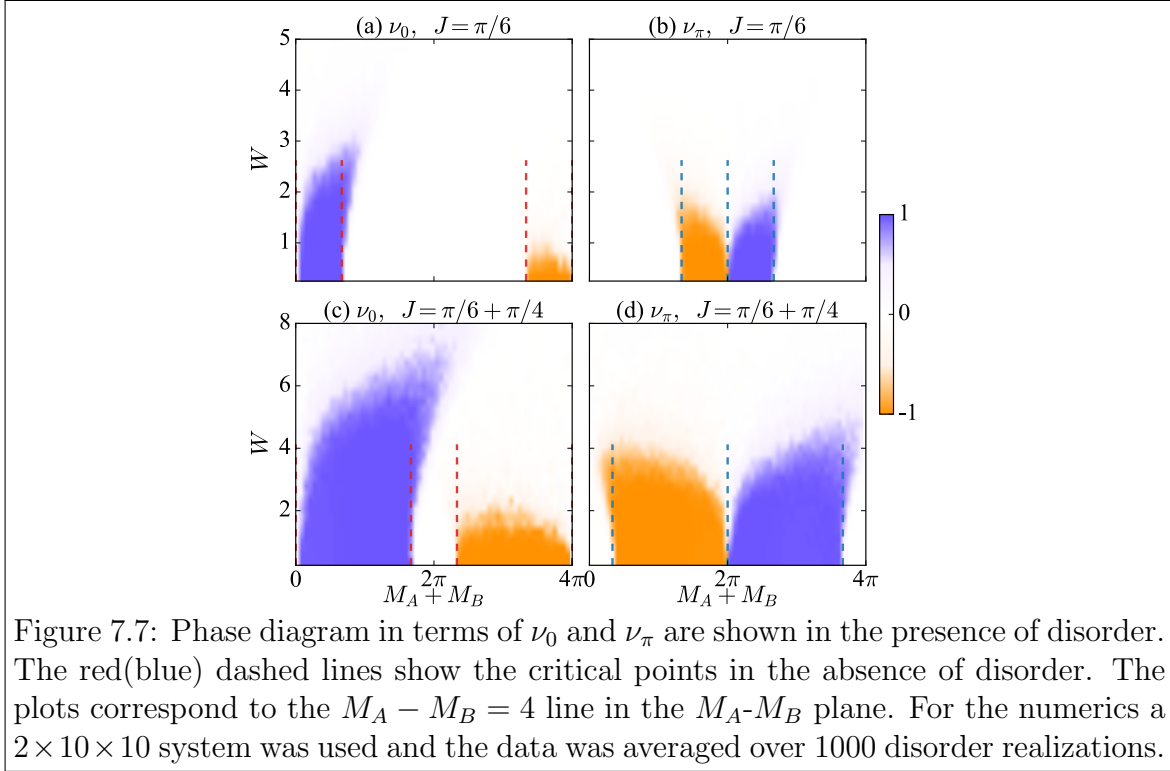


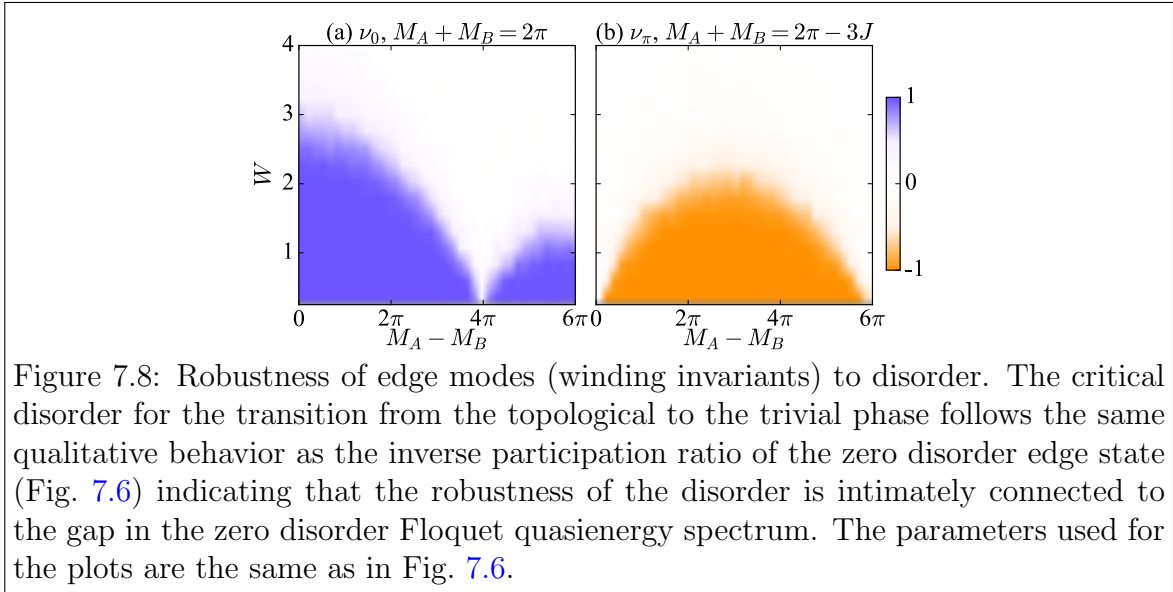
Figure 7.7: Phase diagram in terms of ν_0 and ν_π are shown in the presence of disorder. The red(blue) dashed lines show the critical points in the absence of disorder. The plots correspond to the $M_A - M_B = 4$ line in the $M_A - M_B$ plane. For the numerics a $2 \times 10 \times 10$ system was used and the data was averaged over 1000 disorder realizations.

for the translation-invariant system (Fig. 7.5(a)-(b)). Representative results are shown in Fig. 7.7. The key features of the phase diagram of the system are as follows.

Consistent with the general idea of topological invariance and protection of edge states, weak disorder does not affect the phases of the system. However, starting from a topological phase at zero disorder, the system transits to a trivial one at strong disorder. Analysis of level statistics indicates that the system is fully Anderson localized above the transition.

The critical disorder strength for the transition is lower for systems with parameters $M_{A,B}$ near a phase with an opposite winding number, as compared to systems with parameters close to a trivial phase, indicating that the topological phase in the latter case is much more robust to disorder than the former. This leads to a “V”-like shape of the phase boundaries² for instance at $M_A + M_B = 0$ in Fig. 7.7(a) and (c), and $M_A + M_B = 2\pi$ in Fig. 7.7(b) and (d). An intuitive explanation for the shape could be obtained from a long-wavelength picture, in which the system at critical disorder strengths can be described as made of a distributions of topological and trivial clusters. Changing the parameter $M_A + M_B$ closer to the opposite topological phase results in introduction of clusters of the opposite winding number. At a coarser scale,

²Phase boundaries here refer to the boundaries between the white, blue, and orange regions in Fig. 7.7 which are fuzzy due to finite sized systems and finite number of disorder realisations.



these clusters of opposing phases act as trivial phases increasing the effective density of the trivial clusters. The result is that the transition occurs at a lower disorder strength for systems close to a topological phase with opposite winding number.

For a zero-disorder system in the trivial phase, introduction of disorder leads to complete localization of the bulk states. However, for $M_{A,B}$ in a trivial phase but close to the topological phases, the system surprisingly undergoes a transition into a topological phase at intermediate disorder strengths. Such disorder-induced topological phases, dubbed as topological Anderson insulators have been previously reported in Floquet systems [Titum *et al.* (2015)] and in various static systems [Li *et al.* (2009); Jiang *et al.* (2009)] and explained via a renormalized mass of the disorder averaged medium [Groth *et al.* (2009)]. The Floquet topological Anderson insulator phases appear in continuum with the neighboring topological phases, to the extent that our numerics can resolve. This is unlike the case of static systems with fixed electron densities [Groth *et al.* (2009)]. Such disorder-induced phases can occur for systems with both, ν_π and ν_0 topological order.

Various aspects of the phase diagram as a function of $M_A - M_B$ are as follows. As discussed in Section 7.3.2, there are no topological transitions when $M_A - M_B$ is varied keeping $M_A + M_B$ fixed, however, at certain values of $M_A - M_B$, the gaps close without a topological transition. This is reflected in the critical disorder strength (for the transitions out of the topological phases). This is shown by using the parameters considered in Fig. 7.6(c)-(d) and studying the effect of disorder on the phase diagram as function of $M_A - M_B$. Such modulations in the critical disorder strength arising

from such non-topological gap closings also explain the relative sizes of the lobes of the topological phases shown in Fig. 7.7.

Note that the physics arising from interplay of disorder with such non-topological gap closings is qualitatively distinct from that in the case of topological gap closings occurring for example between the topological and trivial phases in Fig. 7.7 (red/blue lines). While the topological order is unstable to disorder in the vicinity of the former, the latter is associated with robust topological order till very high disorder as well as formation of a topological Anderson insulator.

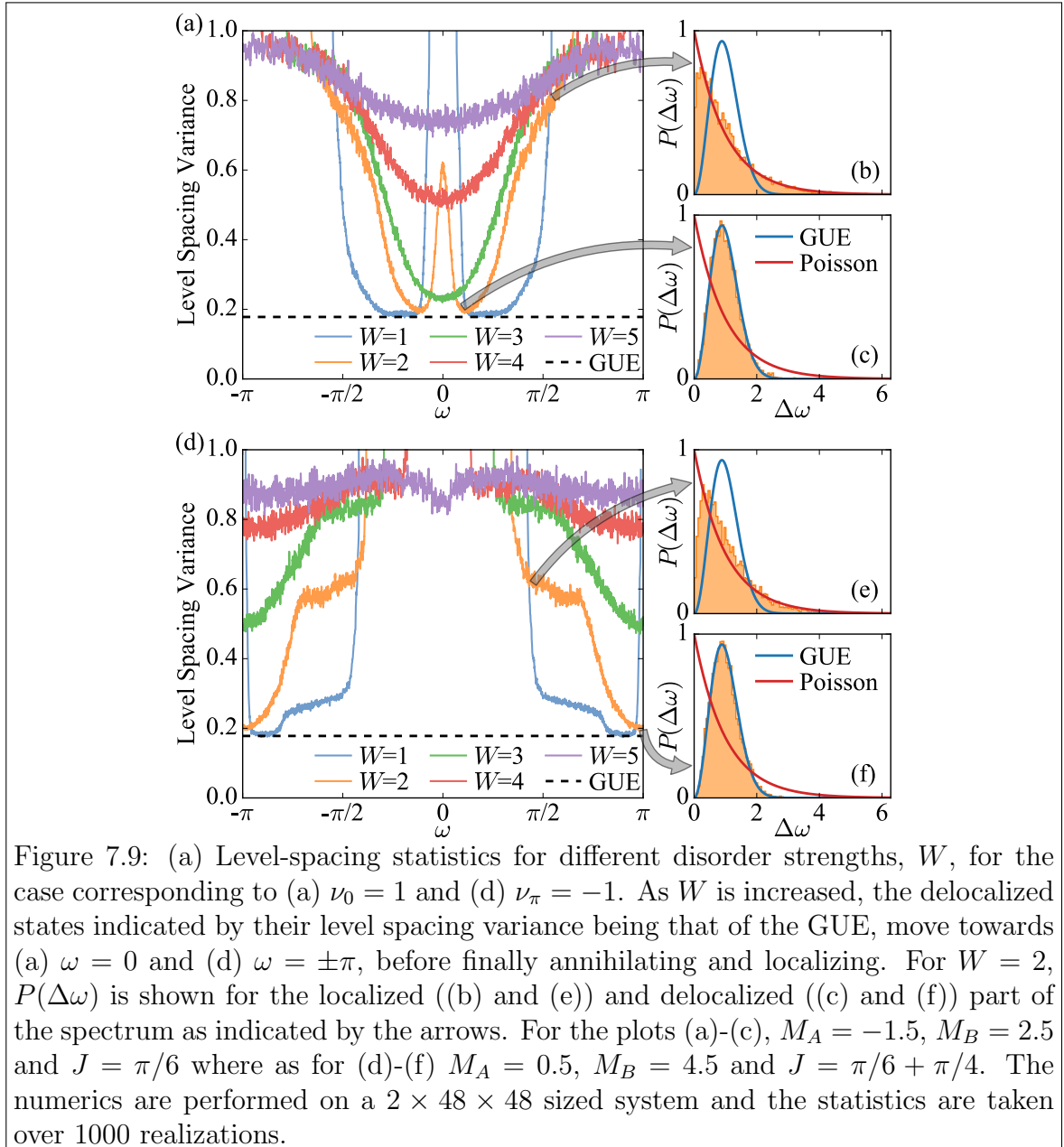
7.4.3 Level-spacing statistics

The interplay of Anderson localization and topology in Chern insulators leads to the occurrence of (at least one) delocalized state(s) in the bulk. Existence of a delocalized state can be motivated from spectral flow arguments [Laughlin (1981); Halperin (1982)]. Transitions out of the topological phase, such as the ones induced by disorder are accompanied by a break down of this delocalized state. Except in certain fine tuned scenarios, this happens through what is called a “levitation and pair annihilation” mechanism for disorder-driven topological phase transition [Halperin (1982); Levine *et al.* (1983); Laughlin (1984); Onoda *et al.* (2007)].

Essentially the same physics is found in the Floquet systems. The presence of the delocalized states in the quasienergy spectrum can be inferred from level spacings as described later in this section. At zero disorder, all single particle states of the system are delocalized. Addition of weak disorder leads to localization of all states in the bulk of the system, leaving a narrow band of delocalized bulk states surrounding every gap that can support edge states. Adding intermediate disorder to a Floquet topological phase leads to formation of bulk localized states in the 0- as well as the π -gap of the Floquet quasienergy spectrum.

On increasing the disorder, the delocalized states drift towards each other in the quasi-energy spectrum, and they meet and ‘annihilate’ at the critical disorder strength. In a Floquet system, since the quasienergies are periodic, the delocalized states can in principle levitate along two possible directions, however in all cases considered, it was found that the delocalized states levitate towards the center of the gap that separates them. The same mechanism appears to apply independently to the gaps around 0 and π (Fig. 7.1).

The quasienergies of the delocalized states can be probed using quasienergy resolved level-spacing statistics as was done for the energy spectrum in a static case [Prodan *et al.* (2010); Castro *et al.* (2015, 2016)]. The level spacing at quasienergy ω is



defined as $\Delta\omega = \omega_{i+1} - \omega_i$, where ω_i is the quasienergy for a finite system closest to ω . These spacings are normalized by disorder-averaged level spacings near ω . If ω corresponds to a localized part of the spectrum, then the quasienergy values arise from a Poisson process as they are uncorrelated and hence $\Delta\omega$ follows an exponential distribution [Mehta (2004)], *i.e.*, $P(\Delta\omega) \sim e^{-\Delta\omega}$. On the other hand if the Floquet eigenstates at quasienergy ω are delocalized, then the quasienergies repel each other and $P(\Delta\omega)$ follows a Wigner-Dyson distribution, specifically a Gaussian unitary ensemble [Mehta (2004)] (GUE) as the Chern insulators we work with have no symmetries, *i.e.*, $P(\Delta\omega) \sim \Delta\omega^2 e^{-4\Delta\omega^2/\pi}$. The two distributions can be distinguished by analyzing the sample variances of the normalized level spacings over many disorder realizations. The delocalized states are indicated by a level spacing variance of ≈ 0.178 (variance of the Wigner-Dyson distribution), whereas fully localized states should show a variance of 1 (variance of the exponential distribution). However, in our finite system studies, any variance that deviates from the GUE value will be interpreted as indicative of localization.

Representative results of level spacing analysis, that support the levitation annihilation picture are shown in Fig. 7.9. On increasing the disorder, the delocalized states move towards each other into the gap, and annihilate each other at the critical disorder. The level spacing statistics for the case where both ν_0 and ν_π have finite values, show delocalized states close to both $\omega = 0$ and $\omega = \pm\pi$ and localized bulk states away from them, as expected.

The level spacing statistics also correctly reflects the reentrant topological behavior. In order to show this, parameters corresponding to $M_A + M_B = 3$ of Fig. 7.7(a) are considered and the level spacing statistics are analyzed as shown in Fig. 7.10. It can be seen that at weak disorder, all the bulk states are localized as there are no quasienergies for which the level spacing variance is close to the GUE value. However on increasing the disorder, delocalized states appear which support a finite winding number, before all states localize again at strong disorder.

Hence, the study of level spacing statistics substantiates the physical picture developed in Section 7.4.2 and provides evidence for the “levitation and annihilation” mechanism of disorder induced phase transitions between Floquet topological and trivial phases. The level spacing studies also add further evidence supporting the existence of disorder-induced transitions into and out of a topological Anderson insulator phase.

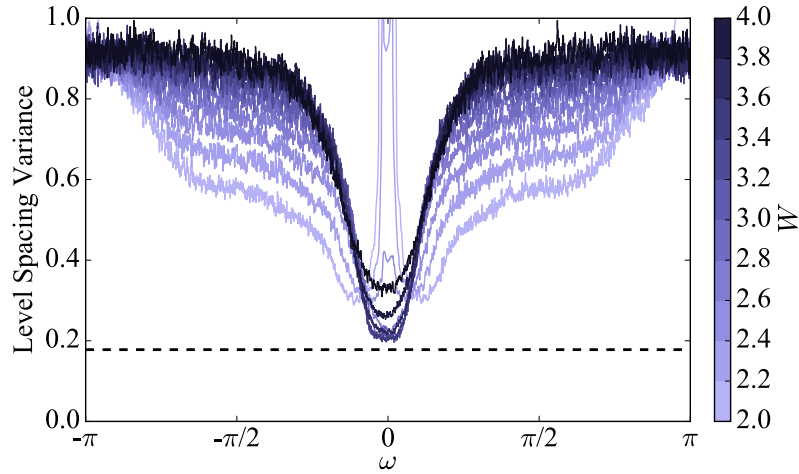


Figure 7.10: Level-spacing statistics showing the reentrant topological behavior. The different lines correspond to different disorder strengths (shown by the color bar) and the horizontal dashed value shows the GUE value. At weak disorder there are no delocalized states as the phase is trivial, however on increasing disorder, delocalized states appear close to $\omega = 0$ accompanied by a transition to a phase with $\nu_0 = 1$, and finally at very strong disorder, the system goes to a trivial phase again with all bulk states localized. For the plots, $M_A = 1$, $M_B = 2$, and $J = \pi/6$ and the statistics are taken over 1000 disorder realization for a $2 \times 48 \times 48$ sized system.

7.5 Summary

To summarize the chapter, the topological phase diagram of a periodically driven Chern insulator is studied, both in the presence and absence of disorder. In the absence of disorder, the exact phase diagram was analytically obtained by studying the Floquet quasienergy spectrum and the topology of the phases was characterized via appropriate winding invariants. It is found that the topological phase depends only on the mean of the periodic drive and not the amplitude, although the amplitude affects the localization lengths of the chiral edge modes in topological phase. In fact, at certain amplitudes there are non-topological gap closings in the quasienergy spectrum leading to vanishing of edge states. The phase diagram was then extended to include the effects of disorder by numerically computing the winding invariants generalized to include disorder. The topological phases were found to be robust to weak disorder, however strong disorder induced a phase transition from a topological to trivial phase. Interestingly, the system also showed a disorder induced transition into a topological Floquet Anderson insulator phase, where the system was trivial at weak/no disorder but underwent a transition to a topological phase at intermediate disorder. Careful analysis of level spacing statistics of the quasienergy spectrum

showed that the disorder-induced transitions happen via a levitation and annihilation of delocalized bulk states within a narrow window of quasienergy in the background of localized bulk states.

For a topological phase having chiral edge modes with quasienergies in the 0- and π -gap, the delocalized bulk states are also at quasienergies close to 0 and π respectively. On increasing disorder, the window of delocalized states drifts towards $\omega = 0$ and $\omega = \pi$ in the respective case, and at the critical disorder, they meet and annihilate each other driving the system to a trivial phase. The presence of the delocalized states is necessitated due to the fact that, in the model studied, any topological phase is accompanied by finite Chern number of the bulk bands, though the Chern number does not fully characterize the topological phase. This is crucially different from the anomalous Floquet-Anderson insulator introduced in Titum *et al.* (2016) where all bulk states are localized, hence the bulk bands have zero Chern number with edge modes present at all quasienergies.

There is however an interesting regime in the model studied here where bulk bands with zero Chern number and chiral edge modes coexist. If the parameters are tuned to a regime, where there exist edge modes in both the gaps at weak disorder, for instance $M_A + M_B = \pi$ in Fig. 7.7(c) and (d), then there are two sets of delocalized bulk states in each band (at weak disorder, the quasienergy spectrum still has two bands), close to $\omega = 0$ and $\omega = \pi$. On increasing disorder, these delocalized states levitate towards their respective gaps. There is threshold disorder where the gaps and the delocalized states corresponding to one of the edge states (the π -modes in this case) annihilate while the edge modes in the other gap are still present. In such a scenario, the two bands are not well separated, and the bulk states form one continuous band with zero Chern number but with equal number of chiral edge modes on either side, thus realizing a situation similar to the topological anomalous Floquet-Anderson insulator of Titum *et al.* (2016). An important difference though is, unlike Titum *et al.* (2016), the system would not realize a quantized charge pump due to the presence of delocalized bulk modes. On further increasing the disorder, the system goes directly to a trivial Anderson insulator and not an anomalous Floquet topological insulator.

This leads to an important observation that in the case studied here, the delocalized bulk states always annihilate between two bands, leading to breakdown of all edge states and associated topological order. It is interesting to ask, if there are scenarios where the delocalized bulk states within the same band annihilate each other. The latter situation could potentially lead to a coexistence of fully localized, zero Chern

number bulk bands but with chiral edge modes at all quasienergies. A possibility is that the large bandwidth of the bulk bands in our system prevents levitation of the delocalized states through the bulk. This raises an interesting question - namely the fate of the levitation and annihilation mechanism for periodically driven topological systems upon flattening of the Floquet quasienergy bands.

Chapter 8

Conclusions and Outlook

The thesis explored various aspects of the interplay of non-equilibrium quantum dynamics and topology. While the interplay was exploited to locate topological quantum phase transitions, characterize the topological phases, and also extract related exotic electromagnetic responses, new topological phases exclusive to out-of-equilibrium systems were also discussed.

In Chapter 3, it was shown that critical points corresponding to topological phase transitions can be located via non-analyticities of expectation values of local bulk observables measured over a family of non-equilibrium states generated via a quantum quench. A large class of initial states could be chosen for the quench, including finite temperature thermal states. Together the chapter presented an interesting scenario where the signatures of ground state quantum criticality seemed to be present in a large class of excited states with finite energy densities. However much of the analysis relied on the translation-invariant and non-interacting nature of the systems discussed. The source of the non-analyticity was shown to be a discontinuous change in the momentum space pseudospin texture at the critical momentum. Hence, a natural question is how robust are these signatures of criticality in systems where scattering between different momentum modes is not restricted, for instance in interacting and/or disordered systems. One of the simpler and more tractable questions that can be answered in this context is, can the protocol detect the disorder-driven topological criticality in the chiral-symmetric AIII class [Mondragon-Shem *et al.* (2014)] as such systems still have a single-particle description allowing for rather large system sizes to be studied numerically.

Chapter 4 discussed the applicability of the semiclassical equations of motion to describe wavepacket dynamics on lattice models hosting energy bands with finite Chern numbers. Specifically, the accuracy of the semiclassical framework in describing the motion of a realistic wavepacket was evaluated. In particular, it was found that,

in order to accurately capture the wavepacket dynamics, the extent of the wavepacket in momentum space needs to be taken into account as the dynamics is sensitive to the interplay of band dispersion and Berry curvature over the finite region of momentum space where the wavepacket has support.

Complementary to the bulk measures, the presence of topologically protected edge states can also be used as a diagnostic for the topological phase in these systems as was discussed in Chapter 5. It was shown that the chiral nature of edge states is manifested in the time-dependent chiral response to local density quenches on the edge, whereas in the trivial phase the excitations on the edges diffuse into the bulk. Since in optical lattice experiments the edges are difficult to access, power-law traps natural to such setups are an alternative way of mimicking edges. It was shown how they can induce new edges in the systems and that the new edge states can be probed from the quench dynamics.

In Chapter 6, the framework of semiclassical dynamics was used to study a Weyl semimetal under large magnetic fields, specifically, in the Hofstadter limit. It was shown that the energy spectrum of a Weyl semimetal under such magnetic fields is described by a family of fractals, dubbed the Weyl butterfly, which possesses new emergent Weyl nodes. The chiralities and locations of these emergent Weyl nodes were then probed using wavepacket dynamics. Further, it was also shown that the chiral anomaly, known to be linearly proportional to the magnetic field in the low field limit, inherits a fractal structure concomitant with the Weyl butterfly and is actually given by the difference of Chern numbers in the gaps of the Weyl butterfly. The results and techniques used in this chapter pave the way for further research on observation of quantum anomalies and their realizations in condensed matter systems. One of the specific questions to address in this regard is to study the anomalies due to the chiral gauge fields which couple with different signs to Weyl nodes depending on the chirality of the Weyl nodes. Such fields can be generated by a spatiotemporal variation of the Weyl node separation [Grushin *et al.* (2016b); Pikulin *et al.* (2016)], which can indeed be generated in optical lattice experiments. Such fields not only add additional corrections to the chiral anomaly but also lead to more exotic physics in the presence of external gauge fields, for instance, non-conservation of total charge in the bulk which is supposedly compensated by the surface. Further along these lines, such chiral magnetic fields can lead to the generation of an energy current parallel to the field, whose temperature dependence directly probes a gravitational anomaly. In simplest terms, the gravitational anomaly can be thought of as additional contributions to the chiral anomalies due to non-trivial properties of the space-time

metric. The signatures are expected to be present in the angular velocities of the edge Fermi arcs, which in principle can again be measured in cold atomic experiments. However, a detailed theoretical proposal for how these effects can be visualized in optical lattices is still missing and constitutes an important area of future research.

An example of topological phases exclusive to out-of-equilibrium systems was discussed in Chapter 7, where the phase diagram and topological invariants characterizing it for a disordered Chern insulator subjected to a Floquet drive were described. It was found that Chern insulators subjected to periodic drives can host topological phases which can have chiral edge modes in the bulk gaps of the Floquet quasienergy spectrum around π . The topological phases were characterized using bulk topological invariants extracted by mapping the unitary evolution within a time period to an energetically trivial but topologically non-trivial time evolution. It was also shown that presence of strong disorder induces new transitions from the different topological to trivial insulator phases, and from a trivial to a topological Anderson insulator phase at intermediate disorder strengths. Analysis of level statistics of the quasienergy spectrum indicated a levitation-annihilation mechanism near these transitions.

The results presented in this thesis and many other works have established that non-equilibrium quantum dynamics is a fascinating area of research which is yet to be explored in all its details. Under this broad field, some specific sub-fields have attracted immense interest, for instance, quench dynamics and periodically driven systems, and their interplay with topology. It has led to the discovery of exotic new phases of matter like Floquet-Chern insulators and discrete time-crystals. Another such instance is systems with eigenstate order and eigenstate phase transitions, for example, many-body localized and Ising spin-glass systems. However, despite such exotic phases existing out of equilibrium, there seems to be an absence of a universal framework that can connect the microscopic theories to dynamical macroscopic observables that characterize these non-equilibrium phases. In equilibrium systems, the analogous role is played by statistical mechanics which bridges microscopic theories and macroscopic thermodynamics. The first step towards building such a framework for non-equilibrium quantum many-body systems appears to me as one of the most promising directions the field is going to take in the near future and also happens to be one of the directions towards which much of my current endeavor is directed.

Bibliography

- Affleck, I., T. Kennedy, E. H. Lieb, and H. Tasaki, 1987, Phys. Rev. Lett. **59**, 799.
- Affleck, I., T. Kennedy, E. H. Lieb, and H. Tasaki, 1988, Commun. Math. Phys. **115**(3), 477.
- Aidelsburger, M., M. Atala, M. Lohse, J. T. Barreiro, B. Paredes, and I. Bloch, 2013, Phys. Rev. Lett. **111**, 185301.
- Aidelsburger, M., M. Lohse, C. Schweizer, M. Atala, J. T. Barreiro, S. Nascimbene, N. R. Cooper, I. Bloch, and N. Goldman, 2015, Nat. Phys. **11**, 162.
- Aji, V., 2012, Phys. Rev. B **85**, 241101.
- Anderson, M. H., J. R. Ensher, M. R. Matthews, C. E. Wieman, and E. A. Cornell, 1995, Science **269**, 198.
- Araújo, M. A. N., and E. V. Castro, 2014, J. Phys. Condens. Matter **26**, 075501.
- Bakr, W. S., A. Peng, M. E. Tai, R. Ma, J. Simon, J. I. Gillen, S. Fölling, L. Pollet, and M. Greiner, 2010, Science **329**, 547.
- Ben Dahan, M., E. Peik, J. Reichel, Y. Castin, and C. Salomon, 1996, Phys. Rev. Lett. **76**, 4508.
- Bernevig, B. A., and T. L. Hughes, 2013, *Topological insulators and topological superconductors* (Princeton University Press).
- Bernevig, B. A., T. L. Hughes, and S.-C. Zhang, 2006, Science **314**, 1757.
- Bernevig, B. A., and S.-C. Zhang, 2006, Phys. Rev. Lett. **96**, 106802.
- Bertlmann, R. A., 2000, *Anomalies in quantum field theory* (Oxford University Press).
- Bhattacharyya, S., S. Dasgupta, and A. Das, 2015, Sci. Rep. **5**, 16490.

- Bloch, I., J. Dalibard, and W. Zwerger, 2008, *Rev. Mod. Phys.* **80**, 885.
- Bott, R., and R. Seeley, 1978, *Comm. Math. Phys.* **62**, 235.
- Bradley, C. C., C. A. Sackett, J. J. Tollett, and R. G. Hulet, 1995, *Phys. Rev. Lett.* **75**, 1687.
- Brüning, J., V. V. Demidov, and V. A. Geyler, 2004, *Phys. Rev. B* **69**, 033202.
- Bulmash, D., and X.-L. Qi, 2016, *Phys. Rev. B* **93**, 081103.
- Burkov, A. A., 2015, *Phys. Rev. B* **91**, 245157.
- Burkov, A. A., and L. Balents, 2011, *Phys. Rev. Lett.* **107**, 127205.
- Caio, M. D., N. R. Cooper, and M. J. Bhaseen, 2015, *Phys. Rev. Lett.* **115**, 236403.
- Castro, E. V., R. de Gail, M. P. López-Sancho, and M. A. H. Vozmediano, 2016, *Phys. Rev. B* **93**, 245414.
- Castro, E. V., M. P. López-Sancho, and M. A. H. Vozmediano, 2015, *Phys. Rev. B* **92**, 085410.
- Chang, C.-Z., J. Zhang, X. Feng, J. Shen, Z. Zhang, M. Guo, K. Li, Y. Ou, P. Wei, L.-L. Wang, Z.-Q. Ji, Y. Feng, *et al.*, 2013, *Science* **340**, 167.
- Chiu, C.-K., J. C. Y. Teo, A. P. Schnyder, and S. Ryu, 2016, *Rev. Mod. Phys.* **88**, 035005.
- D'Alessio, L., and M. Rigol, 2015, *Nat. Comm.* **6**, 8336.
- Dauphin, A., and N. Goldman, 2013, *Phys. Rev. Lett.* **111**, 135302.
- Davis, K. B., M. O. Mewes, M. R. Andrews, N. J. van Druten, D. S. Durfee, D. M. Kurn, and W. Ketterle, 1995, *Phys. Rev. Lett.* **75**, 3969.
- Duca, L., T. Li, M. Reitter, I. Bloch, M. Schleier-Smith, and U. Schneider, 2015, *Science* **347**, 288.
- Else, D. V., B. Bauer, and C. Nayak, 2016, *Phys. Rev. Lett.* **117**, 090402.
- Ernst, P. T., S. Götze, J. S. Krauser, K. Pyka, D.-S. Lühmann, D. Pfannkuche, and K. Sengstock, 2010, *Nat. Phys.* **6**, 56.

- Fläschner, N., D. Vogel, M. Tarnowski, B. S. Rem, D.-S. Lühmann, M. Heyl, J. C. Budich, L. Mathey, K. Sengstock, and C. Weitenberg, 2016, arXiv:1608.05616 .
- Fu, L., C. L. Kane, and E. J. Mele, 2007, Phys. Rev. Lett. **98**, 106803.
- Gaunt, A. L., T. F. Schmidutz, I. Gotlibovych, R. P. Smith, and Z. Hadzibabic, 2013, Phys. Rev. Lett. **110**, 200406.
- Goldman, N., and J. Dalibard, 2014, Phys. Rev. X **4**, 031027.
- Goldman, N., J. Dalibard, A. Dauphin, F. Gerbier, M. Lewenstein, P. Zoller, and I. B. Spielman, 2013, Proc. Natl. Acad. Sci. U.S.A. **110**, 6736.
- Goryo, J., and M. Kohmoto, 2002, Phys. Rev. B **66**, 085118.
- Goswami, P., and S. Tewari, 2013a, Phys. Rev. B **88**, 245107.
- Goswami, P., and S. Tewari, 2013b, arXiv:1311.1506 .
- Greiner, M., O. Mandel, T. Esslinger, T. W. Hänsch, and I. Bloch, 2002, Nature **415**, 39.
- Greiner, M., C. A. Regal, and D. S. Jin, 2003, Nature **426**, 537.
- Groth, C. W., M. Wimmer, A. R. Akhmerov, J. Tworzydło, and C. W. J. Beenakker, 2009, Phys. Rev. Lett. **103**, 196805.
- Grushin, A. G., 2012, Phys. Rev. D **86**, 045001.
- Grushin, A. G., S. Roy, and M. Haque, 2016a, J. Stat. Mech. **2016**, 083103.
- Grushin, A. G., J. W. F. Venderbos, A. Vishwanath, and R. Ilan, 2016b, Phys. Rev. X **6**, 041046.
- Haldane, F. D. M., 1988, Phys. Rev. Lett. **61**, 2015.
- Halperin, B. I., 1982, Phys. Rev. B **25**, 2185.
- Hasan, M. Z., and C. L. Kane, 2010, Rev. Mod. Phys. **82**, 3045.
- Hasan, M. Z., and J. E. Moore, 2011, Annu. Rev. Condens. Matter Phys. **2**, 55.
- Hasegawa, Y., 1992, J. Phys. Soc. Jpn. **61**, 1657.
- Hastings, M. B., and S. Michalakis, 2015, Comm. Math. Phys. **334**, 433.

- Hatsugai, Y., 1993a, Phys. Rev. Lett. **71**, 3697.
- Hatsugai, Y., 1993b, Phys. Rev. B **48**, 11851.
- Hauke, P., M. Lewenstein, and A. Eckardt, 2014, Phys. Rev. Lett. **113**, 045303.
- Hofstadter, D. R., 1976, Phys. Rev. B **14**, 2239.
- Hosur, P., S. A. Parameswaran, and A. Vishwanath, 2012, Phys. Rev. Lett. **108**, 046602.
- Hosur, P., and X. Qi, 2013, Comptes Rendus Physique **14**, 857.
- Jaksch, D., and P. Zoller, 2003, New J. Phys. **5**, 56.
- Jiang, H., L. Wang, Q.-f. Sun, and X. C. Xie, 2009, Phys. Rev. B **80**, 165316.
- Jochim, S., M. Bartenstein, A. Altmeyer, G. Hendl, S. Riedl, C. Chin, J. Hecker Denschlag, and R. Grimm, 2003, Science **302**, 2101.
- Jotzu, G., M. Messer, R. Desbuquois, M. Lebrat, T. Uehlinger, D. Greif, and T. Esslinger, 2014, Nature **515**, 237.
- Kane, C. L., and E. J. Mele, 2005a, Phys. Rev. Lett. **95**, 226801.
- Kane, C. L., and E. J. Mele, 2005b, Phys. Rev. Lett. **95**, 146802.
- Kennedy, C. J., W. C. Burton, W. C. Chung, and W. Ketterle, 2015, Nat. Phys. **11**, 859.
- von Keyserlingk, C. W., and S. L. Sondhi, 2016a, Phys. Rev. B **93**, 245145.
- von Keyserlingk, C. W., and S. L. Sondhi, 2016b, Phys. Rev. B **93**, 245146.
- Kharzeev, D. E., 2014, Progress in Particle and Nuclear Physics **75**, 133.
- Khemani, V., A. Lazarides, R. Moessner, and S. L. Sondhi, 2016, Phys. Rev. Lett. **116**, 250401.
- Killi, M., and A. Paramekanti, 2012, Phys. Rev. A **85**, 061606.
- Killi, M., S. Trotzky, and A. Paramekanti, 2012, Phys. Rev. A **86**, 063632.
- Kitaev, A., 2001, Phys.-Usp. **44**, 131.

- Kitaev, A., V. Lebedev, and M. Feigel'man, 2009, in *AIP Conference Proceedings* (AIP), volume 1134, pp. 22–30.
- Kitagawa, T., E. Berg, M. Rudner, and E. Demler, 2010, *Phys. Rev. B* **82**, 235114.
- Klier, J., I. V. Gornyi, and A. D. Mirlin, 2015, *Phys. Rev. B* **92**, 205113.
- von Klitzing, K., G. Dorda, and M. Pepper, 1980, *Phys. Rev. Lett.* **45**, 494.
- Kohmoto, M., B. I. Halperin, and Y.-S. Wu, 1992, *Phys. Rev. B* **45**, 13488.
- Kolovsky, A. R., F. Grusdt, and M. Fleischhauer, 2014, *Phys. Rev. A* **89**, 033607.
- Koshino, M., and H. Aoki, 2003, *Phys. Rev. B* **67**, 195336.
- Koshino, M., and H. Aoki, 2004, *Phys. Rev. B* **69**, 081303.
- Koshino, M., H. Aoki, K. Kuroki, S. Kagoshima, and T. Osada, 2001, *Phys. Rev. Lett.* **86**, 1062.
- Koshino, M., H. Aoki, T. Osada, K. Kuroki, and S. Kagoshima, 2002, *Phys. Rev. B* **65**, 045310.
- Landsteiner, K., 2014, *Phys. Rev. B* **89**, 075124.
- Laughlin, R. B., 1981, *Phys. Rev. B* **23**, 5632.
- Laughlin, R. B., 1984, *Phys. Rev. Lett.* **52**, 2304.
- Lazarides, A., A. Das, and R. Moessner, 2014a, *Phys. Rev. E* **90**, 012110.
- Lazarides, A., A. Das, and R. Moessner, 2014b, *Phys. Rev. Lett.* **112**, 150401.
- Levine, H., S. B. Libby, and A. M. M. Pruisken, 1983, *Phys. Rev. Lett.* **51**, 1915.
- Li, J., R.-L. Chu, J. K. Jain, and S.-Q. Shen, 2009, *Phys. Rev. Lett.* **102**, 136806.
- Li, Z., H.-Q. Wang, D.-W. Zhang, S.-L. Zhu, and D.-Y. Xing, 2016, *Phys. Rev. A* **94**, 043617.
- Liu, C.-X., P. Ye, and X.-L. Qi, 2013, *Phys. Rev. B* **87**, 235306.
- Liu, X.-J., K. T. Law, and T. K. Ng, 2014, *Phys. Rev. Lett.* **112**, 086401.
- Ludwig, A. W. W., M. P. A. Fisher, R. Shankar, and G. Grinstein, 1994, *Phys. Rev. B* **50**, 7526.

- Mehta, M., 2004, *Random Matrices*, Pure and applied mathematics (Elsevier/Academic Press).
- Meyrath, T. P., F. Schreck, J. L. Hanssen, C.-S. Chuu, and M. G. Raizen, 2005, Phys. Rev. A **71**, 041604.
- Miyake, H., G. A. Siviloglou, C. J. Kennedy, W. C. Burton, and W. Ketterle, 2013, Phys. Rev. Lett. **111**, 185302.
- Mondragon-Shem, I., T. L. Hughes, J. Song, and E. Prodan, 2014, Phys. Rev. Lett. **113**, 046802.
- Nagaosa, N., J. Sinova, S. Onoda, A. H. MacDonald, and N. P. Ong, 2010, Rev. Mod. Phys. **82**, 1539.
- Nielsen, H., and M. Ninomiya, 1983, Phys. Lett. B **130**, 389.
- Nielsen, H. B., and M. Ninomiya, 1981, Physics Letters B **105**, 219.
- Oka, T., and H. Aoki, 2009, Phys. Rev. B **79**, 081406.
- Ominato, Y., and M. Koshino, 2016, Phys. Rev. B **93**, 245304.
- Onoda, M., Y. Avishai, and N. Nagaosa, 2007, Phys. Rev. Lett. **98**, 076802.
- Pikulin, D. I., A. Chen, and M. Franz, 2016, Phys. Rev. X **6**, 041021.
- Potter, A. C., T. Morimoto, and A. Vishwanath, 2016, Phys. Rev. X **6**, 041001.
- Price, H., and N. Cooper, 2012, Phys. Rev. A **85**, 033620.
- Prodan, E., T. L. Hughes, and B. A. Bernevig, 2010, Phys. Rev. Lett. **105**, 115501.
- Qi, X.-L., and S.-C. Zhang, 2011, Rev. Mod. Phys. **83**, 1057.
- Regal, C. A., M. Greiner, and D. S. Jin, 2004, Phys. Rev. Lett. **92**, 040403.
- Rigol, M., V. Dunjko, and M. Olshanii, 2008, Nature **452**, 854.
- Roy, R., 2009, Phys. Rev. B **79**, 195322.
- Roy, R., and F. Harper, 2016, arXiv:1603.06944 .
- Roy, S., A. G. Grushin, R. Moessner, and M. Haque, 2015, Phys. Rev. A **92**, 063626.

- Roy, S., M. Kolodrubetz, J. E. Moore, and A. G. Grushin, 2016, Phys. Rev. B **94**, 161107.
- Roy, S., R. Moessner, and A. Das, 2017, Phys. Rev. B **95**, 041105.
- Roy, S., and G. J. Sreejith, 2016, Phys. Rev. B **94**, 214203.
- Rudner, M. S., N. H. Lindner, E. Berg, and M. Levin, 2013, Phys. Rev. X **3**, 031005.
- Ryu, S., A. P. Schnyder, A. Furusaki, and A. W. Ludwig, 2010, New J. Phys. **12**, 065010.
- Sachdev, S., 2011, *Quantum Phase Transitions* (Cambridge University Press).
- Sacramento, P. D., 2014, Phys. Rev. E **90**, 032138.
- Son, D. T., and B. Z. Spivak, 2013, Phys. Rev. B **88**, 104412.
- Stanescu, T. D., V. Galitski, and S. Das Sarma, 2010, Phys. Rev. A **82**, 013608.
- Streda, P., 1982, J. Phys. C **15**, L717.
- Su, W. P., J. R. Schrieffer, and A. J. Heeger, 1979, Phys. Rev. Lett. **42**, 1698.
- Suzuki, S., J.-i. Inoue, and B. K. Chakrabarti, 2013, *Quantum Ising Phases and Transitions in Transverse Ising Models* (Springer, Heidelberg).
- Thouless, D. J., M. Kohmoto, M. P. Nightingale, and M. den Nijs, 1982, Phys. Rev. Lett. **49**, 405.
- Titum, P., E. Berg, M. S. Rudner, G. Refael, and N. H. Lindner, 2016, Phys. Rev. X **6**, 021013.
- Titum, P., N. H. Lindner, M. C. Rechtsman, and G. Refael, 2015, Phys. Rev. Lett. **114**, 056801.
- Vafeek, O., and A. Vishwanath, 2014, Annu. Rev. Condens. Matter Phys. **5**, 83.
- Dubček, T., C. J. Kennedy, L. Lu, W. Ketterle, M. Soljačić, and H. Buljan, 2015, Phys. Rev. Lett. **114**, 225301.
- Volovik, G. E., 2003, *The Universe in a Helium Droplet* (Clarendon Press, Oxford).
- Wang, Y. H., H. Steinberg, P. Jarillo-Herrero, and N. Gedik, 2013, Science **342**, 453.

Wang, Y.-Q., and X.-J. Liu, 2016, Phys. Rev. A **94**, 031603.

Wegner, F. J., 1971, J. Math. Phys. **12**, 2259.

Wen, X., and A. Zee, 1989, Nucl. Phys. B **316**, 641 .

Xiao, D., M.-C. Chang, and Q. Niu, 2010, Rev. Mod. Phys. **82**, 1959.

Yao, N. Y., A. C. Potter, I.-D. Potirniche, and A. Vishwanath, 2017, Phys. Rev. Lett. **118**, 030401.

Zak, J., 1989, Phys. Rev. Lett. **62**, 2747.

Zhang, H., C.-X. Liu, X.-L. Qi, X. Dai, Z. Fang, and S.-C. Zhang, 2009, Nat. Phys. **5**, 438.

Zwierlein, M. W., C. A. Stan, C. H. Schunck, S. M. F. Raupach, S. Gupta, Z. Hadzibabic, and W. Ketterle, 2003, Phys. Rev. Lett. **91**, 250401.

Zyuzin, A. A., S. Wu, and A. A. Burkov, 2012, Phys. Rev. B **85**, 165110.

Selbständigkeitserklärung

Hiermit versichere ich, dass ich die vorliegende Arbeit selbständig und nur unter Verwendung der angegebenen Literatur und Hilfsmittel angefertigt habe.

Chemnitz, 30.10.2017

Sthitadhi Roy

.....
Unterschrift